Precision Timing in Highly Granular Calorimeters and Applications in Long Baseline Neutrino and Lepton Collider Experiments

Lorenz Konrad Emberger

Vollständiger Abdruck der von der TUM School of Natural Sciences der Technischen

Universität München

zur Erlangung des akademischen Grades eines

Doktors der Naturwissenschaften (Dr. rer. nat.)

genehmigten Dissertation.

Vorsitz: Prof. Dr. Nora Brambilla

Prüfer der Dissertation:

       1.   Hon.-Prof. Dr. Allen C. Caldwell

       2.   Prof. Dr. Lukas Heinrich

Die Dissertation wurde am 16.08.2022 bei der Technischen Universität München eingereicht

und durch die TUM School of Natural Sciences am 17.11.2022 angenommen.

Precision Timing in Highly Granular Calorimeters and Applications in Long Baseline Neutrino and Lepton Collider Experiments

Dissertation von
Lorenz Konrad Emberger

Technische Universität München
Fakultät für Physik

Max–Planck–Institut für Physik
(Werner–Heisenberg–Institut)

Munich, August 2022

Abstract

To fully exploit the clean event signatures and reduced hadronic background for particle flow reconstruction at future e^+e^- collider experiments, highly granular calorimeters are a very attractive option. They offer unprecedented longitudinal and transversal segmentation and consequently an increased capability of particle separation. This enhances the energy resolution of hadronic jets, a vital ingredient for high precision physics involving hadronic decays of the electroweak gauge bosons. Furthermore, the features of these detectors are also beneficial for applications in high precision fixed target geometries like DUNE, a future long baseline neutrino experiment. The international R&D collaboration CALICE is focused on the development of such highly granular systems. The Analog Hadronic Calorimeter (AHCAL), a prototype based on scintillator tiles with SiPM read out, as well as detector concepts based on its design are the topic of this thesis.

A time calibration for the test beam data set recorded with the AHCAL 2018 is presented, along with the correction of occupancy related distortions. The achieved time resolution for minimum ionizing particles is 700 ± 3 ps, meeting the design goal of the prototype of 1 ns or below. Additional studies investigating the detectors response to particle showers in simulation and data are presented. To investigate the intrinsic time resolution of the active elements, independent of the electronics of the prototype, a dedicated campaign to test single channels is performed. According to the results the contribution of the electronics to the time resolution is comparable to the contribution of scintillator and SiPM, hence both components have to be addressed if the combined performance should be improved in the future.

A calorimeter concept based on the AHCAL is studied in the context of long baseline neutrino experiments, using simulations for a subsystem of the DUNE near detector called ND–GAr. Inspired by the AHCAL's timing performance the time-of-flight reconstruction of neutrons produced in neutrino interactions is studied and a resolution of 42 MeV is achieved. The calorimeter also extends the Muon/Pion identification capabilities of the system to the GeV range and a multivariate study based on a boosted decision tree was implemented to quantify the achievable efficiency and purity. Based on this metric the impact of an optional muon identification system on the separation is investigated. A discussion of the results also evaluates the usefulness of the system for the oscillation analysis DUNE will perform.

Zusammenfassung

Um von den übersichtlichen Ereignissignaturen und dem reduzierten hadronischen Untergrund für die Particle Flow Rekonstruktion bei zukünftigen e^+e^--Collider-Experimenten zu profitieren, sind hochgranulare Kalorimeter mit einer exzellenten longitudinalen und transversalen Segmentierung eine sehr vielversprechende Option. Ihre verbesserte Fähigkeit zur Teilchentrennung erhöht die Energieauflösung von hadronischen Jets, welche für die Präzisionsphysik mit hadronischen Zerfällen der elektroschwachen Eichbosonen von entscheidender Bedeutung ist. Darüber hinaus sind die Eigenschaften dieser Detektoren auch für Anwendungen in zukünftigen "Fixed Target"-Geometrien wie dem DUNE-Nahdetektor von Vorteil, da sie die Effizienz der Teilchenidentifikation verbessern. Die internationale R&D-Kollaboration CALICE entwickelt diese hochgranularen Systeme. Das Analoge Hadronische Kalorimeter (AHCAL), ein Prototyp auf der Basis von Szintillatorkacheln mit SiPM-Auslese, sowie darauf aufbauende Detektorkonzepte, sind Thema dieser Arbeit.

Es wird eine Zeitkalibrierung für den mit dem AHCAL 2018 aufgenommenen Teststrahldatensatz vorgestellt, zusammen mit der Korrektur von okkupanzbedingten Verzerrungen. Die erreichte Zeitauflösung für minimalionisierende Teilchen beträgt 700±3 ps, womit das Designziel des Prototyps von 1 ns (oder besser) erreicht wird. Zusätzliche Studien untersichen die Reaktion des Detektors auf Teilchenschauer in Simulation und Daten. Um die intrinsische Zeitauflösung der aktiven Elemente unabhängig von der Elektronik des Prototyps zu bestimmen, wurden Tests einzelner Kanäle durchgeführt. Den Ergebnissen zufolge ist der Beitrag der Elektronik zur Zeitauflösung vergleichbar mit dem Beitrag von Szintillator und SiPM, sodass beide Komponenten verbessert werden müssen, um die kombinierte Auflösung deutlich zu verbessern. Ein auf dem AHCAL basierendes Kalorimeterkonzept wird für den ND-GAr, einem Teil des DUNE-Nahdetektors, simuliert. In Anlehnung an die die Zeitauflösung des AHCAL wird die Flugzeitrekonstruktion von Neutronen, welche bei Neutrinowechselwirkungen entstehen, untersucht und eine Auflösung von 42 MeV erreicht. Das Kalorimeter erweitert auch die Muon/Pion-Identifizierungsfähigkeiten des Systems auf den GeV-Bereich Des weiteren wird eine multivariate Studie auf der Grundlage eines Boosted Decision Tree vorgestellt, um die erreichbare Effizienz und Reinheit der Selektion zu quantifizieren. Mit dieser Metrik werden die Auswirkungen eines optionalen Myonenidentifikationssystems untersucht. Eine Diskussion der Ergebnisse bezieht sich auf die Nützlichkeit des Systems für die Oszillationsanalyse welchezum Kernporgramm von DUNE gehört.

Acknowledgment

First, i would like to express my gratitude to Frank Simon, my supervisor since i started working on my master thesis in 2017. Thanks for the inspiring guidance throughout my work and for always taking time to answer my questions and giving me advice to move forward in my research. One cannot wish for a more passionate supervisor.

I also want to thank Prof. Allen Caldwell for accepting me as a PhD candidate and giving me the opportunity to conduct my PhD research at the MPP. Furthermore, i would like to thank Prof. Susanne Mertens and Prof. Nora Brambilla for taking time to be on my thesis committee.

My sincere thanks go to all present and former colleagues in the Future Detectors group: Swathi, Marco, Hendrik, Malte, Christian, Miro, Yasmine, Thomas, Fabian, Ivan, Christian, Malinda, and the entire Belle II group for the great atmosphere at work and for the countless funny and interesting discussions during the coffee and lunch breaks. The fierce but friendly table tennis battles were always a special highlight.

I would like to thank all the members of the CALICE Collaboration, especially Daniel, Olin, Vladimir, Jiří, Eldwan, Anna, Amine, Linghui, Naoki, Tatsuro, Katja and Felix for fruitful discussions and good times at the AHCAL test beams and collaboration meetings around the world. A special thank you goes to Katja for organizing all the DESY test beams and supporting us during beam time, as well as to Ivan, Fabian and Malte for making these efforts a success. Thanks to Jiří, Malinda as well as the entire AHCAL team at DESY for the countless enjoyable evenings at Samarkand and the spontaneous get-togethers at the DESY hostel.

Finally, i want to thank all my friends and family and express my deepest gratitude to my parents, Isolde and Konrad. Thank you for the moral (and financial) support throughout my studies and the course of this thesis. Without you this would not have been possible.

Contents

Contents

List of Figures

Chapter 1

Introduction

To lead future accelerator based experiments in high energy particle physics to a success, new detector developments pushing the state-of-the-art need to be developed. Regardless of the nature of the experiment, collider or neutrino physics, the need for unprecedented precision is a commonality. The calorimeters used to measure the energy of particles have been an essential component of particle detectors in the past and currently undergo significant development to meet future demands. Especially increasing particle rates and multiplicities call for high spatial segmentation and precise time resolution. These highly complex devices profit from advances in sensor technology and microelectronics, mechanical production, automatization as well as cutting-edge data processing to meet future demands.

Scintillator based calorimeters have a long history. The first large scale device was built for the Ω [1] experiment at CERN in the 80s. The JETSET [2] experiment installed the first full–acceptance device at the Low Energy Ion Ring at CERN to measure electromagnetic showers. First developments of scintillator calorimeters designed for hadron detection eventually led to the SPACAL [3]. All of the early calorimeters used optical fibers to guide the light out of the active volume to the photo multiplier tubes, since those were to big to be installed inside without reducing the performance. The development of small semiconductor based photon counters, such as the Silicon Photomultiplier, enabled the integration of the active electronics into the detector to create compact designs. The R&D collaboration CALICE develops, among others, highly granular scintillator calorimeters for applications in future particle physics experiments which rely on increased particle separation and precise energy reconstruction.

The technological prototype of the Analog Hadronic Calorimeter (AHCAL) is the current cubic meter scale detector of a highly granular calorimeter with SiPM-On-Tile readout [4]. It follows the physics prototype [5] and is built to demonstrate compact and scalable implementations of structural elements and read out electronics. It is the last stage of prototype towards a full scale collider detector at possible future facilities like ILC [6] or CLIC [7]. The device provides 5 dimensional information on individual hits, the three spatial coordinates as well as energy and time. This imaging capability makes it a suitable detector for particle flow reconstruction and sophisticated machine learning techniques for event reconstruction. The calorimeter was tested at the beam test facility at SPS in 2018 where it recorded muon, electron and hadron events. The time calibration and analysis of these data sets is a main subject of this thesis.

Inspired by the design of the AHCAL, current studies on the Near Detector of the long-

baseline neutrino experiment DUNE include a calorimeter concept for the reconstruction of neutral particle and particle separation. It surrounds a gaseous time projection chamber to provide hermeticity and the full reconstruction of the final state of neutrino interactions on argon nuclei. This multi purpose detector called ND-GAr is designed to investigate rare neutrino interactions to enhance our current understanding of cross-sections and event rates. Those are essential in order to increase the precision of the simulation models and deliver the full scientific potential of the DUNE experiment. This thesis investigates the precision of a time-of-flight reconstruction procedure for neutrons. Furthermore, the particle separation capability of muons and pions based on Boosted Decision Tree learning is presented.

Despite the differences in the physics programs of colliders and long-baseline neutrino facilities the detector requirements are very similar in certain aspects. This thesis shows synergies in calorimeter design and reports on relevant performance studies, with special focus on time measurement. Especially the results obtained with real data from various beam tests are transferred to simulation studies for future concepts, to illustrate possibilities for transferable knowledge between the two fields.

Chapter 2

The Future of High Energy Particle Physics

This chapter provides background information on the scientific foundation of future high precision particle physics experiments. The two–pronged approach of high energy and high intensity is discussed by the examples of future linear e^+e^--colliders and the Deep Underground Neutrino Experiment (DUNE). Finally, joint requirements for detector developments are introduced.

2.1 Central Questions in Particle Physics

The overarching theory describing most of the interactions in particle physics, the standard model of particle physics, was experimentally completed with the discovery of the Higgs boson in 2012 [8, 9]. It provides a mathematical formalism to predict the behavior of 30 known fundamental particles, their interactions and ultimately the formation of nucleons that constitute our visible universe. These particles are categorized according to their spin quantum number, where a particle with spin 1/2 is called fermion, and a particle with integer spin is called gauge boson. Gauge bosons are known to mediate three of the four known fundamental forces called weak, strong and electromagnetic. Gravity is not part of the standard model and will be omitted in this introduction. Fermions, subdivided into 6 charged quarks, 6 leptons and their respective antiparticle, interact by the exchange of a gauge boson. Quarks are bound by the strong force, mediated by the gluon, to form a multitude of Hadrons where the most prominent of them are protons and neutrons, constituents of the atomic nucleus. Leptons are comprised of the electron, the muon and the tau lepton as well as the corresponding neutrinos. These particles interact among each other by the weak force, mediated by the W and Z bosons. Additionally, all charged particles can interact electromagnetically by photon exchange. A priori, W and Z bosons are massless, a fundamental feature of a gauge theory with underlying SU(2) symmetry. Since experiments have revealed the mass of these bosons, a mechanism of symmetry breaking is required to introduce the masses into the theoretical description. The Higgs mechanism, published in 1964, provides this solution along with a newly proposed particle called Higgs boson [10]. A complete collection of the particles in the standard model is shown in Section 2.1.

To date, predictions of the standard model of particle physics survived extensive tests and advanced to an extremely successful model. With the observation of the Higgs boson, all particles predicted by the standard model have been observed, while no other

Standard Model of Elementary Particles
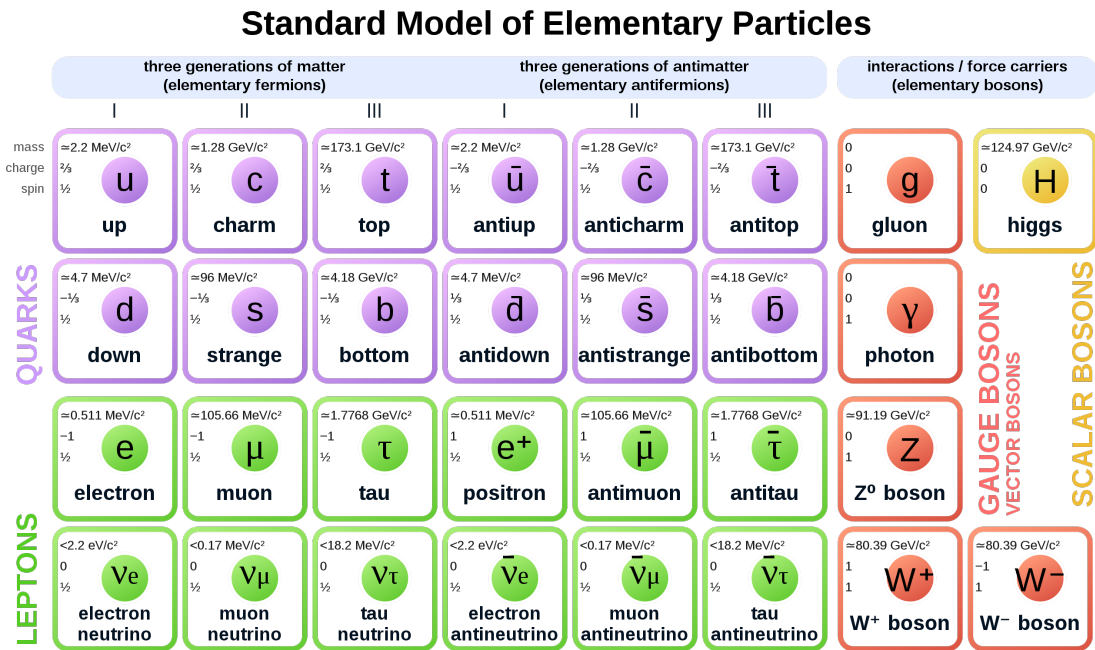
Figure 2.1: Overview of the known fundamental particles and antiparticles in the standard model of particle physics.

fundamental particles have been discovered. There are, however, several shortcomings like the missing explanation of the neutrino masses and the hierarchy problem, connected to the huge difference between the higgs mass and the planck scale, as well as astrophysical observations pointing to the existence of a new form of matter ("dark matter."). The following sections discuss future approaches to these questions.

2.2 Precision Measurements on the Higgs Boson

The precise investigation of the Higgs sector is among the most promising paths towards deeper understanding of the fundamentals of the universe. Probing self-coupling and the nature of the electroweak phase transition may provide information on baryogenesis in the early universe [11]. So called Higgs-portal models implement extensions of the standard model as a new dark matter state interacting with the Higgs boson [12]. This would result in invisible decays of the Higgs boson which can be probed at colliders.
So far, the measurements of ATLAS and CMS on the Higgs couplings to vector bosons and fermions are found to be consistent to the standard model predictions within a 10% error margin [13]. Possible deviations of the standard model prediction are expected to appear at the 5% level or lower, so future high energy physics experiments are designed to explore the Higgs sector at this precision [14]. The most important measurement at
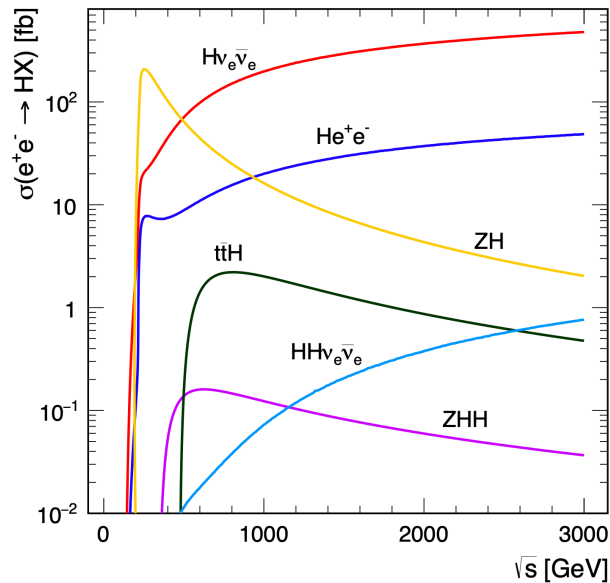
Figure 2.2: Higgs production channels with corresponding cross-sections in e$^+$e$^-$ collisions. Taken from [16].

future lepton collider concepts like ILC [15] or CLIC [7] is the reaction (e$^+$e$^-$ → ZH) at a center-of-mass energy of $\sqrt{s}$ =250 GeV (Figure 2.2). This two–body final state offers a model independent way of measuring the properties of the Higgs boson. By precise reconstruction of the Z bosons kinematics and knowledge of the initial state of the collision, all the properties of the Higgs boson can be inferred without the need of a particular model of the Higgs boson decay. This so called *recoil mass technique* allows measurements on the mass and the total and invisible decay width of the Higgs boson [15]. The low background environment also allows the reconstruction of all visible final states of a decaying Higgs boson. A significant fraction of those is not accessible at hadron colliders since the irreducible hadronic background interferes with hadronic decay modes. Besides guaranteed results on the properties of the Higgs boson, the efforts will also be dedicated to precision searches for deviations from the standard model. These may manifest themselves in the coupling of the Higgs boson to other standard model particles or in higher order loop corrections to standard model processes. The future precision is needed to access these minor effects. This could open the path for a possible experimental confirmation of extensions to the Higgs sector like composite models or various super symmetries already formulated in theory but currently without experimental proof or disproof.

Going to higher center of mass energies of 500 GeV and beyond, measurements on the Higgs self-coupling parameter in the (e$^+$e$^-$ → ZHH) and (e$^+$e$^-$ → HH$\nu_e\overline{\nu_e}$) processes and on models including an extended Higgs sector [17], like the Minimal Supersymmetric

Standard Model (MSSM) [18], become possible. At this point the expected physics reach would allow complementary measurements also on Dark Matter models to establish connections to cosmological observations like baryogenesis or weakly interacting massive particles (WIMPs) [15].

The Higgs Factory - A Concept for Future e^+e^- Colliders

In contrast to hadron colliders, e^+e^- colliders are well suited to precisely reconstruct complete hadronic final states in a high energy environment because they are not shadowed by hadronic background events. Additionally, leptons are no composite particles so their initial momentum does not follow a potentially broad distribution[1] but can be well prepared. This section discusses the physics potential and introduces concepts of possible future e^+e^- colliders.

As of now, a single candidate for a future e^+e^- colliders is not chosen, but several different scenarios are being discussed. FCC-ee [19] and CEPC [20] are two circular colliders proposed to be built at CERN and in China, respectively. The advantage of having a circular machine is the conceptually high luminosity and the reusability of the beam after collision. Since only a very small fraction of the particles in two colliding bunches actually interact, the remaining particles circulate again and collide at the interaction region multiple times. Furthermore, the same accelerating structure can be reused to step-wise accelerate the particles to the nominal energy. A major disadvantage of circular machines, however, is the emission of *synchrotron radiation* [21] which limits the maximum achievable collision energy. Any charged particle forced to circulate in a magnetic field emits electromagnetic radiation with a power of $P \propto E^4/r^2m^4$, with m being the particles mass and r being the radius. For FCC-ee and a radius of 100 km this means a maximum center of mass energy of 365 GeV. The reason for this is the limit of emitted power which has to be kept below 50 MW per beam, while the energy of the radiation emitted towards the experiments has to be kept below 10 keV to reduce background [19]. Besides the circular machines the linear colliders ILC [22] and CLIC [7] are proposed to be built in Japan and at CERN respectively. The striking advantage of a linear machine is the extremely reduced power of synchrotron radiation giving access to higher center of mass energies. Its maximum is only determined by the length of the accelerator and the accelerating gradient. Since particles are not re-used, the luminosity at low energies is lower than for circular colliders. Different accelerating structures are proposed for the two scenarios. ILC uses superconducting cavities, similar to the ones used at the XFEL accelerator at DESY [23], which offer an accelerating gradient of $30\,\mathrm{MV\,m^{-1}}$. At the first stage of operation the two main accelerators will have a combined length of 22 km to deliver the beams at a maximum collision energy of 250 GeV to realize a Higgs Factory. Upgrade plans foresee a step wise increase to 1 TeV [6]. For CLIC a novel two-beam acceleration is being designed to reach higher accelerating gradients and therefore reduce the length of the accelerator. The planned accelerating gradient

---

[1]When colliding composite particles like hadrons at high energy, the actually colliding particles are the partons. The total momentum of the hadron is distributed among the partons following a parton distribution function. Therefore the initial state of the collision is never known exactly.

at the first stage of operation is planned to be $72\,\mathrm{MV\,m^{-1}}$. With a main accelerator length of $11.4\,\mathrm{km}$ this results in an nominal collision energy of $380\,\mathrm{GeV}$ with upgrade plans to $3\,\mathrm{TeV}$ [7]. In contrast to circular colliders, the accelerated particles are delivered in bunch trains and are lost after crossing at the interaction point. At CLIC, bunches trains with 352 bunches per train are brought to collision at a frequency of $50\,\mathrm{Hz}$ [7]. The setup of a linear collider consequently offers only one interaction point where an experiment can be placed, while a circular collider can supply multiple detectors with particles. The commitment to a specific collider scenario depends strongly on the desired measurement program and is discussed among the collider communities at the moment. The core measurement programs of Higgs factory and top quark threshold scan [24] are possible in any scenario but decisions have to be made concerning further physics goals, their technical requirements and the available resources and funding.

Detector Requirements

In order to fully exploit the clean environment at these lepton colliders the detectors have to be capable of identifying and reconstructing each particle in a final state. Especially the hadronic decays of the Higgs and electroweak gauge bosons $(\mathrm{H}, \mathrm{W}^{\pm}, \mathrm{Z} \to \mathrm{q}\bar{\mathrm{q}})$ need to be resolved to achieve the desired precision on the Higgs parameters. Since these decays form two jets in the detectors, that are not necessarily well separated in space, the position resolution has to be high enough to reliably separate them and reconstruct the flavor of the final state quark. While the tracking detectors typically offer excellent position resolution, also the calorimeters need to be finely segmented in order to associate the tracks emerging from the vertex to the energy depositions in them. This ability also aids the so called Particle Flow paradigm of event reconstruction [25]. The goal is the precise assignment of particle signatures to the sub-detector that is best suited for measuring their energy. This reasoning led to developments like the highly granular calorimeter prototypes developed by the CALICE collaboration. The Analog Hadronic CALorimeter (AHCAL) is a finely segmented, cubic meter scale detector prototype that will be discussed in more detail throughout this thesis. An additional benefit of this device is the single cell time stamping capability to separate and cluster the energy depositions in the detector not only in the three spatial coordinates, but also in the time domain. This enables the separation of overlapping signatures in space coming from two different events separated in time. Modern calorimeter designs target a time resolution at the order of 10 to $100\,\mathrm{ps}$ on the particle level.

2.3 Precision Neutrino Physics – The DUNE Experiment

In the standard model, the neutrinos are a priori massless. The observation of neutrino oscillation in the late 1990s [26], however, implies the existence of neutrino masses. The exact value of the individual masses cannot be measured via oscillations, because experiments investigating the oscillation behavior are only sensitive to the squared mass difference between two mass eigenstates of the neutrino. Consequently, the ordering of

these eigenstates is ambiguous. Furthermore, the underlying theory includes a source of CP-violation which is not yet quantified precise enough to confirm its occurrence in the neutrino sector. This section provides an overview of the Deep Underground Neutrino Experiment (DUNE) [27] and motivates the scientific program according to the theoretical background of neutrino oscillations. Particular attention is payed to the Near Detector which is the subject of a study conducted in the course of this thesis.

Overview

DUNE is a next-generation long-baseline neutrino experiment hosted at the Fermi National Accelerator Laboratory in Chicago, Illinois. Its main scientific goals are the determination of the neutrino mass hierarchy and the measurement of CP-Violation in the neutrino sector. The experiment will use protons from the Fermilab accelerator complex to generate a muon neutrino or muon anti-neutrino beam of unprecedented intensity. The beam energy ranges primarily from $0.5\,\mathrm{GeV}$ to $5\,\mathrm{GeV}$. The properties of this beam are measured at two detectors, the Near Detector (ND) and the Far Detector(FD), to precisely investigate the oscillation behavior of the neutrinos. The ND is located underground at Fermilab, the FD at the Sanford Underground Research Facility (SURF), separated by a baseline of $1300\,\mathrm{km}$. An illustration of the experiment is shown in Figure 2.3.
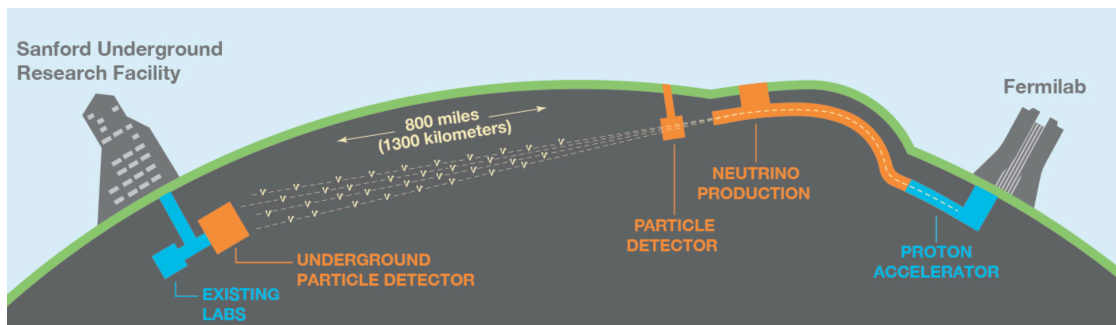
Figure 2.3: Sketch of the experimental setup of DUNE. Initially, protons are accelerated at Fermilab, Chicago. After guiding them along an arc and pointing them along the final beam direction, they are hitting a neutrino production target. The resulting muon neutrino beam reaches the first particle detector which characterizes its content and energy spectrum. After propagating through the earths crust for about $1300\,\mathrm{km}$ the neutrinos hit the second detector in Sanford, where the oscillated beam is characterized again to measure the electron neutrino appearance. Taken from [28].

The main observable of the experiment is the ratio of electron neutrinos to muon neutrinos in the FD, the so called electron neutrino appearance. The main scientific goals are precise measurements of the neutrino mixing angles, finding evidence for leptonic CP violation and the determination of the neutrino mass hierarchy. Ancillary measurements include the search for proton decay, observations on supernovae and further investigation

of various BSM models. The following section provides the theoretical treatment of neutrino oscillations with special attention to the observable effects relevant for DUNE.

The Physics of DUNE - Neutrino Oscillations

The general concept of neutrino oscillation describes a flavor change of the neutrino as it travels through space-time. A neutrino created with a specific *flavor eigenstate* in an arbitrary reaction has a non-zero probability to be detected in a different flavour eigenstate after some time. Initially, this mechanism was proposed by Pontecorvo in 1968 [29] as a solution to the solar neutrino problem and was confirmed experimentally in the early 2000s by the SNO experiment [30]. The solution is based on the quantum mechanics of a system of mixed states. The flavour eigenstates of the neutrino are interpreted as a superposition of three *mass eigenstates*:

$$\begin{pmatrix} \nu_e \\ \nu_\mu \\ \nu_\tau \end{pmatrix} = U_{PMNS} \cdot \begin{pmatrix} \nu_1 \\ \nu_2 \\ \nu_3 \end{pmatrix}. \tag{2.1}$$

In this equation, ν_e, ν_μ and ν_τ denote the flavor eigenstates, ν_1, ν_2 and ν_3 denote the mass eigenstates and U_{PMNS} is the so-called Pontecorvo-Maki-Nakagawa-Sakata matrix (PMNS) [31]. It is fully described by three mixing angles (θ_{12}, θ_{23}, θ_{13}) and one complex phase δ_{CP}:

$$\begin{pmatrix} U_{e1} & U_{e2} & U_{e3} \\ U_{\mu 1} & U_{\mu 2} & U_{\mu 3} \\ U_{\tau 1} & U_{\tau 2} & U_{\tau 3} \end{pmatrix} = \begin{pmatrix} c_{12}c_{13} & s_{12}c_{13} & s_{13}e^{-i\delta_{CP}} \\ -s_{12}c_{23} - c_{12}s_{13}s_{23}e^{i\delta_{CP}} & c_{12}c_{23} - s_{12}s_{13}s_{23}e^{i\delta_{CP}} & c_{13}s_{23} \\ s_{12}c_{23} - c_{12}s_{13}s_{23}e^{i\delta_{CP}} & -c_{12}c_{23} - s_{12}s_{13}c_{23}e^{i\delta_{CP}} & c_{13}c_{23} \end{pmatrix}.$$

Here, $s_{ij} = \sin\theta_{ij}$, $c_{ij} = \cos\theta_{ij}$ and i denotes the imaginary unit. By investigating the quantum mechanical time evolution of the flavor eigenstates [32], one can derive expressions for the transition probability between these states. The main oscillation channel DUNE will use to conduct the planned studies is $\nu_\mu \to \nu_e$. It is parameterized by

$$\begin{aligned} P_{\nu_\mu \to \nu_e} \simeq & -4 \sum_{k>j} \text{Re}\left[U_{\mu k}^* U_{ek} U_{\mu j} U_{ej}^* \right] \sin^2 \left(\frac{\Delta m_{kj}^2 L}{4E_\nu} \right) \\ & + 2 \sum_{k>j} \text{Im}\left[U_{\mu k}^* U_{ek} U_{\mu j} U_{ej}^* \right] \sin^2 \left(\frac{\Delta m_{kj}^2 L}{2E_\nu} \right), \end{aligned} \tag{2.2}$$

where Δm_{kj}^2 is the squared mass difference between mass eigenstate j and k, E_ν is the neutrino energy, L is the distance between origin and detection of the neutrino (the baseline) and $U_{\alpha k}$ are the PMNS matrix elements, with $\alpha \in [e, \mu, \tau]$. It becomes apparent that oscillations are only possible for a non-zero squared mass difference, and that the oscillation frequency scales with the squared mass difference and the neutrino energy. Performing a CP transformation [2] on Equation (2.2) implies a complex conjugation of

---

[2] A CP transformation replaces all particles with their anti-particles and inverts all spatial coordinates.
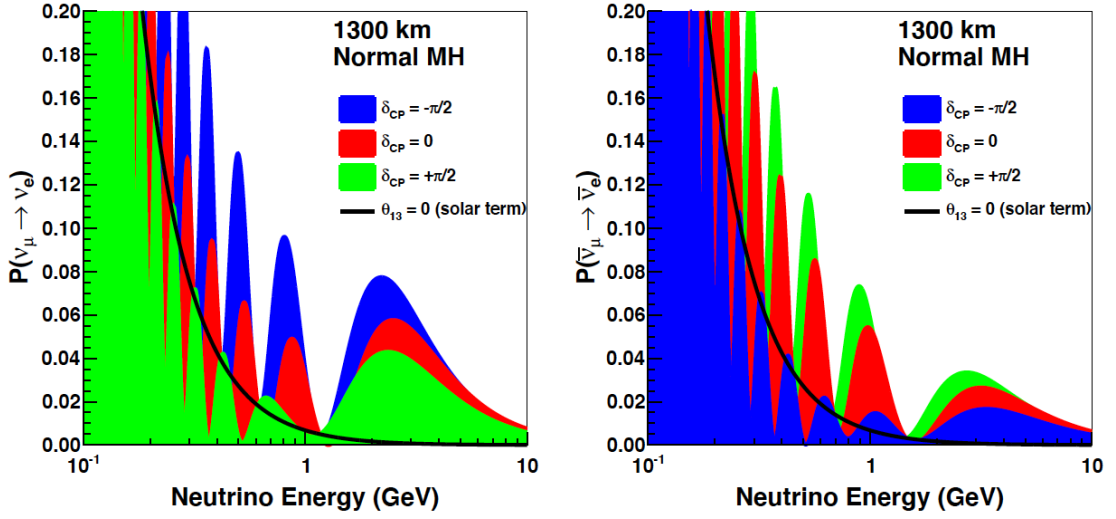
Figure 2.4: Transition probability from muon neutrino to electron neutrino (left) and muon anti-neutrino to electron anti-neutrino (right) for $\delta = \pm\pi/2$ and $\delta = 0$. Besides the different oscillation patterns for different values of δ, the pattern also varies between neutrinos and anti-neutrinos. Taken from [33].

the PMNS matrix elements and thus leads to a change in the transition probability for all oscillations involving Θ_{13}, because the corresponding matrix elements depend on $i\delta_{CP}$. This shows that the theory of neutrino oscillation provides a source of CP violation since neutrinos and anti-neutrinos follow different oscillation patterns for a non-zero δ_{CP}. DUNE makes use of this by running the experiment in neutrino and anti-neutrino mode to measure the value of δ_{CP}. An illustration of the oscillation probability at the energy range and baseline of DUNE is shown in Figure 2.4.

The transition probability described by Equation (2.2) is only valid for propagation of the neutrinos in vacuum. Since the beam used for DUNE will propagate through the earths crust, the probability is changed due to the presence of electrons in the traversed matter. This is known as the Mikheyev–Smirnov–Wolfenstein (MSW) effect [34]. The electron neutrino component of the mass eigenstates undergo coherent charged current forward scattering with the surrounding electrons. This introduces a matter potential in the quantum mechanical treatment leading to an enhancement of the effective mass of the eigenstates. A detailed derivation is for example shown in [32]. The modified mass leads to a modified transition probability. By substituting the explicit expressions of the

PMNS matrix, the probability reads [35]:

$$P_{\nu_\mu \to \nu_e} \approx \sin^2(\theta_{23}) \sin^2(2\theta_{13}) \frac{\sin^2(\Delta_{32}(1-x))}{(1-x)^2}$$
$$+ \alpha J \cos(\Delta \pm \delta) \frac{\sin(\Delta x) \sin(\Delta(1-x))}{x(1-x)} \qquad (2.3)$$
$$+ \alpha^2 \cos^2(\theta_{23}) \sin^2(2\theta_{12}) \frac{\sin^2(\Delta x)}{x^2}.$$

Here, $J = \cos(\theta_{13}) \sin(2\theta_{13}) \sin(2\theta_{12}) \sin(2\theta_{23})$, $\alpha = \Delta m_{21}^2 / \Delta m_{22}^2$ and $\Delta = \Delta m_{23}^2 L / 4E_\nu$. The plus (minus) sign applies to muon (anti-) neutrino transition. The parameter x describes the contribution from the MSW effect. It reads

$$x = \pm 2\sqrt{2} G_F N_e E_\nu / \Delta m_{23}^2, \qquad (2.4)$$

where G_F is the Fermi constant and N_e is the electron number density of the medium the neutrino traverses. The sign of x is connected to the mass ordering of the neutrinos. As mentioned in Section 2.1, the absolute masses of the neutrinos can not be inferred from measurements of the transition probability, because they are scaling only with mass differences. Due to the modification of the vacuum oscillation by the matter potential of the MSW effect, the probability of electron neutrino appearance is changed for particles and anti-particles. Especially the states ν_1 and ν_2 are affected because of their larger electron neutrino admixture. This effect can be understood by expressing the mass eigenstates as a superposition of flavor eigenstates according to Equation (2.1):

$$|\nu_k\rangle = U_{ek}^* |\nu_e\rangle \cdot U_{\mu k}^* |\nu_\mu\rangle \cdot U_{\tau k}^* |\nu_\tau\rangle. \qquad (2.5)$$

An overview of the possible orderings of the mass eigenstates with their currently known flavor admixtures is shown in Figure 2.5. Observations of the solar neutrino flux determined the order of $\Delta m_{12}^2 = \Delta m_{sol}^2$ using the MSW effect in the sun [32], the sign of $\Delta m_{23}^2 = \Delta m_{atm}^2$ is not determined up to now. The primary oscillation mode for the DUNE experiment (Equation (2.2)) is sensitive to this mass splitting, but to disentangle this effect from the contribution of δ_{CP}, the baseline L and the neutrino energy have to be chosen adequately to tune $\Delta \sim \pi/2$. Figure 2.6 shows the transition probability for different baselines over a range of neutrino energies .
At baseline of 810 km the effect becomes significant. DUNEs baseline is fixed at about 1300 km which enables the experiment to disentangle the effect of δ_{CP} and Δm_{23}^2 on the oscillation pattern. In order to fully exploit the exceptionally long baseline, the neutrino energies have to be known, well controlled and should also cover multiple oscillation maxima. Therefore, the Long Baseline Neutrino Facility (LBNF) was implemented to generate the worlds most intense, high energetic and brilliant muon (anti-)neutrino beam.

The Neutrino Beam

To generate the neutrino beam, the first step is the acceleration of protons using Fermilabs accelerator infrastructure. After reaching the nominal energy between 60 GeV and
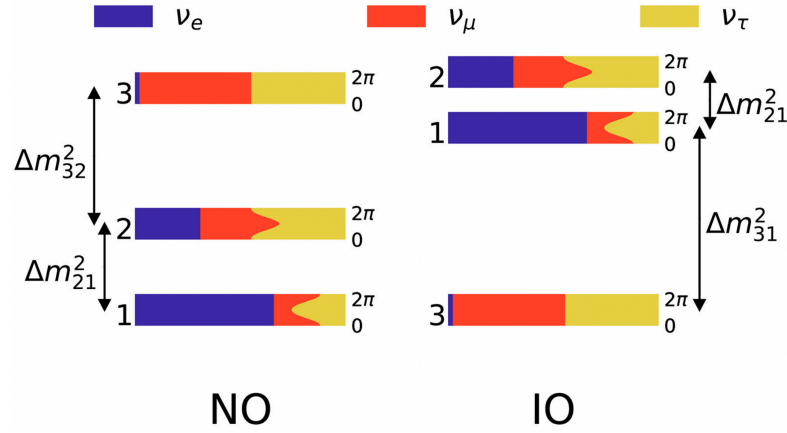
Figure 2.5: The two possible orderings of the mass eigenstates along with their flavour composition. The ordering of ν_1 and ν_2 was fixed by solar neutrino experiments. The order of ν_2 and ν_3 is ambiguous and pursued by modern long baseline neutrino experiments. The resulting possibilities are called "Normal" (NO) and "Inverted" (IO) order. The colors encode the admixture of electron, muon, and tau flavour of the respective mass eigenstate. This composition is expected to change with respect to the value of δ_{CP}. Taken from [36].
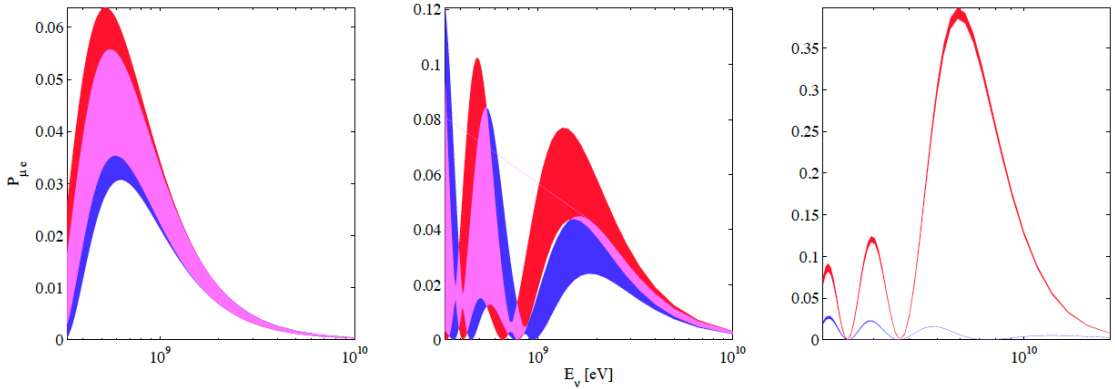
Figure 2.6: Transition probability from muon neutrino to electron neutrino in terms of energy. From left to right, the different probabilities at distances of 295 km, 810 km and 7500 km are shown. Red indicates the normal ordering, blue the inverted ordering and the bandwidth is obtained by varying the value of δ_{CP}. One can observe that the difference between orderings increases with rising distance. Dune's baseline is 1300 km, so the separation of the orderings is clearly visible. The probabilities for muon anti-neutrino to electron anti-neutrino oscillation are similar, but with interchanged mass orderings. Taken from [37].
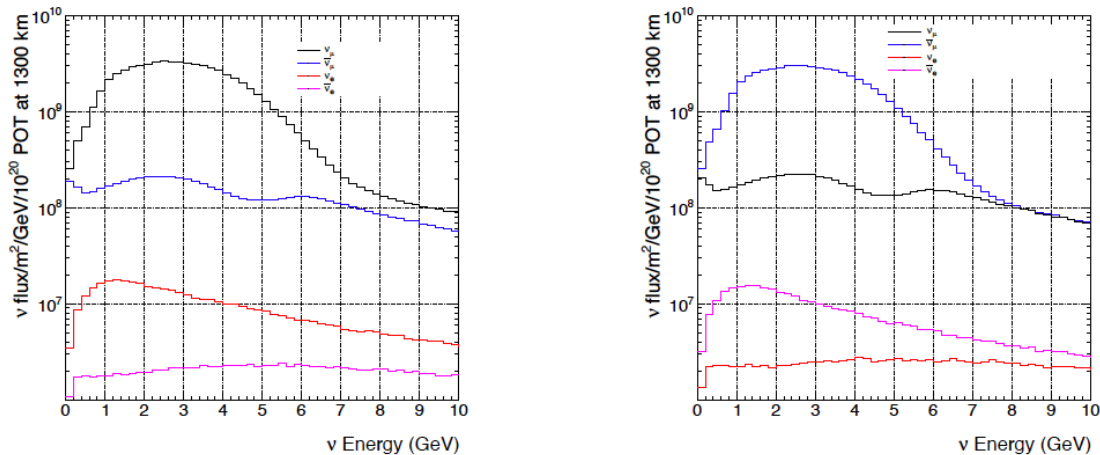
Figure 2.7: Predicted neutrino flux and beam composition. The left histogram shows the flux for muon neutrino mode, the right one shows muon anti-neutrino mode. The residual contamination of electron neutrinos and anti-neutrinos is also shown. Taken from [33].

120 GeV [38], they are pointed onto a graphite target to produce charged mesons. These mesons, mostly pions and kaons, are focused by carefully designed magnetic horns to reach the desired intensity. This stage is critical since the high radiation dose from the proton beam requires reliable cooling and radiation monitoring, and is directly responsible for the generation of the wide-band neutrino beam required for DUNEs physics program. After passing the horns the mesons are guided down an evacuated pipe where they decay into muons and muon neutrinos. By selecting the charge of the mesons, one can select the production of neutrinos or anti-neutrinos. Finally, the beam enters the absorber hall where the residual hadrons and muons are removed and the neutrinos travel to the near and far detectors.

The facility is designed to deliver a beam power of 1.2 MW with a potential upgrade to 2.4 MW [38]. Since the first and second oscillation maxima are expected to be approximately at 2.4 GeV and 0.8 GeV, the beamline is optimized to deliver the peak neutrino flux at energies from 0.5 GeV to 5 GeV as shown in Figure 2.7. The neutrino production is tuned to deliver a pure muon (anti-)neutrino beam, but due to inefficiencies in the sign selection, suppressed decay modes of the mesons and muon decay the resulting beam will be contaminated by electron (anti-)neutrinos. One of the main tasks of the Near Detector is the characterization of the beam to determine its initial composition and energy spectrum.

The Near Detector

Designed as a multi–purpose detector system, the main task of the Near Detector (ND) is the characterization of the beam before oscillation and the constraining of

systematic uncertainties for oscillation studies. Furthermore, it is vital to extrapolate the neutrino flux from the near to the far detector and to perform precision measurements on neutrino–nucleon cross sections. The current concept of the DUNE ND consists of three independent sub-detectors with different specializations. The first detector in the beam line is a liquid argon time projection chamber (TPC) (ND–LAr [39]) featuring the same target material as the far detector but with smaller drift volume and finely segmented readout. The small drift volume enables a good spatial resolution by limiting the diffusion of electrons as they drift towards the TPCs sense wires. By using the same target material as the far detector, systematic errors of the flux extrapolation to the far detector can be canceled. Second in the beam line is a high pressure gaseous argon TPC which is placed downstream of ND–LAr, called ND–GAr. This TPC is surrounded by an electromagnetic calorimeter and a solenoid magnet creating a magnetic field normal to the beam direction. The return yoke of the magnet is eventually equipped with a muon detector. ND–GAr is designed to perform high precision measurements on the energy spectrum of the neutrino beam, as well as on cross sections of rare neutrino interactions. The system provides full hermeticity and excellent momentum resolution because of the magnetized TPC and the low detection threshold in the gas TPC. The baseline calorimeter design features a highly granular scintillator part in the innermost layers to increase the particle separation capability and angular resolution, followed by layers equipped with crossed scintillator strips. Previous studies [40] have shown that the spatial resolution in the innermost layers is especially important for the angular resolution of the system, so this hybrid design offers a possibility to reduce the channel count and therefore the cost. Since ND-GAr is the subject for parts of the studies in this thesis, it is covered in more detail in Chapter 7. The third detector, called System for On-Axis Neutrino Detection (SAND) [39], consists of a tracking detector, surrounded by a lead-fiber ECAL and a magnet, recycled from the KLOE detector [41]. This system offers complementary energy spectrum measurement with high neutron detection efficiency. This detector will stay on the axis of the neutrino beam for the full runtime of the experiment, while ND–GAr and ND–LAr will be moved off-axis on a rail system within the DUNE-PRISM [42] project. Due to the relativistic pion decay kinematics the energy spectrum of the produced neutrinos sharpens for increasing off-axis angles. This enables the detectors to investigate neutrino interactions in specific energy intervals and focus on individual event topologies. Figure 2.8 shows an engineering drawing of the underground near detector complex.

The Far Detector

While the ND characterizes the un-oscillated muon (anti-)neutrino beam the Far Detector (FD) measures its composition again, after it traversed the baseline. The primary goal is the estimation of electron neutrino appearance in the muon neutrino beam, caused by oscillation as explained in Section 2.3. The FD consists of four liquid argon TPCs placed 1.5 km underground in the Sanford mine. The detector has to be able to identify the electron, produced by the electron neutrino interaction with the argon, to perform the appearance measurement. Different read out strategies of the TPCs exist, including
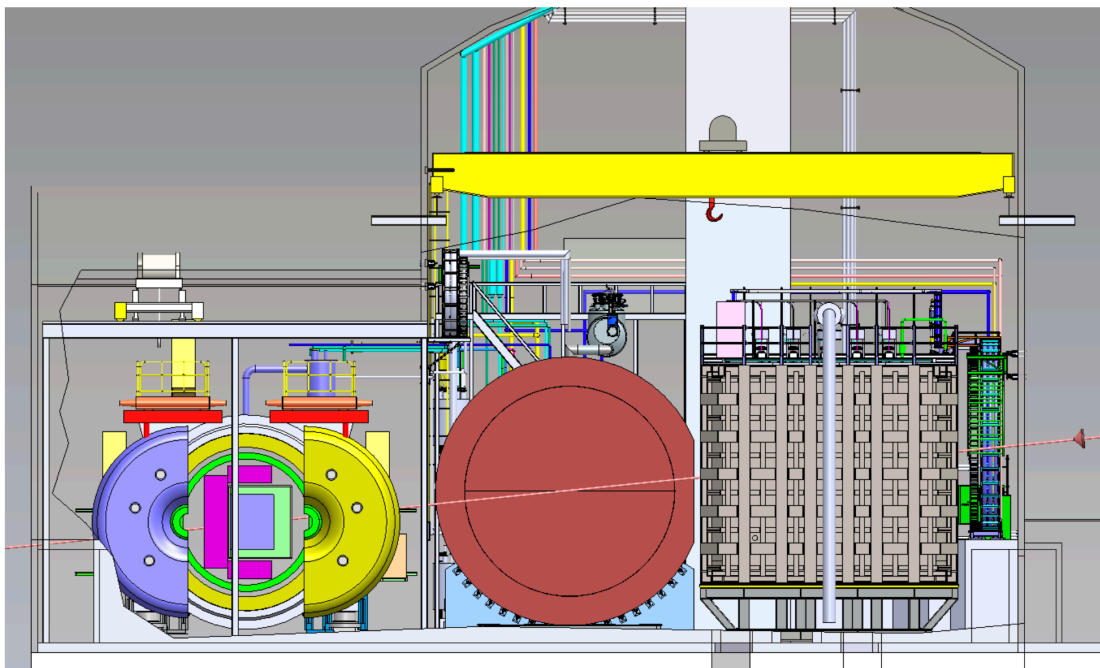
Figure 2.8: The DUNE Near Detector complex. The first detector on the right is ND-LAr, a liquid argon TPC. The middle one, called ND-GAr, consists of a magnetized high pressure gaseous argon TPC surrounded by an ECAL and a muon detector. SAND, the System for on-Axis Neutrino Detection, is located on the right. It is a magnetized scintillator tracker surrounded by an ECAL. The beam direction is shown as a red arrow entering from the right. Taken from [43].

vertical drift coupled with photon detectors to pick up scintillation light from the liquid argon, as well as horizontal drift featuring crossed anode and cathode wire planes. Those are submerged in the argon to provide a constant electric drift field and to collect the charges produced by traversing charged particles. The drift time to the wires is used to perform a 3D reconstruction of the event, the collected charge is proportional to the deposited energy. A complete overview over the FD is provided in [28].

Sensitivity to Oscillation Parameters

Among the primary scientific goals of DUNE are precise measurements of neutrino oscillation parameters. As introduced in Section 2.3 the experimental setup allows investigation especially of δ_{CP} and the sign of Δm_{31}^2. The sensitivity to these parameters can be extrapolated as a function of kt·MW·year, a measure of how much beam power the FD will be exposed to over several years, given its fiducial mass. This allows an estimation of the minimum runtime of the experiment. Figure 2.9 shows the projected significance of the mass hierarchy determination for different values of δ_{CP} for an exposure
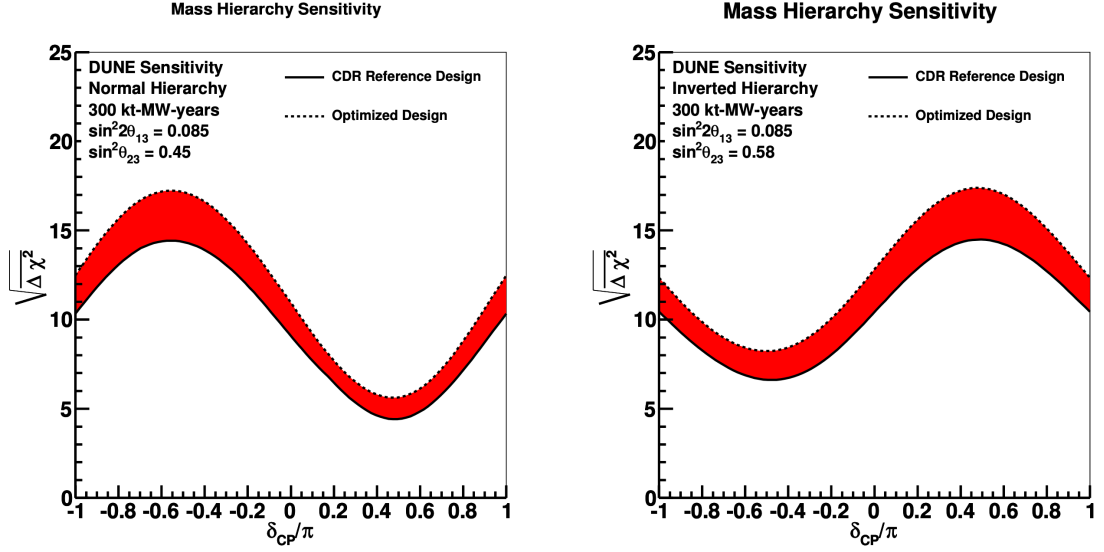
Figure 2.9: Sensitivity to the mass hierarchy for an exposure of 300kt·MW·year for different values of δ_{CP}. The left plot shows normal hierarchy, the right plot shows inverted hierarchy. The solid line represents the projection for the CDR reference design, the dashed line accounts for possible detector improvements over the course of further optimization efforts. Taken from [33].

of 300kt·MW·year. This corresponds to a runtime of 7 years given a beam power of 1.07 MW and a FD fiducial mass of 40 kt [33]. For this exposure the mass hierarchy can be determined at a statistical significance of $\sqrt{|\Delta\chi^2|} = 5$ for the full range of δ_{CP} values corresponding to a 5σ discovery.

A similar projection can be performed for the sensitivity to the value of δ_{CP} which is shown in Figure 2.10 for the same exposure of 300kt·MW·year for normal and inverted mass hierarchy [33]. This shows, that the experiment is most sensitive to maximal CP violation around $\delta_{CP} \sim \pm\frac{\pi}{2}$, because the sensitivity naturally drops to zero towards vanishing CP violation.

Additionally, DUNE will be able to improve the precision of the neutrino mixing angles, particularly $\sin^2(\Theta_{23})$, which will in turn improve the precision of independent measurements that take this value as input to the tested model. An overview of the projected precision is given in [33].

2.4 Common Requirements for Technological Developments

As explained in the previous sections the trend in modern calorimeter design goes towards high spatial granularity and unprecedented time resolution. Regardless of the research field, neutrino physics or collider experiments, these features offer benefits for precision
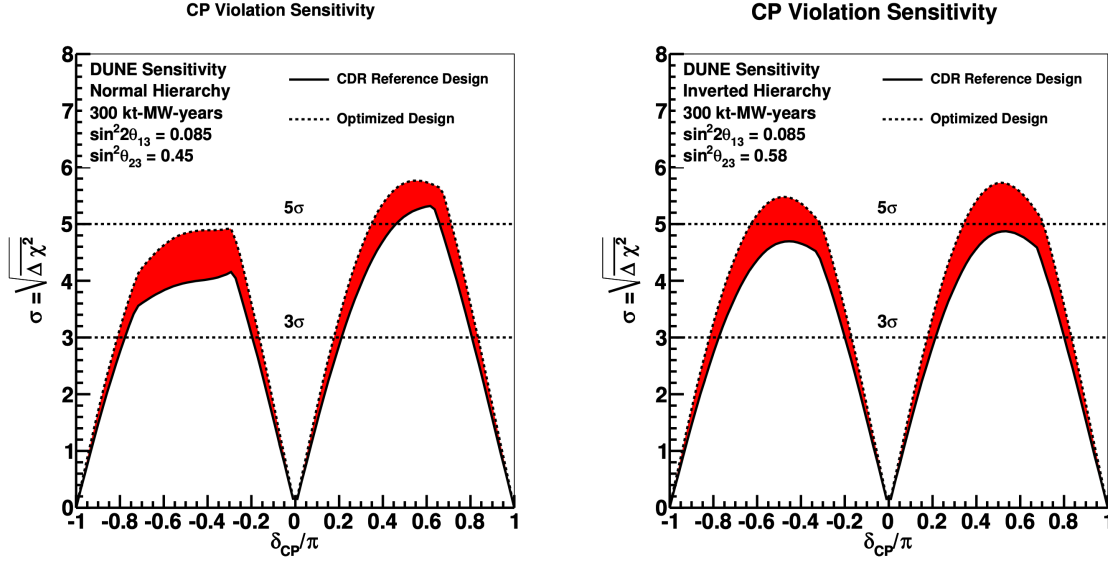
Figure 2.10: Sensitivity to the value of δ_{CP} for an exposure of 300kt·MW·year for normal (left) and inverted (right) hierarchy. In both cases the maximum sensitivity is expected around maximal CP violation of $\delta_{CP} \approx \pm\frac{\pi}{2}$. Taken from [33].

measurements. In most experiments, high precision goes along with large data samples. In order to optimize for the runtime of the experiment these samples have to be recorded at a sufficient rate, implying high intensity particle beams and increased background rates. In these scenarios, high granularity will increase the efficiency and quality of the data collection on interesting but rare processes since modern data analysis tools like machine learning and artificial neural networks exploit the detailed information produced by those devices. Their development, however, poses technical challenges arising from the unprecedented channel count and data sizes. Calibration procedures of these detectors are very involved and produce millions of constants to reduce the inevitable channel by channel deviations in the response. The data aggregation and read-out has to be able to cope with the generated information and requires high-speed transfer of data and sophisticated means of data reduction, commonly built into the detector before the data is transferred to mass storage. This thesis addresses some of the topics by reporting on the calibration procedure and timing performance of the CALICE AHCAL prototype built for applications in future collider experiments. Furthermore, a simulation study on particle separation with the highly granular calorimeter concept of the DUNE ND is shown, which exploits the benefits of high granularity and time resolution.

Chapter 3

Calorimetry

Advances in instrumentation are crucial for the success of future High Energy Particle physics (HEP) experiments. Both in high energy and high precision experiments, the energy of particles emerging from the processes under study is a key observable. The calorimeter, a specialized detector to measure the energy of particles, has been and still is a irreplaceable device in HEP experiments. This chapter introduces the basic principles of calorimetry by explaining the mechanisms of the interactions, different particle species can undergo with the detector material. Furthermore, means of signal generation and extraction are discussed.

3.1 Interactions of Particles with Matter

To tailor a calorimeter to the demands of a particular experiment, it is vital to understand the processes through which a particle can interact with matter and transfer energy to it. The following section will introduce the most important processes for calorimetric purposes.

Heavy Charged Particles

Heavy charged particles, like muons, mainly loose their energy by ionization and excitation of the electrons in the material they traverse. The mean rate of energy loss per unit length is described by the Bethe-Bloch equation [44] and reads

$$-\left\langle \frac{dE}{dx} \right\rangle = K z^2 \frac{Z}{A} \frac{1}{\beta^2} \left[\frac{1}{2} ln \left(\frac{2 m_e c^2 \beta^2 \gamma^2 T_{max}}{I^2} \right) - \beta^2 - \frac{\delta(\beta\gamma)}{2} \right]. \tag{3.1}$$

K is a constant, z is the charge number of the traversing particle, Z is the charge number and A the mass number of the material, I is the mean excitation energy of the material, T_{max} is the maximum kinetic energy transfer to an electron in the material and $\delta(\beta\gamma)$ is the density effect correction. Up to an accuracy of a few % the equation is valid in a region of 0.1< $\beta\gamma$ < 1000, with $\beta\gamma = p/Mc$ [45]. Figure 3.1 shows the loss rates for different particles and elements. The energy loss is high for particles with low momentum before decreasing to a minimum at 2< $\beta\gamma$ <3. Particles in this region are called "Minimum Ionizing Particle" (MIP). Because of this well defined energy deposition, MIP-like muons are a convenient way to calibrate a calorimeter.
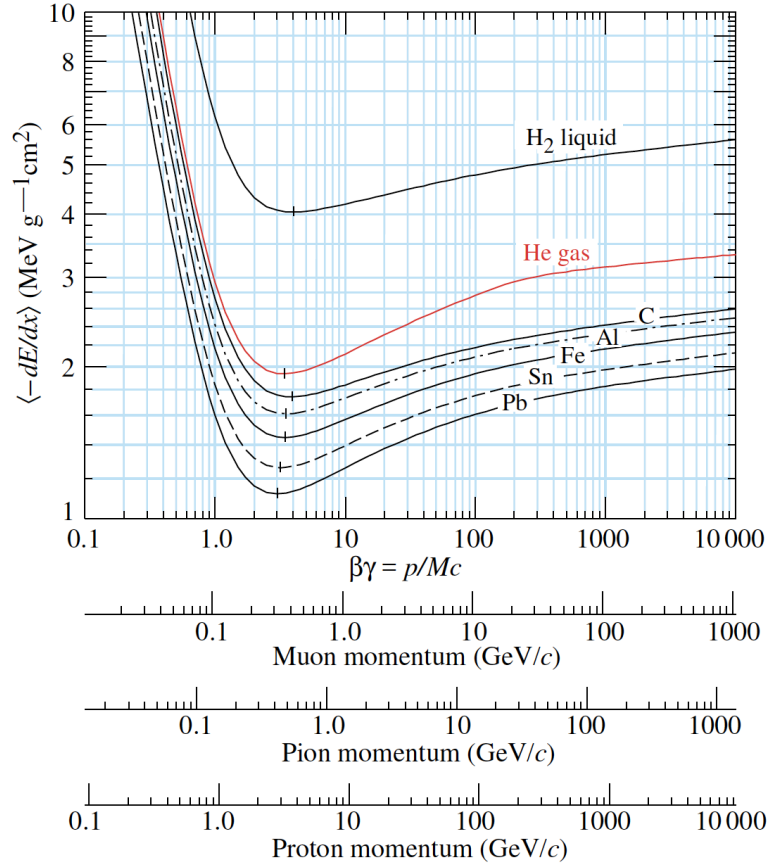
Figure 3.1: Stopping power $-\langle \frac{dE}{dx} \rangle$ for different materials. Taken from [45].

Electrons and Positrons

The interesting interactions of electrons and positrons for calorimetric purposes are illustrated in Figure 3.2. At energies below 10 MeV the energy is predominantly deposited by ionization and excitation of the nuclei in the detector material. Low momentum scattering processes like Möller ($e^- e^- \rightarrow e^- e^-$) and Bhabha ($e^+ e^- \rightarrow e^+ e^-$) scattering play a minor role. At energies above 10 MeV bremsstrahlung becomes dominant. The electron radiates photons while traversing the coulomb field of a nucleus and is gradually decelerated. The energy spectrum of the radiated photons decreases with $1/E$, thus the majority of the photons carry away a small fraction of the electrons energy. An overview of these processes is shown in Figure 3.2.

The energy loss of an electron via bremsstrahlung relates to its energy by [46]

$$-\frac{dE}{dX} = \frac{E}{X_0}. \tag{3.2}$$

The parameter X_0 is called *radiation length* and quantifies the mean distance after which an electron has lost all but 1/e of its incident energy. The radiation length is a material
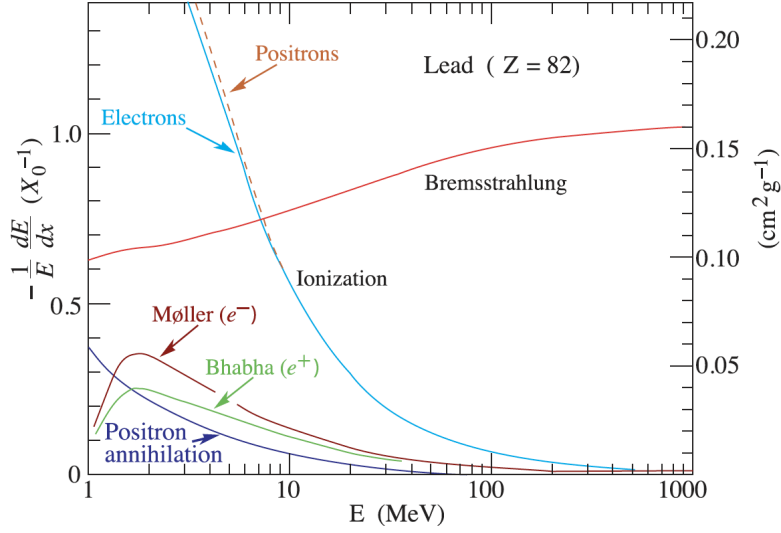
Figure 3.2: Energy loss per radiation length of electrons and positrons in lead as a function of particle energy. In the low energy region scattering and ionization are the dominant processes. From the critical energy ($\sim 8\,\mathrm{MeV}$) up to higher energies, the energy loss is dominated by bremsstrahlung. Taken from [45].

property and is approximated by [47]

$$X_0 \approx \frac{716.4A}{Z(Z+1)\ln\left(\frac{287}{\sqrt{Z}}\right)}\left[\frac{g}{cm^2}\right], \tag{3.3}$$

with A and Z being mass and atomic number of the respective element. In the case of a mixture of N different elements, the radiation length is calculated according to their volume fractions:

$$X_0 = \sum_{n=0}^{N} \frac{V_i}{X_i} \tag{3.4}$$

where V_i and X_i are the volume fraction and the radiation length of the ith element. The energy at which the loss by bremsstrahlung equals the ionization loss is called *critical energy* E_c and plays an important role in the development of electromagnetic showers discussed in Section 3.1.1.

Photons

The energy loss of photons in matter depends on their energy and can be subdivided into three regions shown in Figure 3.3. In the sub-MeV range the dominant process is the photoelectric effect leading to total absorption of the photon. For kinetic energies of 1 MeV to 10 MeV compton scattering [48] becomes dominant. This process transfers a fraction of the photons energy to an electron of the surrounding medium. For even higher energies, the dominant process is the creation of an electron-positron pair while
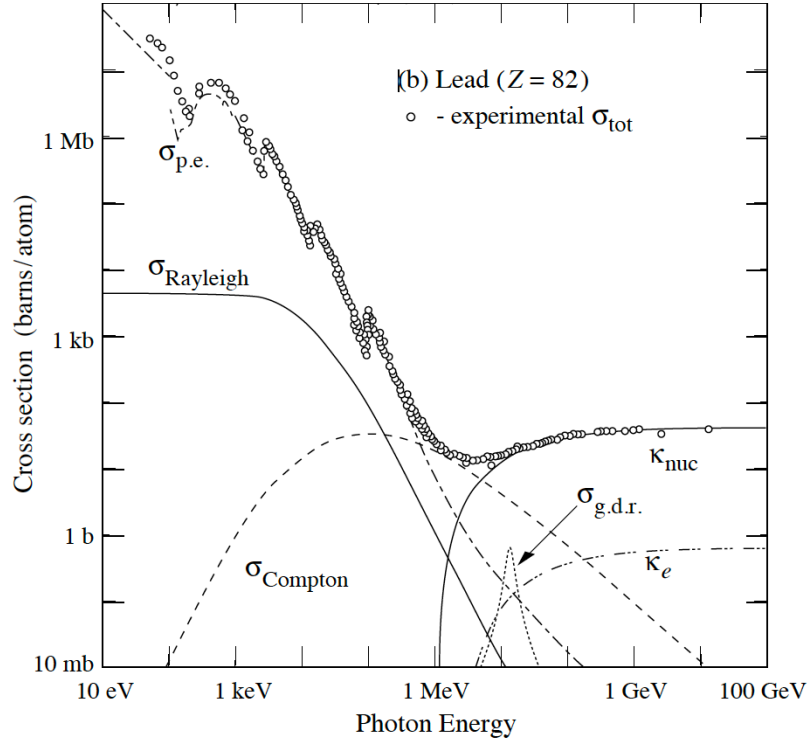
Figure 3.3: Total cross section of photons in lead. Photoelectric absorption ($\sigma_{p.e.}$)is dominant up to an energy of 1 MeV. In the intermediate range from 1 MeV to 10 MeV, compton scattering becomes the dominant process followed by pair-production in nuclear (κ_{nuc}) and electron (κ_e) coulomb fields. The dotted line at 10 MeV resembles the great dipole resonance ($\sigma_{g.d.r.}$), breaking up the lead nucleus. Taken from [45].

traversing the nuclear coulomb fields.

It can be shown that the cross section for photon interactions in the high energy limit is given by

$$\sigma(E \rightarrow \infty) = \frac{7}{9} \frac{A}{N_A X_0}, \tag{3.5}$$

where N_A is Avogadro's number and A is the atomic weight. This implies that the mean free path of high energy photons before creating an electron-positron pair, equals $\frac{9}{7} X_0$ [47]

Interactions of Hadrons

The discussion of interactions of hadrons with matter has to be done separately for neutral and electrically charged particles. In general, the most probable energy loss of charged hadrons is governed by the Bethe-Bloch equation Section 3.1 similar to muons. Consequently, if they are in the correct momentum range, they can also be considered as minimum ionizing particles with similar signatures in the detector. Due to their mass,

the energy loss to bremsstrahlung is minimal since the radiated power scales with m^{-6} and the lightest charged hadrons, the pions, are 278 times heavier than electrons. This prevents the formation of a typical electromagnetic shower as explained in Section 3.1.1. Compared to mesons, hadrons have a much higher cross section for *Hard Interactions* with the atomic nuclei or individual nucleons of the surrounding medium due to their composite nature and participation in the strong force. The variety of possible hadronic processes leads to large fluctuations of the signature of a hadronic event in the detector. Depending on the momentum transfer of the reaction, the struck nucleus either receives only a small fraction of the hadrons momentum or is disintegrated by inelastic scattering. These strong inelastic interactions typically change the nature of the primary hadron and produce a number of secondary particles, typically nucleons from the struck nucleus, additional charged or neutral mesons like pions or kaons as well as leptons and photons. Additional lower energy nuclear reactions within the remnants of the struck nucleus, like evaporation of neutrons by intra-nuclear cascades [49] and de-excitation by emission of photons lead to the creation of low energy particles. Since neutral hadrons cannot ionize the medium, the only way of loosing energy are nuclear interactions. The most prominent neutral particles concerning calorimetry are neutrons which play a special role in the development of hadronic calorimeters discussed later. The mean free path before an inelastic interaction occurs is called *nuclear interaction length* λ_I and is estimated by [46]

$$\lambda_I \approx 35 \frac{\mathrm{g}}{\mathrm{cm}^2} A^{1/3}. \tag{3.6}$$

Here, A is the atomic mass number. This relates to a path length by weighting it with the density of the traversed medium.

For the commonly used detector materials the X_0 is much shorter than λ_I. In Iron, for example, $X_0 = 1.757\,\mathrm{cm}$ [45] wile $\lambda_\mathrm{I} = 16.77\,\mathrm{cm}$ [45]. Consequently, the material needed to contain electrons, positrons or photons in the detector is much lower than for hadrons of comparable energy. This drives the design of electromagnetic and hadronic calorimeters and will be further discussed in Section 3.3.

3.1.1 The Electromagnetic Shower

Electrons, Positrons and Photons of sufficient energy develop electromagnetic showers in matter because of the reactions transforming them into each other. As explained above, a photon with kinetic energy of $10\,\mathrm{MeV}$ or higher looses energy by creating electrons and positrons, which in turn loose their energy by radiating photons. Since a single high energy electron can radiate a large number of photons a significant particle multiplication occurs, leading to the development of a shower (Figure 3.4). As the shower develops the average energy per particle decreases until the pair-creation of electrons and positions stops. The remaining particles loose their energy by lower energy processes like compton scattering and ionization and the shower fades. Since the angle at which the electrons and photons are emitted scales with $m_e c^2/E$ [46], the core of the shower evolves along the direction of the incident particle. The length of the electromagnetic shower is proportional
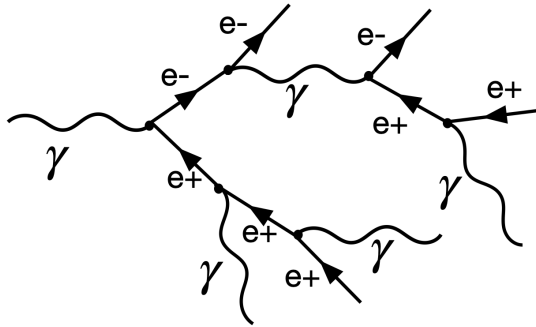
Figure 3.4: The start of an electromagnetic shower. The photons create electron-positron pairs which in turn radiate photons, leading to the development of a cascade.

to the logarithm of the incident energy [47]. Thus, if the material properties (X_0) are constant, it needs relatively little extra material to contain electromagnetic showers of higher energy. For example, it takes 25 X_0 of lead to contain a 10 GeV electromagnetic shower, whereas only an additional 1.3 X_0 is needed to contain 20 GeV [47].

In reality, the shower does not stop immediately after the critical energy is reached, but it continues well beyond the point at which the amount of particles is maximized. Processes like compton scattering and ionization can also produce secondary particles, leading to a slow decay of the shower after the maximum. More accurate shower models are available from Monte Carlo simulations (for example in [46]), but will not be elaborated further. The transverse shower development is described by the *Moliere Radius* ρ_M, given by [47]

$$\rho_M = \frac{X_0}{\epsilon_c} m_e \sqrt{\frac{4\pi}{\alpha}} = \frac{X_0}{E_c} 21.2 \text{MeV}, \tag{3.7}$$

with m_e=511 keV, the rest mass of the electron, and α the fine structure constant. This material specific quantity relates the radiation length and the critical energy to the radius of a cylinder containing on average 90% of the deposited energy [47].

3.1.2 The Hadronic Shower

The hadronic shower differs significantly from the electromagnetic one due to their governing mechanism, the *strong force*. While the particle multiplicity in an electromagnetic shower is driven by bremsstrahlung and pair creation, the number of possible interactions is much larger for hadrons. Additionally, a fraction of the energy is fundamentally *invisible* because it is consumed to break up the nuclear binding by spallation. A part of it is also carried away by neutrons leaving the detector. The typical length scale of a hadronic shower is governed by the nuclear interaction length λ_I. In most absorbers λ_I is much larger than X_0[1] and hadronic cascades usually evolve on larger scales than

---

[1]For lead: X_0=0.53 cm, λ_I=17.59 cm
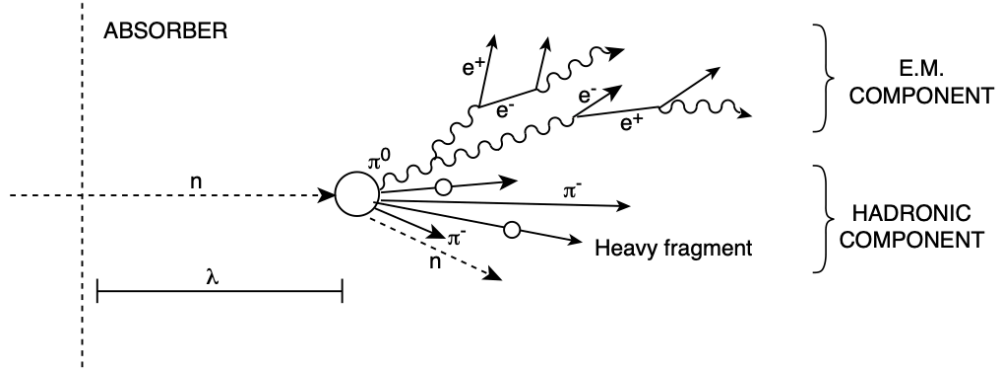
Figure 3.5: Schematic of the hadronic shower development. The primary hadron undergoes a strong interaction with the nucleus of the traversed medium. Among the produced secondary particles are charged and neutral baryons and mesons which can subsequently undergo additional interactions and increase the particle multiplicity. Neutral pions play special role because of their primary decay mode into two gamma photons. The gamma photons induce an electromagnetic sub-shower within the hadronic shower. Taken from [50].

electromagnetic showers and require larger detectors to achieve containment. On average 1/3 of the secondary particles are highly energetic neutral pions. With a branching ratio of 98.8% these pions instantly decay into two photons, leading to electromagnetic sub-showers within the larger hadronic shower. The fraction of total energy of the hadronic shower contained these sub-showers is on average given by

$$f_{em} = 1 - \left(\frac{E}{E_0} \right)^{(k-1)}. \tag{3.8}$$

Here, E_0 denotes the average energy for the production of one pion, k is related to the average number of produced pions per interaction and E is the energy of the primary hadron. This electromagnetic contamination deteriorates the energy resolution of hadronic calorimeters, because they are not optimized to detect electromagnetic showers. The spallation reactions induced by highly energetic hadrons also induces the evaporation of slow neutrons by the remaining nuclear remnants. Their energy follows a Maxwell-Boltzmann distribution and is typically of the the order of 1 MeV [47]. Together with the highly energetic neutrons produced instantly by the spallation reaction they contribute significantly to the invisible energy because their interaction with the medium is purely based on the strong interaction and is highly material dependent. Up to an energy of 1 GeV the most probable interaction is elastic scattering, followed by inelastic interactions. After loosing their kinetic energy the neutrons are captured by a nucleus which radiates the gained energy by emitting gamma photons. Since the speed of these neutrons is low, the processes happen at later times up to several microsecond after the initial inelastic hadronic interaction and the shower start.

3.1.3 Energy Deposition of Charged Particles in Thin Layers

A special role in the development and response of calorimeters play the characteristics of energy deposition of charged particles in thin layers. Detectors like sampling calorimeters or silicon tracking detectors usually consist of individual active components with a low thickness of tens of micrometers to several millimeters. Since this restricts the number of individual interactions the spectrum of the energy deposition does not follow a naive Gaussian model but is sensitive to fluctuations. The spectrum was first described by Landau [51] and is characterized by a long tail towards higher energies caused by occasional high-energy collisions with electrons of the surrounding medium.

This tail drives the mean energy loss, as it is described by Bethe-Bloch, away from the most probable energy loss, therefore it is a common practice in detector development to use the mode of this distribution to quantify the energy deposition in a single active element. Furthermore, the most probable value of the distribution is only weakly correlated to the energy of the traversing particle. This property makes it a suitable quantity to calibrate the detector with minimum ionizing particles like muons, that penetrate the full detector volume without causing significant amounts of secondary particles.

3.2 Scintillation and Photon Counting as Means of Signal Extraction

The calorimeters and detector concepts discussed in this thesis use scintillating material to extract the signal. A scintillator converts a fraction of the energy deposited by ionizing radiation to visible light These photons are collected and detected by dedicated counters. The number of emitted photons is proportional to the energy transfer to the scintillator which in turn enables the final detector to measure energies of incoming particles. Besides crystalline and liquid scintillators, polymer based ones are especially interesting because of their simple handling and relatively low price. Since the polymers, for example polyvinyl toluene or polystyrene, reabsorb a fraction of the emitted light, flours are added to modify the emission characteristic as shown in Figure 3.6.

In addition to the wavelength shift, the flours are also coupling to the polymer by dipole-dipole interactions (Forster transfer). These happen on a much shorter time scale and increase the prompt light emission and consequently the intrinsic time resolution of the compound [45].

A convenient photon counter is the *Silicon PhotoMultiplier (SiPM)* [52], a matrix of individual silicon-based *Avalanche Photo Diodes (APDs)*. The SiPMs used in calorimetry typically feature thousands of APDs on an area of about $1\,\mathrm{mm}^2$. They are coupled to the scintillator to count the number of photons impinging on them and generate a measurable electrical signal. The area of this signal is proportional to the number of detected photons and encodes the deposited energy in the polymer. The compactness and low power consumption of the SiPMs offer a convenient possibility to integrate them into the active area of the calorimeter without introducing massive amounts of uninstrumented material.
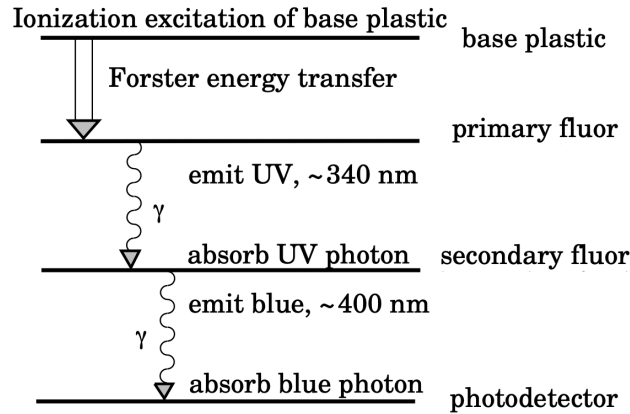
Figure 3.6: Light emission in polymer based scintillators. The energy transferred to the base plastic is transferred to the primary flour by Forster energy transfer. This transfer occurs on a smaller time scale then the emission of the primary polymer. The second flour shifts the wavelength out of the absorption band of the base plastic. Taken from [45].

This concept will be explained further within the scope of the CALICE Analog Hadronic Calorimeter in Chapter 4.

3.3 Sampling Calorimeters and their Response to Particles

In general, calorimeters can determine a particles energy by measuring the energy deposited in side the active detector volume. Different approaches to the mechanical structure of a calorimeter exist. Homogeneous ones feature a fully active detector and the total detector volume is able to transfer the deposited energy into a measurable signal. Commonly used materials are scintillating inorganic crystals like thallium-dopes sodium iodide (NaI(Tl)) or lutetium–yttrium oxyorthosilicate (LYSO), depending on the usecase. The advantage of those crystals is their high density compared to organic or polymer-based scintillators, allowing for compact detector designs because of short radiation and nuclear interaction length to achieve containment. They are, however, expensive to manufacture. An inhomogeneous sampling calorimeter utilizes layers of dense passive material interleaved with an active medium for signal generation. These active areas are usually made of semi-conductor or low-density plastic scintillators. Since a large part of the incident particle's energy is deposited in the passive area, called absorber, this kind of calorimeter transforms only a fraction of the deposited energy into a signal. The absorber is usually made of heavy elements like tungsten, lead or iron (Steel) with short radiation length or nuclear interaction length. Impinging particles are gradually stopped and eventually form particle showers. Since a particle shower distributes the energy of one single primary particle across many secondaries of lower energy, it is much easier to contain the total energy within the detector volume. By

detecting the scintillation light in the active layers with photon counters like SiPMs, an electrical signal proportional to the energy of the primary particle is generated. The conversion factor from visible to total deposited energy, the so called *sampling fraction*, is defined as the energy deposition of a (MIP) in the active layers (E_{active}^{MIP}) relative to the total energy deposited in the calorimeter ($E_{active}^{MIP} + E_{absorber}^{MIP}$):

$$f_{sampling} = \frac{E_{active}^{MIP}}{E_{active}^{MIP} + E_{absorber}^{MIP}}. \tag{3.9}$$

Since $E_{absorber}^{MIP}$ is not measurable in a real calorimeter the absorber deposition has to be estimated by comparing the signals of MIPs (e.g. muons) of different energies (described in [47]). The sampling fraction is not to be confused with the response to particle showers, because their low energetic constituents deposit a much larger fraction of their energy in the absorber structure. The relative response of electrons (photons) and MIPs (e/mip) is in reality always smaller than 1. However, to some extent this value can be tuned by adjusting the *sampling frequency*, another characteristic quantity in calorimeter design. The sampling frequency increases by thinning down the absorber layers while keeping the total thickness of the calorimeter constant and increasing the layer count. On a microscopic level this increases the total area of the boundary layer between absorber and active medium, so a larger fraction of particles escapes the uninstrumented material and is detected.

Response to Hadrons

Sampling calorimeters are also used to detect hadrons, but in contrast to electrons (photons) the different interactions explained in Section 3.1 lead to a very different response of the detector. A charged pion at an energy below $1\,\mathrm{GeV}$ behaves like a MIP and probably looses its energy by ionization without considerable particle multiplication. Increasing the the energy also increases the chance of spallation reactions eventually developing a hadronic shower (Section 3.1.2). Among other particles, these reactions produce highly energetic secondary pions with a multiplicity that fluctuates on an event by event basis depending on the specific kinematics of the process. About one third of these pions are neutral [47] and lead to the development of an electromagnetic sub-shower. The energy density of these usually compact showers is much higher compared to the larger surrounding hadronic shower, due the usually short radiation length of the absorber structure Section 3.1. The sub-showers have a much higher chance to be contained in a finite detector volume. On the contrary, highly energetic secondaries like charged mesons and neutrons have a higher chance to penetrate the detector with very low energy deposition, increasing the amount of undetected energy. Therefore, a large electromagnetic fraction increases the amount of visible energy but the stochastic nature of this processes also increases the intrinsic event by event fluctuations.

Energy Resolution

Due to the fact that a sampling calorimeter is not active throughout the detector volume and the energy deposition in the calorimeter is only measured at specific layers, the energy resolution is influenced by the accuracy of this sampling. The total signal of the calorimeter is composed of the energy deposition of individual charged particles in the showers. With this respect it can be viewed as a simple particle counting experiment and is governed by poissons statistics. The energy resolution at a certain energy is defined by the standard deviation of the reconstructed energy divided by the true energy of the particle (σ/E). Assuming that at a given energy E, about 100 particles contribute to the signal, the standard deviation is $1/\sqrt{100} = 10\%$ and therefore, neglecting other sources of fluctuation, the resolution is also expected to be 10% at this energy. This implies that an increase in sampling fraction results in a reduced resolution from sampling fluctuations, since the amount of particles contributing to the signal is increased. In a linearly responding calorimeter the average number of shower particles scales with the particle energy so the relative energy resolution can be parameterized by [47]

$$\frac{\sigma}{E} = \frac{A}{\sqrt{E}} = \frac{10\%}{\sqrt{E}}. \tag{3.10}$$

This shows that the relative resolution decreases for increasing particle energy since the sampling fluctuations only increase with $\sqrt{E}$. In real applications additional sources of fluctuations contribute to the energy resolution. Effects caused by electronic noise are independent of the particle energy and contribute with a given value to the standard deviation of the reconstructed energy. The contribution of non-containment (leakage) of particle showers to the resolution increases linearly with rising particle energy.

Due to their compactness and low cost compared to alternative systems like homogeneous calorimeters or detectors using scintillating crystals as active medium, sampling calorimeters based on plastic scintillators with SiPM readout are promising concepts for future applications. Especially for hadronic calorimeters which typically require large mounts of dense material to contain highly energetic hadronic showers, a sampling calorimeter with metal absorbers is the most economic choice. Since the channel count in a highly granular calorimeter is intrinsically high, this option is unfeasible for homogeneous calorimeters. To reach unambiguous single channel imaging capability each individual cell has to be equipped with some form of read out which introduces inhomogenities in the active medium. Furthermore, the only types of scintillators reaching a nuclear collision length and radiation length comparable to dense metal are scintillating crystals. Due to their high cost it is not feasible to equip the full volume of a complete hadronic calorimeter for a collider detector with scintillating crystals. The following sections introduce a prototype of a hadronic sampling calorimeter developed by the CALICE collaboration for application in future particle collider detectors.

Chapter 4

The Large CALICE Analog Hadronic Calorimeter Prototype

CALICE is an international collaboration dedicated to developing modern highly granular calorimeter systems for applications in future high energy particle physics experiments. Various sub-groups develop electromagnetic and hadronic calorimeters based on silicon [53], gaseous [54] or scintillator [55] readout. The large Analog Hadronic Calorimeter (AHCAL) prototype is a scintillator based hadronic sampling calorimeter (see Section 3.3). It is designed for high spatial granularity and integrated electronics to investigate the capabilities of such a system and to demonstrate the scalability to a full scale collider detector. This chapter introduces the design drivers, explains the readout scheme and calibration. Special emphasis is put on the time calibration which is a major part of this thesis.

4.1 Design Drivers and Implementation

In a particle flow [25] oriented detector system envisioned for future collider experiments, the task of the hadronic calorimeter is the precise energy reconstruction of neutral hadrons in particle jets. Since the majority of the constituents of a jet are charged hadrons, the system has to be capable of separating the individual particles and associate them with their respective signal in the detector. Usually this is done by extrapolating the tracks recorded by the tracking detectors to the front face of the calorimeter. To reduce the risk of wrong association the spatial resolution of the calorimeter has to be high enough to separate particles that enter the detector in close proximity. This so called *confusion* is an important performance metric especially for experiments with high luminosity and increased pile-up of events. Furthermore, the particle flow approach increases the energy resolution for hadronic jets [56], making these calorimeter systems especially useful for precision measurements on processes with multiple hadronic final states e.g. involving a Higgs boson[1].

The AHCAL technological prototype is a system designed for applications in such future collider experiments. It is built as an imaging calorimeter using highly segmented active

---

[1]The standard model Higgs boson primarily decays into particles that form hadronic jets, either by direct decay into a pair of quarks or gluons or via the production of W and Z bosons. The majority of these bosons decay into a quark pair which will form hadronic jets.

Figure 4.1: Fully assembled AHCAL technological prototype. The active layers, identified by the visible interfaces, are placed between the stainless steel absorber structure. In total the prototype consists of 39 layers.

layers based on plastic scintillators to provide single channel energy and time measurement while keeping a sufficient 3-dimensional position resolution for particle flow reconstruction. Preceded by the *physics prototype* [5] built to establish the concept of highly granular calorimeters and to develop capable reconstruction algorithms to exploit the detector's capabilities [25], the technological prototype will demonstrate the scalability of the design and study the integration into a full scale collider detector. Figure 4.1 shows the assembled AHCAL stack consisting of 39 layers of non-magnetic steel absorber plates with a total depth of about 4λ. The active layers placed between the steel feature 576 individual plastic scintillator tiles with a spatial granularity of $30 \times 30 \, \text{mm}^2$, wrapped in reflective foil and read out by silicon photomultipliers (SiPMs). Each SiPM is directly mounted to a Printed Circuit Board (PCB), the *HCAL Base Unit (HBU)*, containing a total of 4 SPIROC2E chips [57] for read out and digitization. These Application Specific Integrated Circuits (ASIC) are customized to the purpose of reading out SiPM signals and operate within the detector volume. The total front-face area of the detector amounts to $72 \times 72 \, \text{cm}^2$, equivalent to 4 HBUs. The next sections provide information on the signal extraction, digitization and calibration procedures necessary to understand the results explained in Chapter 5.
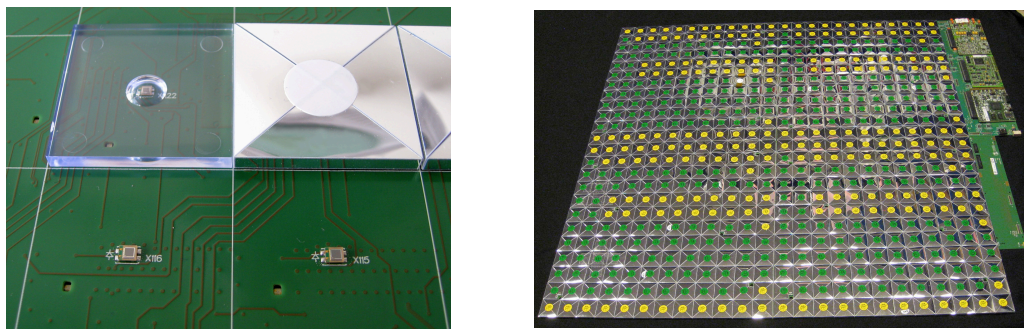
Figure 4.2: Left: Individual channels of the calorimeter. Shown are unequipped channels with the bare SiPM placed in the center, as well as an unwrapped tile to illustrate the placement of the scintillator and a wrapped tile. Right: Fully assembled active layer of the AHCAL with interface and power boards.

The SiPM-On-Tile Technology

To achieve competitive energy and time measurement compared to silicon or crystal based calorimeters, while keeping material and production costs under control, plastic scintillators provide a viable solution. In the past, the scintillation light was guided out of the active detector volume and picked up by photomultiplier tubes of several centimeters in size. This introduces long signal paths, increases light loss and affects time and energy resolution. The availability and sinking costs of small scale SiPMs with sizes around $1\,mm^2$ offered the possibility to integrate the light sensor and read out electronics into the detector, allowing compact designs with minimal introduction of dead material. The first application of the *SiPM-on-Tile* technology in large scale calorimeter prototypes was demonstrated by the CALICE collaboration and got optimized further [58] [59] until construction of the AHCAL. The left image in Figure 4.2 shows a partially equipped HBU with the SiPMs directly soldered to it, as well as two $30{\times}30{\times}3\,mm^3$ scintillators. The unwrapped tile illustrates the combination of active medium and photon detection in a compact way by housing the SiPM (Hamamatsu MPPC S13360-1325PE) in a dome shaped cavity (dimple) to enhance light collection. The tiles are wrapped in reflective foil to reduce light loss and are glued directly to the PCB. The right image in Figure 4.2 shows a fully equipped active layer of the AHCAL prototype, including interface, control and power supply boards. The analog signals from the SiPMs are digitized by the ASICs mounted on the opposite side of the HBU and get sent to a data aggregator, minimizing the analog signal path of the system ensuring undistorted signals and minimal loss of information.

The total thickness of an active layer is around $7\,mm$ including the reflective foil, scintillator, PCB and ASIC. The tiles are automatically wrapped and placed on the HBU to demonstrate scalable mass production techniques required for the construction of a full size collider detector.

The SPIROC2E Front-End Chip

The integration of the front-end electronics into the detector volume requires a slim package that contains the trigger logic, amplifiers, buffer memory and digitizers. The *SiPM Integrated Read Out Chip* (SPIROC) [57] (Version 2E) is a dedicated ASIC for handling signals from SiPMs and is specifically designed around the requirements of the AHCAL. It can read up to 36 channels and has an onboard analog memory store up to 16 events within one read out cycle. To eliminate the need of active cooling, therefore reducing the complexity and amount of dead material, the chip is operated in *power-pulsing* mode synchronized to the collision timing in a linear collider. One cycle of the ILC, for example, consists of 1 ms of bunch crossings followed by 199 ms of down time needed to prepare the next bunch trains in the pre-accelerators. This results in a duty cycle of 0.5% in which the chip has to be ready to record the SiPM signals and store them in the onboard analog memory. In between the collisions the buffered signals are digitized and sent to the eternal storage via a data aggregator. By powering the analog part of the ASIC only during collisions and the digital part only during the accelerator down time, the power consumption is drastically reduced to reach the design goal of 25 µW per channel [60]. This chip also provides dual-gain energy measurement to increase the dynamic range of the system and reduce signal clipping, as well as single-cell time stamping with a foreseen resolution below 1 ns. During one read out cycle the detector can take data until the analog buffer of one chip is filled, whereupon it sends a busy signal to the Clock and Control Card (CCC) which distributes a "stop acquisition" signal to the remaining chips and initiates the digitization and read out. If the buffers are not filled within a predefined time, the acquisition is stopped manually by the CCC.

Energy Measurement on the SPIROC2E

A sketch of the electronics of one channel on the SPIROC is shown in Figure 4.3. Upon the arrival of an external trigger, the signal of the SiPM connected to "IN" is amplified by the low and high gain amplifier. The high gain signal is shaped and compared to a predefined trigger threshold to decide if the signal level is high enough to be stored in the analog memory. For the energy measurement, both low and high gain signals are connected to a memory cell which consists of a capacitor to store the charge delivered by the slow shapers. The data taking is subdivided into time steps called *Bunch crossing IDs (BxID)*, a term that refers to the crossing of the particle bunches at the interaction point of the collider. It is an increasing counter important to associate the readings of the individual channels to an event. This counter is also responsible for the switching of the memory cells and ensures that only one cell per BxID is filled without overwriting data from previous BxIDs. If the acquisition is stopped, the memory cells are one-by-one connected to a gain selector switch to decide which cell is connected to the 12-bit Wilkinson Analog-to-Digital (ADC) converter. The gain switching ensures that the signals do not exceed the dynamic range of the ADC. After digitization the signals are stored in an onboard digital memory until the data concentrator is ready to read the data packets. After all events are sent out, the memory is reset and a new readout cycle
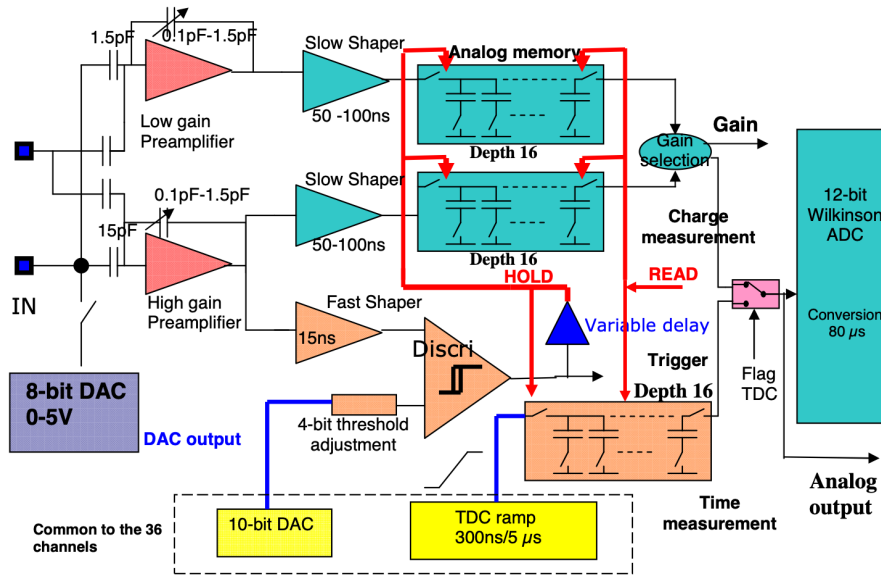
Figure 4.3: Sketch of the analog part of one channel on SPIROC2E. The SiPM is connected to the input named "IN". Taken from [61].

starts.

In the reconstruction the energy in units of ADC is converted to the MIP scale. Therefore, the ADC spectrum of hits produced by minimum ionizing muons is obtained per channel and the most probable value is extracted. This value is used to convert the hit energy from ADC to MIP. The advantage of this approach is the well defined energy deposition of MIPs according to the Bethe-Bloch formula (see Section 3.1). Since these particles penetrate the detector, an equal amount of events can be collected throughout the full volume to extract this calibration value for all channels. The detailed process of energy calibration includes a number of additional steps not covered in this thesis. Details are explained in [62]. The time measurement will be explained in greater detail in the next section since it is vital to the analysis described in Chapter 5.

4.2 Time Measurement on the SPIROC2E

The main clock frequency of 4 MHz of the SPIROC2E is not fast enough to reach a time resolution on the sub-nanosecond level. The implementation of a faster main clock would result in an increased power consumption and heat dissipation which will ultimately increase the complexity and cost of the calorimeter system. The *Time-to-Digital Converter (TDC)* implemented on the chip is a so called "ramp-interpolator" using an analog voltage ramp of constant slope to transform the time measurement into a voltage measurement done with the same 12-bit Wilkinson ADC used for the energy measurement. As explained in Section 4.1 the read out cycles are subdivided into individual BxIDs that are uniquely associated to an event number. During a BxID the

35
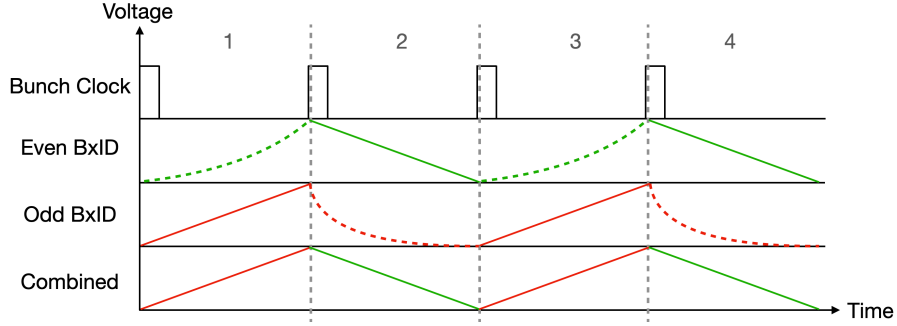
Figure 4.4: Sketch of the TDC ramps. Alternating slopes are implemented and switched for even and odd BxID parities. The dashed lines only illustrate the recovery of the ramp to its initial state and do not represent the actual voltage levels.

voltage of the TDC ramp is linearly increased. As sketched in Figure 4.4, two individual slopes with opposing sign are implemented for even and odd bunch crossing parities, in order to reduce unwanted oscillations associated to fast voltage switching that might potentially distort the time measurement at the beginning of each BxID. In this scheme, one ramp can recover its initial state while the other one is in use.

As soon as the external trigger arrives and the discriminator connected to the high gain signal line (see Figure 4.3) enables the data taking, the current voltage of the ramp is stored in one of 16 analog memory cells. This implies that any point in time, within one BxID, is associated to a voltage reading and is always defined relative to the start of the BxID. After the acquisition is stopped the stored voltages are digitized and sent via the data aggregator to the DAQ computer.

Theoretical Time Resolution

The ASIC can operate in two modes that depend on the speed of the bunch clock and determine the duration of one BxID. The default bunch clock frequency is 5 MHz (ILC mode) which results in a BxID length of 200 ns and is designed to match the bunch spacing at ILC. Since these detectors get tested and calibrated at beam test facilities that usually do not provide particles at this rate, a slow bunch clock is implemented at 250 kHz (Test beam mode) to prolong the duration to 4 µs and to reduce the amount of empty bunch crossings. A faster bunch clock also increases the slope of the voltage ramp and therefore increases the theoretical time resolution. Assuming that the voltage range of the ramp is the same for every clock speed, the time binning achievable with the 12-bit ADC is $\frac{4000\text{ns}}{4096}$ =0.977 ns for test beam mode and $\frac{200\text{ns}}{4096}$ =0.048 ns for ILC mode. Since the ramp voltages are not exactly the same on every chip and also the analog memory cells introduce additional distortions due to manufacturing tolerances, a time calibration has to be performed against the external trigger reference in order to extract a realistic time resolution of the system.
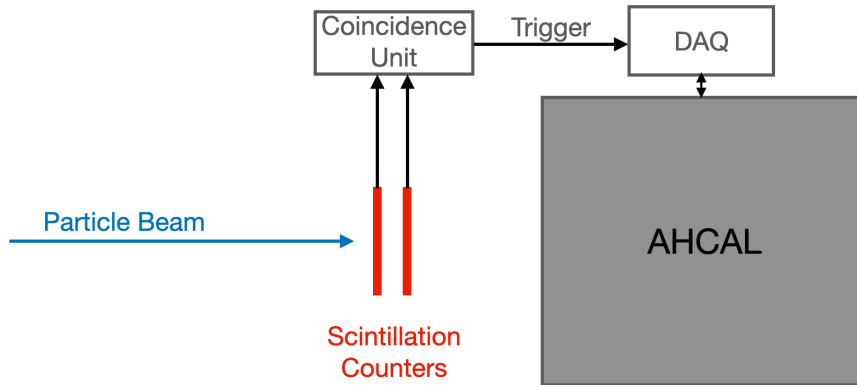
Figure 4.5: Simplified sketch of the beam test setup. The scintillation counters shown in red are wired to a coincidence unit that generates a trigger signal for the AHCAL upon the passage of a beam particle.

4.3 Time Calibration

The data packets received from the DAQ [63] of the AHCAL encode the hit time in ADC readings relative to the start of the bunch crossing and have to be calibrated to nanoseconds against an external trigger. This procedure was first used in [64] and is extended in the frame of this thesis. In a test beam scenario this trigger signal is usually generated by two scintillation counters placed in front of the calorimeter as shown in Figure 4.5. As soon as a particle creates a signal in both counters, the coincidence unit they are connected to issues a trigger signal to the DAQ system of the AHCAL. The timestamp of this trigger is associated to the current BxID so that the energy depositions in the AHCAL can be associated to a trigger time. Later in the event building step, only energy depositions within one read out cycle and a valid trigger will be stored as validated events. It is important to note that the time stamping accuracy of the Beam InterFace (BIF), which is responsible for the trigger validation of the recorded events, is at the order of 1 ns.

4.3.1 Extraction of the TDC Ramp

The general principle of the time calibration is the reconstruction of the TDC ramp in terms of ns/TDC. Since this has to be done separately for every chip, channel, memory cell and BxID, the hits in the detector are sorted into these categories. For every combination, the BIF trigger time has to be related to the TDC readings of the hits as shown in Figure 4.6. By fitting a linear function to the data the parameters of the TDC ramp can be extracted. Because there is only one circuit per chip that generates the voltage ramp for all channels, the slope parameters for even and odd BxIDs are the same for every
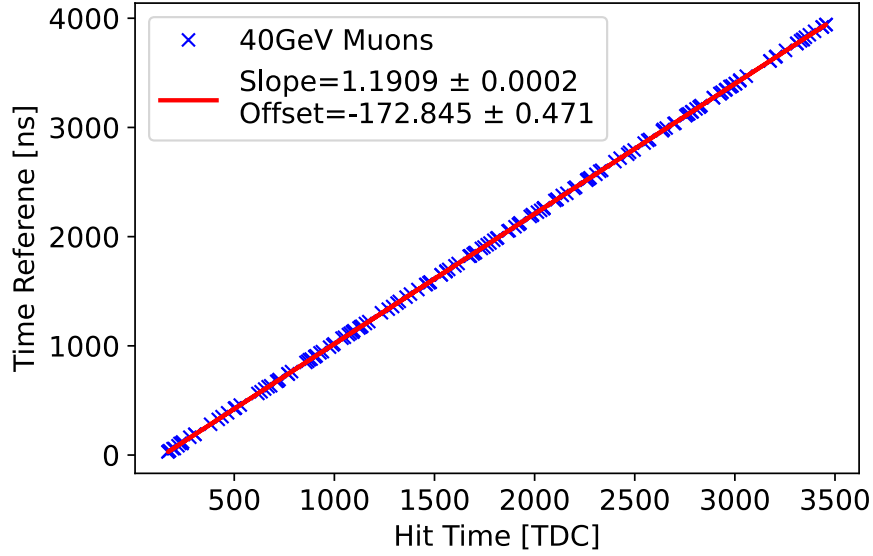
Figure 4.6: This plot shows the linear relationship between the reference time provided by the BIF and the hit time in terms of TDC ticks measured by the ASIC. The linear fit is used in the calibration to translate the hit time from TDC to nanoseconds.

channel on a chip. The offset however, has to be extracted individually for every channel and analog memory cell to account for differences in signal paths and tolerances of the analog electronics on the chip. For the full prototype equipped with 39 layers and 16 ASICs per layer, this results in a total of 720096 calibration constants. The formula to reconstruct the hit time in nanoseconds from the TDC reading of the ASIC reads:

$$t_{\text{Hit}}[\text{ns}] = \text{Slope}[\frac{\text{ns}}{\text{TDC}}] \cdot t_{\text{Hit}}[\text{TDC}] + \text{Offset}[\text{ns}] - T_{\text{Reference}}[\text{ns}]. \tag{4.1}$$

To obtain a full calibration of the setup a data set covering the full detector volume has to be collected with a sufficient amount of hits per channel and memory cell to perform the linear fit. Additionally, the events should have one hit per layer to keep the occupancy per chip minimal and should extend through the full volume to obtain the same amount of statistics per layer. The best suited particles for this task are muons close to minimum ionization (see Section 3.1) because the vast majority traverses the detector without causing particle showers. Due to this procedure, the reconstructed hit times of a muon traversing the detector are distributed around zero because they are always calibrated relative to the arrival of the external trigger. In fact, the time of all quasi instantaneous processed like the formation of electromagnetic showers or inelastic hadron interactions, that happen on the same timescale as a muon traversing the detector, will be distributed around zero. Slower processes like elastic scattering of neutrons and nuclear processes will be delayed.

The following section introduces the data set collected at beam test campaigns in 2018

at CERN and 2019 at DESY and evaluates the calibration based on the spread of the constants and the number of successful calibrations.

4.3.2 Calibration Data Set - May and June 2018

The fully assembled AHCAL prototype has undergone a first extensive test program at the SPS test beam facility at CERN in 2018. In the course two campaigns in May and June large data sets to calibrate the energy and time of the detector were taken. The detector was placed on a remote controlled movable stage to scan the full volume with a muon beam and collected a total valid event count of ~ 32000000 in May and ~ 6000000 in June. All of the events are taken with the slow bunch clock and bunch crossing length of $4\,\mu s$. An additional event selection discards all the events that have a trigger time within $500\,ns$ around the change of the BxID to reduce the risk of picking up distortions of the hit time from the switching of the TDC ramps. After sorting the hit according to chip, channel, memory cell and BxID, the linear fit is performed. For each combination, hit numbers between 20 and 200 are required to gain sufficient accuracy while keeping the memory and time consumption under control.

4.3.3 Calibration Data Set- August 2019

Another dedicated beam test campaign was launched in August 2019 at DESY to test the AHCAL hardware in ILC mode. To suppress the formation of electromagnetic showers from the electron beam and to keep the occupancy of the ASICs low, the majority of data was taken with 5 active layers without absorbers. The performance of the detector in ILC mode will be reported in Section 5.3.

4.4 Correction of Time Shifts

During the first reconstruction of the TDC data from SPIROC2E in the May beam test campaign, an unexpected shift of hit times was observed. The histogram in figure Figure 4.7 shows the reconstructed hit times of muons after the calibration procedure explained before. In addition to the expected central peak two accumulations of hit times around $\pm 28\,ns$ are observed. Thorough investigation has shown that these are not correlated to any physical processes in the detector but caused by the read out. More specifically, it depends on the state of the detector before the acquisition (read out cycle) is stopped and the data is digitized and moved from the ASIC to the DAQ computer.
To understand this behavior one has to look at the hierarchy of the relevant DAQ elements shown in Figure 4.8.
The stopping of the acquisition is triggered by two different conditions. In the unproblematic scenario, the Detector InterFace (DIF) issues the stop signal after a predefined time out is reached. This signals propagate to the individual ASICs which stop the acquisition simultaneously and initiate the digitization. The data is transferred via the DAQ chain and sent to the computer via the Link Data Aggregator (LDA).
The second possible scenario occurs if one of the ASICs filled its analog buffer within
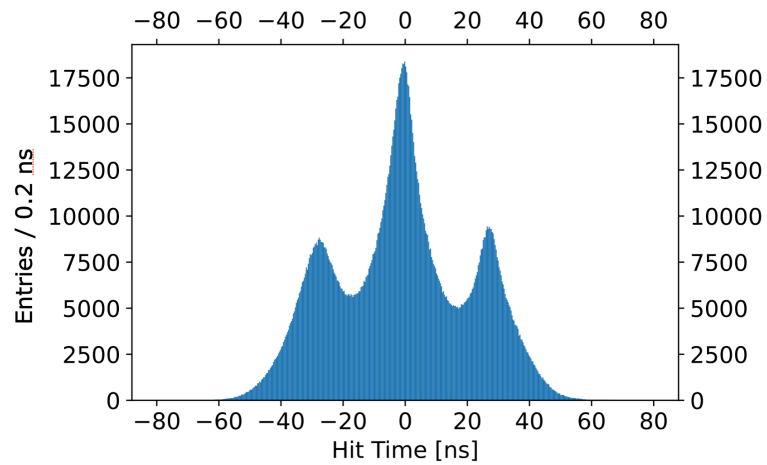
Figure 4.7: Hit time distribution of a muon data set with visible shifts. An additional calibration step is implemented to correct the unwanted secondary peaks around $\pm\,28\,$ns.
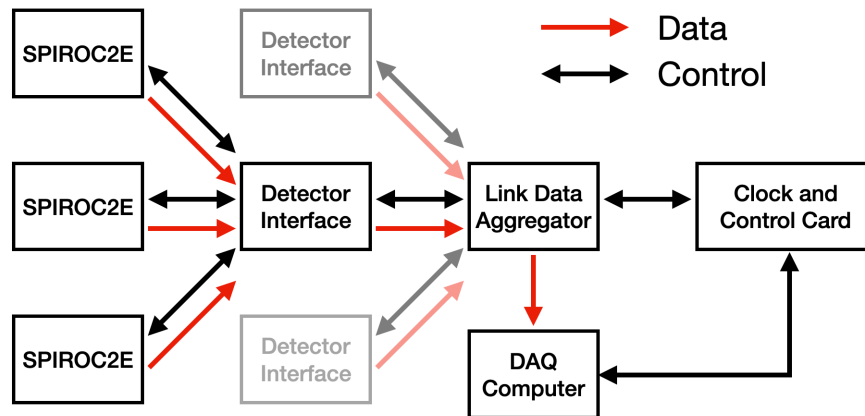
Figure 4.8: Sketch of the relevant parts of the DAQ chain of the AHCAL. The red arrows show the flow of data from the individual channels on the SPIROC2Es to the DAQ computer for storage. The shadowed parts illustrate additional parts that are not shown for simplicity. The control commands are propagated to the chips from the Clock and Control Card through all the DAQ modules.

one channel and cannot take further data. This chip issues a *busy* control signal that propagates to the CCC and is distributed to all the other chips in the detector. During this propagation delay, data is still taken by these chips. Since the read out cycles in the AHCAL are subdivided into BxIDs the issuing of the busy signal does not necessarily occur in the same BxID in which all the other chips stop taking data. The time shifts are connected to this mismatch and appear only in read out cycles that got terminated by a full chip. Since this conditions are only encoded in the raw data from the detector but did not get saved to the reconstructed data, the information was not accessible for calibration. An updated DAQ software was developed and the raw data got processed again, to include the relevant information on the termination of the read out cycle. If the last BxID parity in the read out cycle is odd, no shifts occur. If the parity is even, the hit time of the individual events within this cycle is shifted by $+27\,\text{ns}$ if the BxID parity of the respective event is even, or $-27\,\text{ns}$ if it is odd. Consequently, the calibration has to be sensitive to the stopping condition of the detector in order to correct for this behavior, hence the calibration explained in Section 4.3 has to be extended. In addition to the previously obtained offset parameters an additional offset ($\text{Offset}_{\text{BxID}}$) is used for the read out cycles affected by the shift. This offset is calculated individually for every memory cell, relative to the offset for memory cell 0 (Offset_0), which is extracted from non shifted data from read out cycles terminated by the timeout. Equation (4.1) is extended by this additional functionality and reads:

$$t_{\text{Hit}}[\text{ns}] = \text{Slope}[\frac{\text{ns}}{\text{TDC}}] \cdot t_{\text{Hit}}[\text{TDC}] + \text{Offset}_0[\text{ns}] + \text{Offset}_{\text{BxID}}[\text{ns}] - T_{\text{Reference}}[\text{ns}] \quad (4.2)$$

With this method, $\text{Offset}_{\text{BxID}}$ should exactly reflect the time shifts seen in Figure 4.7 making it easy to monitor the behavior of the detector. The Slope and Offset_0 parameters for the non shifted case are shown in Figure 4.9.
The slope parameters accumulate around $\pm\,1.2\,\text{ns}\,\text{TDC}^{-1}$, in agreement with the expectation of two equal absolute values with opposite signs. The offsets for the odd BxID follow a narrow distribution around $-145\,\text{ns}$ while the ones for even BxID are spread around $4425\,\text{ns}$. This larger spread originates from the implementation of the voltage ramp used for the time measurement, since the low voltage point of the digital-to-analog converter is defined with a higher accuracy than the end point of the ramp. In total, 93% of the channels passed the minimum required events in memory cell 0 (see Section 4.3) to successfully calculate the constants. The remaining ones are set to produce a hit time of $-999\,\text{ns}$ to identify them in the analysis. The $\text{Offset}_{\text{BxID}}$ values are obtained relative to Offset_0 for the shifted and not shifted read out cycles. Since one value is needed for every memory cell, only the mean values are shown in Figure 4.10, the error bars indicate the standard error of the mean.
For the non shifted set memory cell 0 has no additional value, since this is defined as Offset_0. From cell 2 on the constants for even BxID gradually decrease until cell 12 where they increase steeply. On the contrary, the constant for odd BxID increase steadily up to cell 15. Since the non-shifted case only includes read out cycles terminated by the timeout, cell 16 is never filled as explained above. As expected, the shift got picked up in
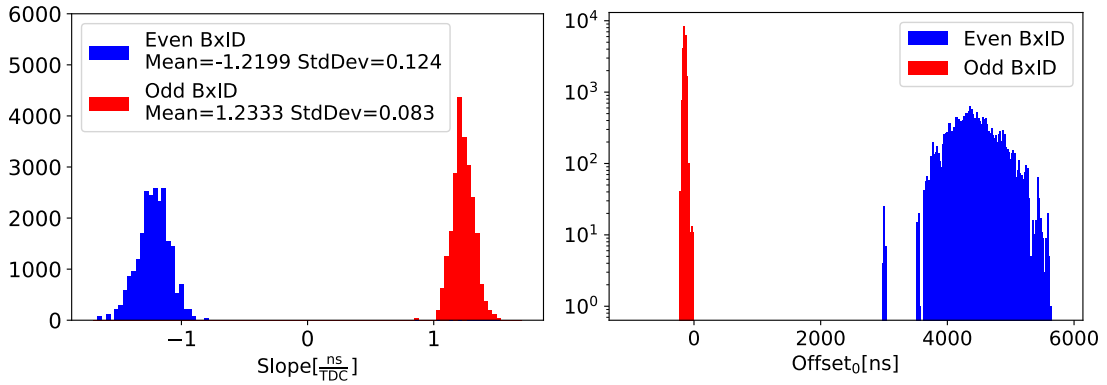
Figure 4.9: Left: Distribution of the slope parameters of the linear calibration fit for even and odd BxID. As expected, the values are distributed around the same absolute value with opposite sign. Right: Distribution of the offset parameters of the linear calibration fit for even and odd BxID. The larger spread of the blue distribution originates from the implementation of the voltage ramp used for the time measurement, since the low voltage point of the digital-to-analog converter is defined with a higher accuracy than the end point of the ramp.
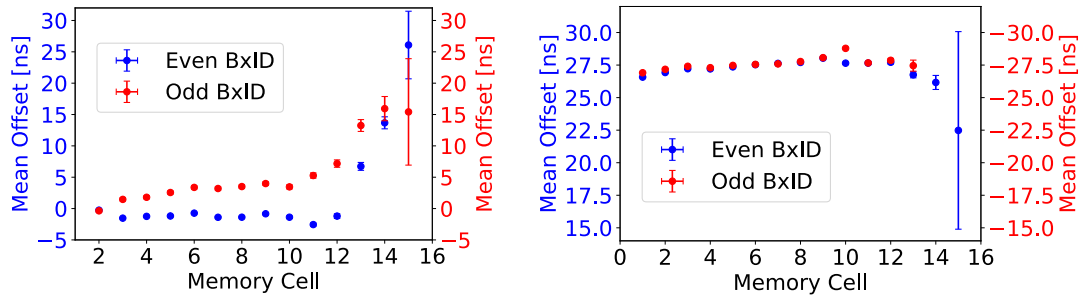
Figure 4.10: Mean values of $\text{Offset}_{\text{BxID}}$ for the different memory cells. On the left, the unshifted cases are shown and the values are distributed closer to zero, as expected. The right side shows the constants for the shifted case and a cleas accumulation of the valures around $\pm 27.5\,\text{ns}$ is visible. In both cases the missing points are caused by the sparse calibration data set in the higher memory cells, often not fulfilling the minimum statistics required for the calibration fit.
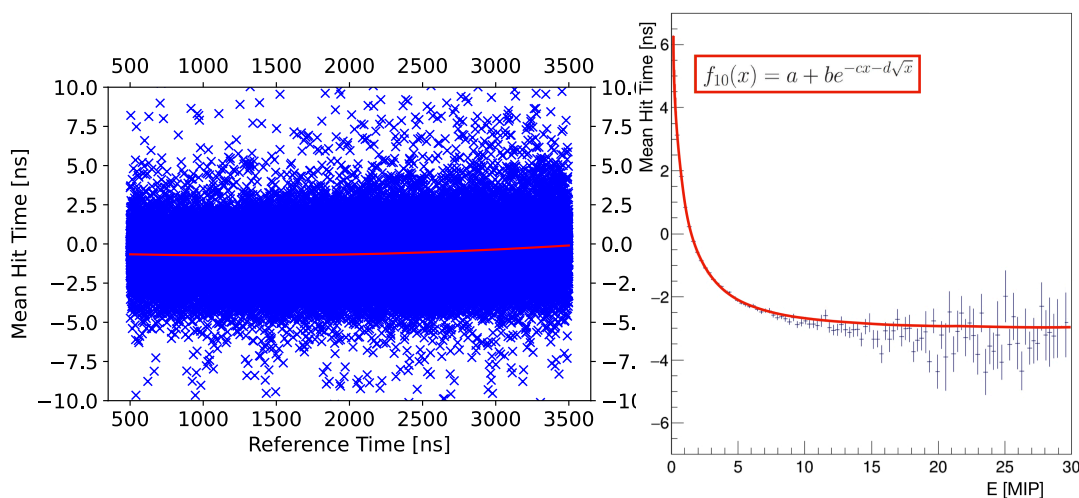
Figure 4.11: Left: Example of the correction of a slight non-linearity of the TDC ramp manifesting itself as a non-linear relation between reference and mean hit time. Right: Example of the correction of time walk. The modified exponential function showed the best performance in parameterizing the data points.

the calibration constants of the shifted data set at $\pm 28\,\mathrm{ns}$, showing comparable values for even and odd BxIDs, except memory cell 10 which is known to behave different also in the energy calibration [62]. After the correction of the shift, non-linearities in the response are corrected.

4.5 Correction of Non-Linearity and Time Walk

The voltage ramp in the TDC is in reality not necessarily a linear increase, due to imperfections in the electronics. To compensate this a correction in the form of a second order polynomial is applied. An example of this is shown Figure 4.11 on the left for the mean hit time of 100000 muon events.

There is a slight non linearity which manifests itself in an offset of $400\,\mathrm{ps}$ at the beginning of the BxID which vanishes towards later reference time. The overall linearity is improved compared to the previous detector setup equipped with the older SPIROC2B chips [64]. The right plot in Figure 4.11 shows an example of the time walk correction applied to the hit times, to correct for the fact that signals with a higher amplitude are expected to cross a constant threshold earlier than hits with a lower amplitude. An exponential function shown in the plot was found to fit the response of the AHCAL best. After calibration and corrections are applied, the hit time distribution of muon events is free of shits and centered at zero as shown in Figure 4.12.

Figure 4.12: Resulting muon hit time distribution after the corrections are applied. The distribution is centered at zero and the time shifts present in Figure 4.7 are corrected.

4.6 Correction of Chip Occupancy

The corrections obtained with the muon data set are also applied to electron and pion data. The difference is that these particles cause particle showers in the detector and the number of hits recorded by one chip per event can get large. It was found that this so-called occupancy impacts the time measurement of SPIROC2E. As shown in Fig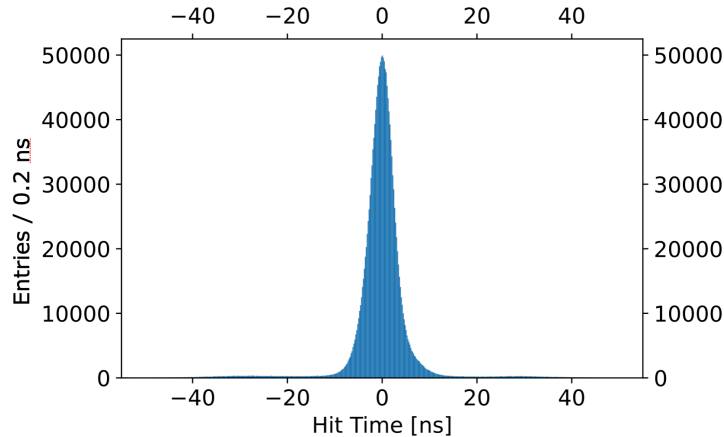ure 4.13 on the left, not only the mean hit time is shifted with rising chip occupancy but also the width of the distribution changes. For even BxIDs the time measurement is smeared to positive times, for odd BxID to negative times. While the mean hit time can be corrected by an additional calibration, the width of the distribution cannot be decreased because shifting individual hits would break the correlation of hit times within one event. Figure 4.13 shows an example of a 2nd order polynomial fit that is used to parameterize and correct the mean hit time.

For every channel one such fit is obtained for even and odd BxID for high and low gain signals which results in 4 calibration fits per channel. A comparison of the hit time distribution before and after the occupancy correction for a 40 GeV pion data set is shown in Figure 4.14. The corrected distribution shows increased uniformity and is centered at 0 ns, as expected. Most importantly the tails of the distribution are decreased. The remaining broadening of the corrected distribution at about ± 15 ns is caused by high occupancies of 10 and beyond, where the time distribution gets wide enough that a correction based on the mean does not significantly reduce the spread.

While the time measurement of MIPs and particle tracks behaves as expected after the corrections, the impact of the occupancy cannot be eliminated fully. For analyses performed on the shower data this requires special attention the hit times in the affected region up to about 80 ns. Since instantaneous processes happening in high occupancy regions are mixed with physically delayed signals from slower hadronic processes, conclusions drawn from an analysis of the hit times in this region always have to take these
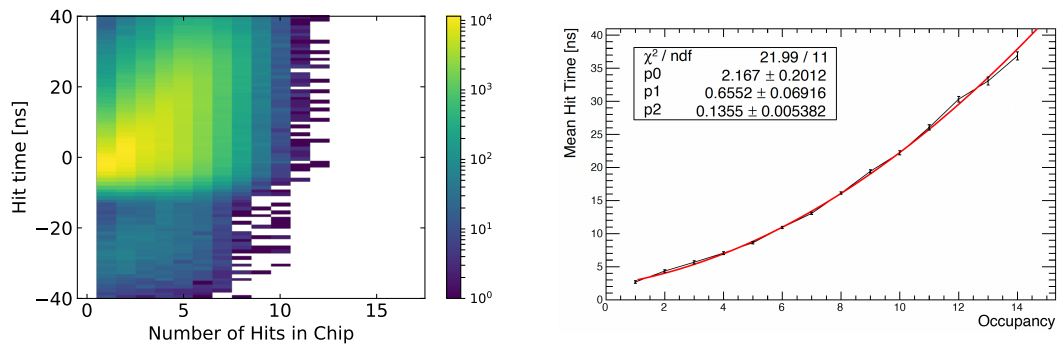
Figure 4.13: Left: Example of the occupancy dependent smearing and shift of the hit times for even BxID for an electron data set. Right: Example of the relation of mean hit time and occupancy for an individual channel. These fits are obtained channel-wise for even and odd BxID and high and low gain signals and are used to correct the mean hit time.
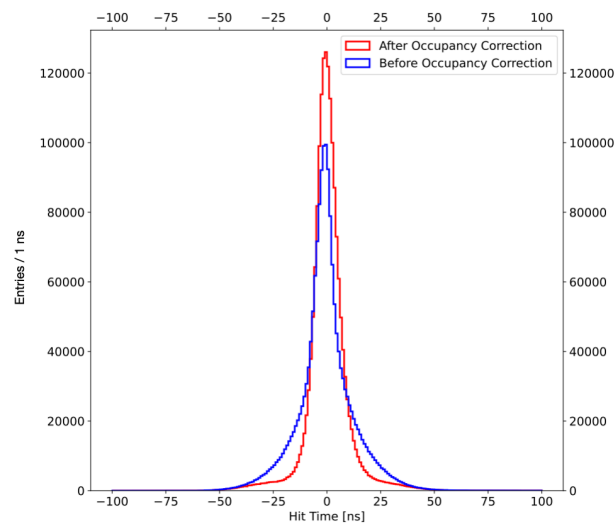
Figure 4.14: Comparison of the hit time distribution before (blue) and after (red) the occupancy correction for a pion run. The tails are significantly reduced and the symmetry of the distribution is increased. The mean is also moved closer to zero.

effects into consideration. For processes happening on the order of $100\,\mathrm{ns}$ to $1\,\mathrm{\mu s}$ after shower start the effects become increasingly insignificant. This enables quantitative analyses of the hit times in this region as performed in the following chapter.

Chapter 5

Time Measurement with the CALICE Analog Hadronic Calorimeter

The large technological prototype of the AHCAL is the first fully equipped calorimeter using the SiPM-On-Tile technology, while having realistic depth and segmentation comparable to a large scale collider detector. Furthermore, it is built with scalable components and a mechanical structure close to the final application. This features offer a well suited environment to study the detector's performance and derive statements towards the implementation of such a technology in a future collider. This chapter reports on the timing capabilities of the prototype obtained via the time resolution for MIPs, both in test beam and ILC mode (see Section 4.2). Additionally, the time structure of particle cascades is investigated.

5.1 Data Sets and Event Selection

The majority of analyses shown in this chapter are based on data recorded at the SPS in June 2018. An overview of the collected statistics is shown in Section 5.1. To investigate the time resolution for MIPs in ILC mode, a small dedicated data set recorded at DESY in August 2019 is used which will be explained in the corresponding section.

	Muons	**Pions**	**Electrons**
Energy [GeV]	40	10, 20, 30, 40, 60, 80, 100, 120	10, 20, 30, 40, 50, 60, 70, 80, 90, 100
Events	∼6.400.000	400.000 to 600.000	200.000 to 400.000
Usage	Calibration	Study hadronic response, occupancy correction	Study EM response, occupancy correction

Table 5.1: Overview of the data sets recorded in the test beam campaign in June 2018 at the SPS.

The muon data set is entirely used for calibration since the events are spread over the full detector area and produce on average one hit per layer, therefore keeping chip occupancy related effects at a minimum. Furthermore only events with a total number of hits up to 40 are used, to suppress rare showering muons and delta electrons. The constants for the time calibration explained in the previous chapter are calculated with the remaining

muon events.

5.2 Monte Carlo Event Generation

To check the performance of the simulation the detailed detector setup is also modeled in *GDML* files, including small non-uniformities and air gaps between the individual layers. For every particle type and energy corresponding simulated events are generated within DD4hep [65]. This provides a consistent framework to generate and process simulated data for reconstruction in *Marlin* [66], similar to the data sets recorded in the test beam campaign. At the heart of DD4hep, the Monte Carlo simulation toolkit GEANT4 [67] is responsible to track the generated particles throughout the detector. So called *physics lists* implement the particles and parametrizations of the possible interactions with the detector medium. The interactions are chosen at random according to their probability at a certain energy. Different models are typically contained in one physics list to extend the validity towards a wider energy range [68][69]. The detector's response in the Monte Carlo simulation is compared to the response of the real prototype. Possible deviations can then be investigated further in order to either improve the simulation or isolate imperfections in the detector.

To ensure comparability between independent analyses, 100000 events for each particle type and energy are generated in a centralized production run. To investigate the accuracy of different models in predicting the detectors response to particles, two physics lists called QGSP-BERT-HP and FTFP-BERT-HP are used to generate the events. A brief overview of the detector model and simulation of the electronics is given below.

Detector Model

Figure 5.1 shows a sketch of one layer as it is implemented in the simulation for the June test beam. In total, 39 of those layers are arranged to resemble the AHCAL technological prototype as close as possible. In order to decrease the number of individual volumes in GEANT4 to save computation power, the scintillator is not segmented into tiles, but treated as a plate of polystyrene as large as the front face area of the calorimeter. The segmentation of the energy depositions is done after the simulation step. Furthermore, not every detail of the electronics on the circuit board is implemented, but approximated by a layer of material mixture that resembles on average the composition of ASICs, conductors and analog components. On a more detailed level, the dead areas between the scintillator tiles in the real detector are also included in the simulation. Energy depositions close to the boundary layer between two tiles are discarded. Since the scintillator is simulated as one plate, this is purely based on the position information of the energy deposition.

Digitization

The digitization implements functionality to transform the raw energy depositions from GEANT4 to the realistic response of the detector including all the effects from the signal
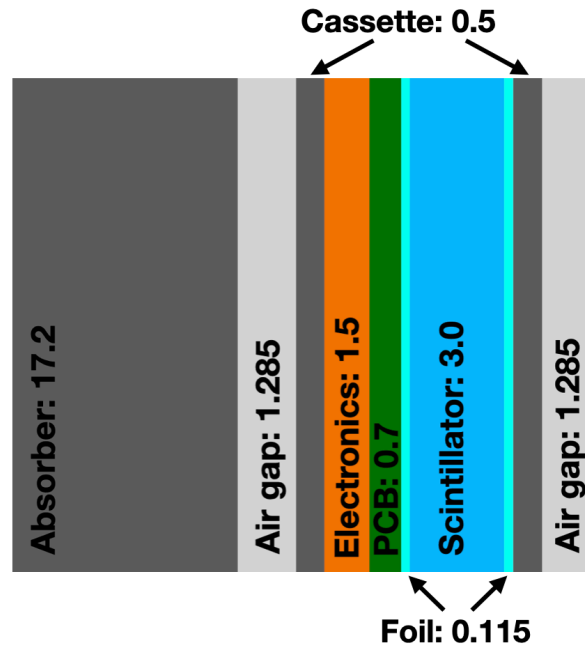
Figure 5.1: Sketch of an AHCAL layer in simulation. The thickness of the components is shown in mm.

generation and electronics. As a first step, the energy depositions in GeV are transformed to the MIP scale using the *MIP to GeV* factor. This factor is obtained by obtaining the hit energy spectrum of minimum ionizing muons and extracting the most probable value, similar to the energy calibration in the AHCAL briefly explained in Chapter 4. After the conversion the effects of the signal shaping are implemented by summing up all the energy depositions inside a channel within a 50 ns window. The effects introduced by the SiPM are treated next. First the number of theoretically fired pixels is calculated from the deposited energy, including the saturation effects. This number is smeared using a Poissonian probability distribution to replicate the photon counting. In order to produce an output file that encodes the simulated data in terms of the same units produced by the detectors DAQ, the energy is transformed from fired pixels to ADC counts. In this way, the same reconstruction code for Marlin can be used to process simulated and real data. Finally the hit times from GEANT4 are modified by a Gaussian distribution to resemble the real detectors response. A detailed description of the digitization is found in [62].

5.3 Measurement of the MIP Time Resolution

The design goal of the AHCAL in terms of time resolution for tracks of Minimum Ionizing Particles (MIP) is below 1 ns. As shown in Figure 5.2 on the left the characteristic signature of a minimum ionizing muon is one energy deposition per layer, therefore effects

Figure 5.2: The left image shows a 40 GeV muon event in the AHCAL. The MIP-like particle penetrates the detector without causing considerable particle multiplication. The right image shows a 60 GeV pion event in the calorimeter. After penetrating the first few layers on the left, an inelastic hadronic interaction causes a hadronic shower to form.
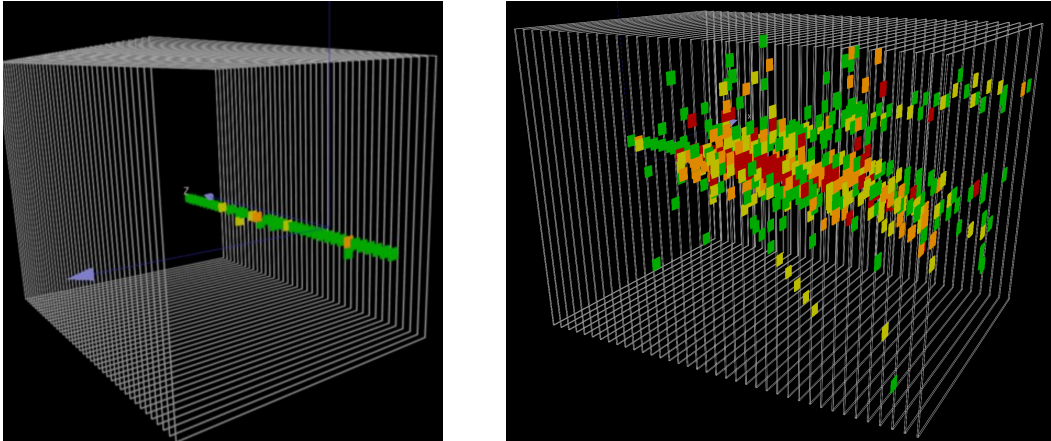
caused by rising chip occupancy inside particle showers (right side of Figure 5.2) are minimal and the timing performance of individual channels can be extracted.

The following analysis reports on the MIP time resolution for test beam mode and ILC mode using the slow and fast bunch clock, respectively. As explained in Section 4.2, the ILC mode is expected to outperform the test beam mode in terms of time resolution.

5.3.1 Testbeam Mode

The intended measurement length in ILC mode within one BxID is 200 ns, corresponding to the nominal bunch spacing in the ILC. Since most of the test beam facilities don't supply particles at this rate, data taking in this mode will lead to a lot of empty BxIDs within read out cycles. The test beam mode is intended to take efficient data at lower rates by increasing the bunch crossing duration by a factor of 20, but this also reduces the achievable theoretical time resolution by the same factor. It is nevertheless interesting to investigate the timing behavior in this mode to isolate possible issues in the electronics. The used data set to obtain the MIP time resolution consists of events of 40 GeV muons spread over the 4 quadrants of the detector to hit each of the 4 HBUs per layer. Odd behaviors in the response can thus be detected.

Figure 5.3 shows the mean and the standard deviation of the hit time distribution per layer. While a slight trend towards later hit times and wider distributions exists with increasing depth, no outliers are visible. These trends are mostly from failed calibrations for individual channels and an investigation on the channel level did not show any significant outliers. To calculate the single channel time resolution the distribution of the hit time difference for subsequent pairs of layers is obtained, in order to eliminate distortions from the trigger electronics. Since the trigger signal is generated externally
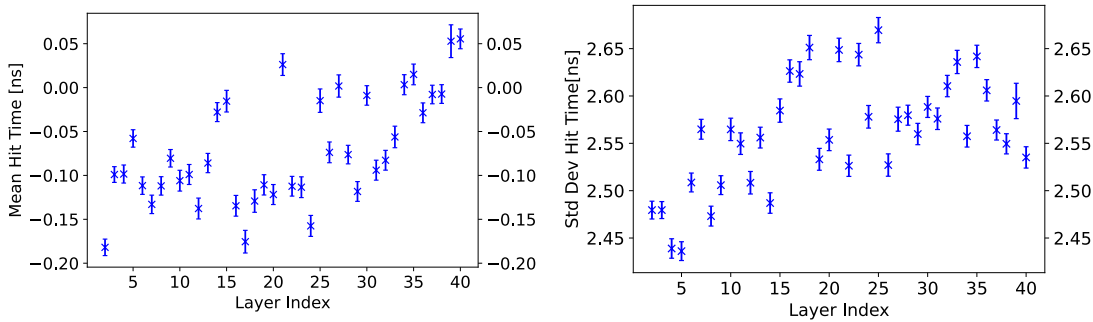
Figure 5.3: Mean hit time (left) and standard deviation of the hit time (right) for the individual layers of the AHCAL.
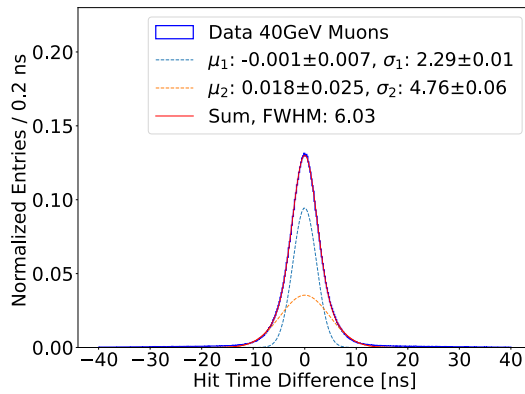
Figure 5.4: Distribution of the hit time difference in test beam mode. A single Gaussian does not describe the distribution in the tails so a sum of two Gaussians in chosen instead. The width of the full distribution is given in terms of the Full Width at Half Maximum (FWHM).

and independent of the activity in the calorimeter, the time measurement in every layer is interpreted as independent. Therefore, the single channel resolution is obtained by dividing the standard deviation of the hit time difference by a factor of $\sqrt{2}$. The left side of Figure 5.4 shows the distribution and the sum of two Gaussian functions fitted to it. This is necessary to describe the tails of the distribution and their evolution with rising hit energy. The resolution derived from the smaller Gaussian is 1.626 ± 0.015 ns with a Full Width at Half Maximum (FWHM) of the full distribution of 6.3 ns.

Since the calorimeter is intended to measure the times of hits within particle showers it is also necessary to investigate the scaling of the time resolution with the hit energy. Therefore the hit energies are binned and the time resolution is determined per bin. Figure 5.5 shows the evolution of the width of the two Gaussian contributions versus the hit energy, whereas the horizontal error bars show the bin width. The energy dependent resolution is best described by an exponential decay of the form
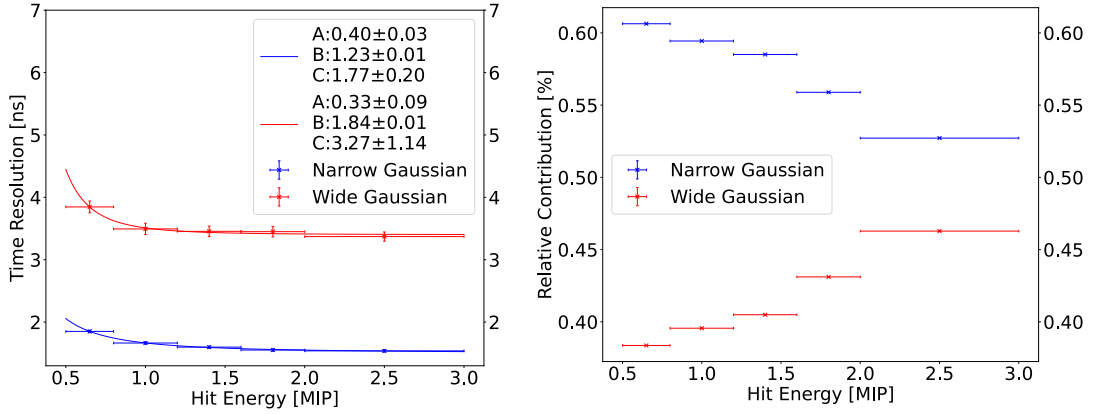
Figure 5.5: Left: Energy dependent time resolution derived from the narrow and wide Gaussian, parameterized with Equation (5.1). Right: Relative contribution of the two Gaussian contributions to the sum measured by the fraction of the area.

$$\text{Time Resolution} = \frac{A}{E^C} + B, \tag{5.1}$$

with E being the hit energy. The fit results of this function to the data shows that the resolution of the narrow contribution scales with an exponent of C = 1.77 while the wide Gaussian scales almost cubic, with C = 3.27. In order to fully understand the scaling of the width of the hit time distribution the relative contribution of the narrow and wide gaussian to the overall hit time distribution has to be understood. The right side of Figure 5.5 shows the area of the two Gaussians relative to the total area of the distribution. With both the distributions decreasing with rising hit energy, the relative contribution of the wider Gaussian increases. This implies that the time measurement acquires an additional distortion that increasingly widens the distribution as the hit energy increases, probably due to the increased charge stored on the chip.

To shed more light on the timing properties of the SiPM-On-Tile technology without having the electronics of the full prototype, a dedicated beam test was conducted which is the subject of Chapter 6. This is also beneficial to understand the contribution of the AHCAL electronics on the timing performance by de-convolving both effects.

5.3.2 ILC Mode

In addition to the extensive beam test at SPS in 2018, a small scale test was conducted at DESY in 2019. The setup consisted of only 5 layers of the detector without absorber, but the DAQ ran in ILC mode with a factor 20 of increased theoretical time resolution. Furthermore, inspired by the lessons learned from correcting the time shifts recorded in 2018, the DAQ software was upgraded to prevent the shifts to occur. This also implies, that the amount of calibration constants needed per channel is drastically removed by about 66%. The design goal of the AHCAL is a time resolution of 1 ns or below in this

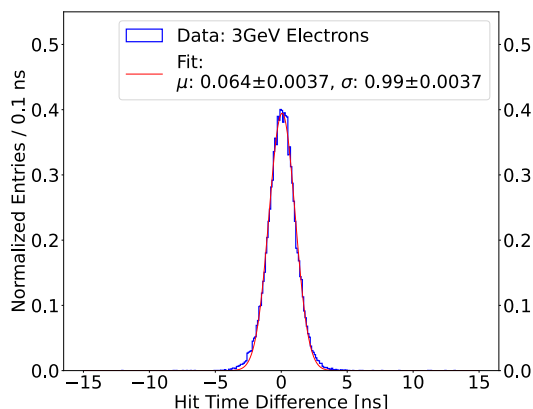Figure 5.6: Distribution of the hit time difference in ILC mode. In contrast to test beam mode, this distribution is well described by a single Gaussian. The resulting time resolution, obtained by dividing its width by $\sqrt{2}$ is $700\pm3\,\text{ps}$.

mode of operation. Due to a faulty connector in the 2019 beam test at DESY, which resulted in a drift of the time reference, only a small data set of 15000 events is used for this analysis.

Figure 5.6 shows the distribution of the hit time difference of subsequent channels parameterized by a Gaussian function. By dividing the variance of this function by $\sqrt{2}$ a single channel resolution of ($700\pm3\,\text{ps}$) follows, hence the design goal for the MIP time resolution could be achieved. Operation of the full calorimeter in ILC mode has been completed June 2022 at CERN, with the goal of investigating the severity of the occupancy related effects with the fast bunch clock.

5.4 Time Structure of Electromagnetic and Hadronic Showers

While the time stamping of MIP-like signatures and showers in a calorimeter is a helpful tool for background rejection and the association of events in the tracking detectors to calorimeter hits, a major advantage of single cell timing is the investigation of the time structure of particle showers. This is not only vital to improve our current understanding of shower formation to update the models in the Monte Carlo event generation, but also to increase the accuracy of the energy reconstruction. Especially hadronic showers are known to have a delicate time structure because of nuclear processes like spallation and neutron evaporation of excited atoms. Compared to the instantaneous processes like inelastic scattering, they happen on a longer time scale of $1\,\text{ns}$ to several tens of μs, if slow neutrons are generated. Since these neutrons usually deposit only a fraction of their kinetic energy in the active elements of the detector before escaping, the linear conversion from visible to total energy of the primary particle, which accounts for the sampling fraction of the calorimeter (Section 3.3), cannot be applied. Furthermore, the energy used to break up nuclei of the detector medium in spallation and neutron capture

reactions is intrinsically invisible to the calorimeter. By isolating these processes in the time domain, dedicated scaling factors can be obtained to account for a different response of the detector. This is one aspect of a technique called *software compensation* [70] which is described in more detail in [64].The following sections report on the time structure of electromagnetic and hadronic showers measured with the AHCAL.

Electromagnetic Showers

In theory, the electromagnetic shower should not have a specific time structure and very minor event by event fluctuations as explained in Figure 3.4. Paired with the high energy density of electromagnetic showers, this property is beneficial to benchmark the calorimeter's performance for high hit energies without being biased by delayed hadronic energy depositions.
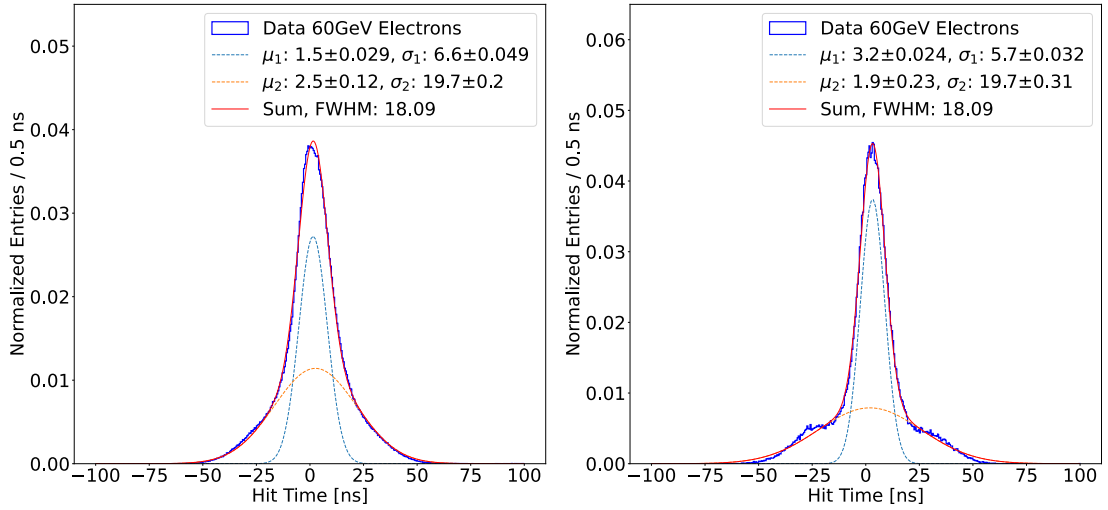
Figure 5.7: The left figure shows the hit time distribution for $60\,\mathrm{GeV}$ electrons after calibration. The remnants of the chip occupancy issue discussed in Section 4.3 are clearly visible in the pronounced tail and the slightly shifted mean of the gaussian fits. It is even more pronounced for hits above an energy of $10\,\mathrm{MIP}$ (right figure), because this cut favors the center of the electromagnetic shower where energy density and occupancy are high.

The left side of Figure 5.7 shows the resulting hit time distribution for a $60\,\mathrm{GeV}$ run after calibration. Similar to the muon runs, the distribution is best parameterized by a sum of two Gaussian distributions. The remnants of the chip occupancy issue discussed in Section 4.3 are clearly visible in the pronounced tail and the slightly shifted mean of the Gaussian fits. By rejecting hits below an energy of $10\,\mathrm{MIP}$ to extract the hits in the shower center, where the occupancy and charge stored on the chip is high, this effects are even more pronounced. Only the width of the narrow Gaussian decreases which is expected because the time resolution should increase for high hit energies, assuming the
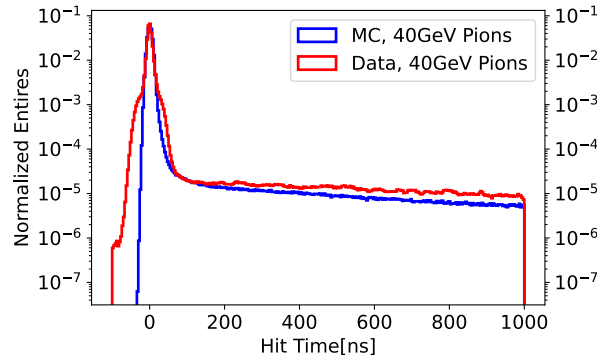
Figure 5.8: Hit time distribution of pion events in data and simulation. Data shows a significant contribution of the remaining occupancy smearing around 20 ns to 80 ns. The simulation is modified by a Gaussian smearing of 6.6 ns, inspired by the width of the narrow Gaussian obtained for the electron events. While the distributions agree around the peak and the shoulder at 100 ns, the tail is not accurately represented in simulation.

system is free of additional distortions. For the discussion of hadronic showers and the comparison to Monte Carlo data, a Gaussian smearing of 6.6 ns is applied to the hit times produced by GEANT4, inspired by the width of the narrow Gaussian.

Hadronic Showers

The occupancy related effects also impact the time distribution of hits in a hadronic shower, in many cases more severely than in electromagnetic ones due to its larger dimensions. However, the spallation and elastic processes contribute to a very delayed tail of the hit time distribution and should be resolved nevertheless. It is caused by neutrons with a typical kinetic energy of a few MeV [47]. Due to their low cross section and non-relativistic energy they produce delayed hits at a time scale that is orders of magnitude longer than the time resolution, and can be resolved reliably.

The signature of these processes is clearly visible in the tail of the hit time distributions of data and simulation shown in Figure 5.8. While the disagreement in the range of 20 ns to 80 ns is caused by the occupancy issue and the increasing width of the hit time distribution with rising hit energy (see Section 5.3.1), the difference in the tail of the distribution is caused by the modeling of the hadronic processes in simulation. To extract the disagreement between data and Monte Carlo in the late part of the hadronic shower, the fraction of hits later than 100 ns is a sensitive observable. Figure 5.9 shows this fraction for data (left) and Monte Carlo (right), for all layers of the detector.

For energies up to 40 GeV the shape of the data points is in good agreement with the simulation, but an offset of 0.005 in the absolute values is present. For the high energy particles the data begins to differ significantly from the Monte Carlo. The fraction of late hits in data rises linearly to the maximum around layer 28, while the simulation shows a more moderate and non-linear increase towards the maximum around layer 31.
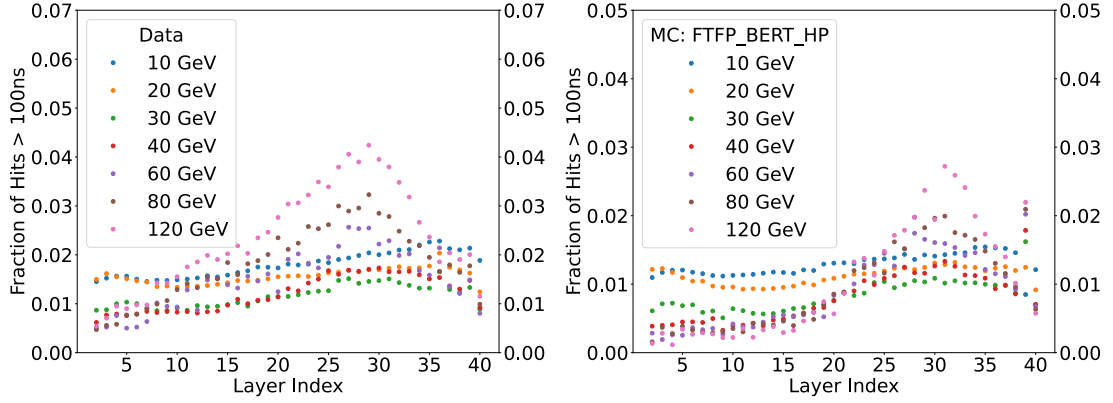
Figure 5.9: Layer-wise fraction of hits later than 100 ns for data (left) and simulation (right). The simulated samples are taken from a centralized data production used by every analysis on the AHCAL to ensure comparability.

Two possible explanations for the observations are discussed in the following.

A fundamental difference between the test beam environment and the simulation is the quantization of the acquisition time into bunch crossing IDs. In simulation, the duration of one event is defined by the time until all particles, primary and secondary, are either leaving the detector or stopped. Depending on the neutron content this can take several microseconds. In data, the maximum amount of time is limited to 4000 ns, regardless of the neutron content. Consequently, neutrons generated by the previous event can still deposit energy in the acquisition window of the following event, simply because they still propagate through the detector. This *afterglow* is very hard to pick up in the energy domain since these hits only contribute a small amount to the total visible energy.The constant event rate in a test beam environment, however, leads to a build-up of slow neutrons in the detector. Assuming they are isotropically distributed they increase the chance of late hits in the first layers of the calorimeter.

Another possibility is the incorrect modeling of the neutron yield and their spatial distribution in simulation. A higher yield in reality would explain the offset in the fraction of late hits that is observed throughout the detector. A higher probability of backscattering or emission of neutrons in upstream direction would increase the fraction of late hits in the first layers of the calorimeter.

The available data set from the test beams in 2018 with the fully equipped prototype are not suited to disentangle these possibilities, because the afterglow and a higher overall neutron yield are indistinguishable. Taking data with a sufficiently long dead time between events for the neutrons to disappear can provide insight, but this will also lead to very inefficient data taking and the accumulation of enough statistics to draw significant conclusions will take a long time. In future test beams however, this issue should be addressed.

5.5 Discussion of the Results

Compared to the results obtained with the physics prototype [64] the MIP time resolution in test beam mode was increased by about 50% for both Gaussian contributions. The main difference of the prototypes is the updated ASIC from SPIROC2B to SPIROC2E, as well as an external trigger time stamp provided by the BIF. The main source of uncertainties in this analysis arises from the shifted hit times in particular read out cycles. Since the correction of the shifts requires a fragmentation of the data set in shifted and non-shifted cases and dramatically reduces the number of events available for calibration of the individual channels, especially the higher memory cells are calibrated poorly. For the first time the detector was operated in ILC mode and outperformed the test beam mode, as expected. The design goal for the MIP time resolution of the AHCAL in this mode is at 1 ns or better, which is clearly achieved with a measured resolution of (700±3 ps). The occupancy problem still exists and is especially problematic for particle showers. A channel wise correction got implemented and the width of the narrow Gaussian contribution to the hit time distribution for showers could be recovered to 6.6 ns, which is comparable to the width of the MIP hit time distribution. This additional calibration, however, only corrects the mean hit time shift per occupancy. The additional broadening of the distribution cannot be corrected and leads to pronounced tails for electrons and hadrons. Since this behavior distorts times between 20 ns to 80 ns, reliable comparisons to simulations are only shown for later hit times. Globally, the FTFP–BERT–HP physics list used for simulation of the pion events underestimates the total number of hits later than 100 ns by about 25%. Also the evolution of the late hit content per layer is slightly mismodeled, possibly due to neutron afterglow from previous events or imperfections in the simulation. To investigate these effects, specialized data sets have to be recorded in upcoming test beam campaigns. Since the shift in the hit times got prevented in software, the imperfections in the time calibration are expected to decrease for future data taking. A pending measurement planned for beam test in 2022 at CERN addresses the behavior of the detector for hadrons in ILC mode and the corresponding impact of the occupancy effects.

Chapter 6

The Intrinsic Time Resolution of the SiPM-On-Tile Technology

The time measurement done with large calorimeters like the CALICE AHCAL (Chapter 4) includes effects caused by the involved data acquisition system and calibration procedure. This introduces unavoidable distortions into the time measurement which shadow the pure performance of the combination of scintillating tile and SiPM. To measure the *intrinsic* and energy dependent time resolution of the SiPM-on-Tile configuration, a dedicated beam test setup was designed with minimal electronics which requires only a small number of calibration values. The setup was used at the DESY testbeam facility [71] in Hamburg in October 2020. This chapter explains the setup and reports the results of the measurement.

6.1 Test Beam Setup and Data Taking

To make the setup as simple and understandable as possible a beam telescope like configuration of four channels was assembled. The sensors of this kind have been developed in the scope of the CLAWS [72] beam monitoring system for the SuperKEKB [73] accelerator. A sketch of the setup is shown in Figure 6.1 on the right. The sensors CA, CC,CE and CG (left side of Figure 6.1) labeled according to the input of the digitizer are assembled as a stack which the electron beam will penetrate. CA and CG are used as coincidence triggers, CC and CE are taking data to perform the time resolution analysis. Using Cat7 Ethernet cords the power and signal lines of the sensors are connected to the receiver box containing the voltage supply which is controlled and powered from the DAQ Computer by a USB3 connection. The receiver board also routes the analog signal to the digitizer using BNC cords. This digitizer, a PicoScope 6000E manufactured by Pico Technology, is capable of sampling the complete analog signal at a rate of 2.5 GHz on four channels, at a peak trigger rate of 300 kHz. The digitizer is controlled by the DAQ computer that also saves the full analog waveform of each channel to a binary format once the PicoScope's internal memory of 2 giga samples is filled. This offers the possibility of offline signal analysis without prior conditioning and a potential loss of information.

The setup's flexibility enables the quick exchange of sensors without suffering from extended downtime within the data taking period. By equipping multiple sensors with different scintillating tiles and materials, a variety of SiPM-on-Tile configurations can
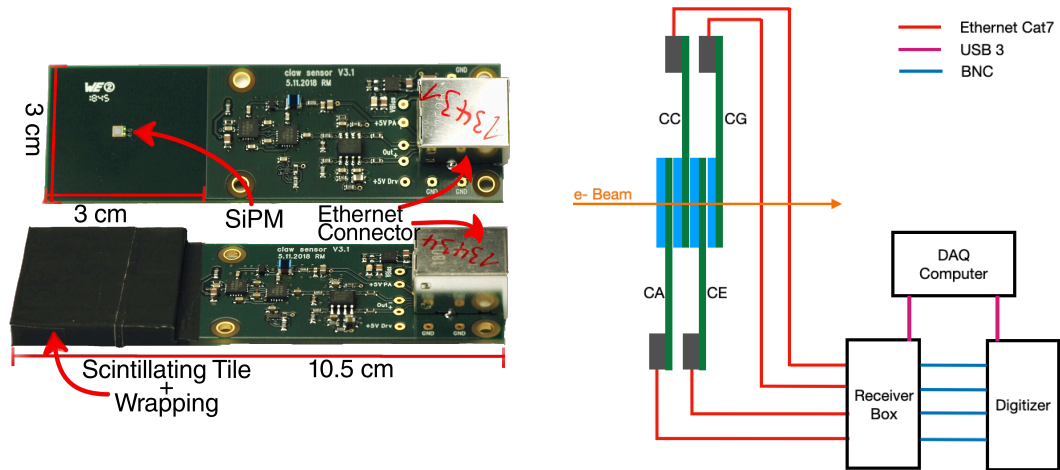
Figure 6.1: The left image shows a picture of the sensors used for the beam test setup. The bare sensor on top can be equipped with different kinds of wrapped scintillator tiles. The signal from the SiPM gets amplified and sent to the receiver box via ethernet. The right sketch shows the beam test setup. The sensors labeled CA, CC, CE and CG are placed in the electron beam and connected to the receiver box which houses the power supply for the SiPMs and amplifiers. It also forwards the signal to the digitizer. Receiver box and digitizer are controlled by the DAQ computer.

be investigated. The setup was successfully tested at the DESY test beam facility in October 2020. The recorded data sets used for the studies in this thesis are listed in Table 6.1. Two large sets have been collected with the same $30\,\text{mm} \times 30\,\text{mm} \times 3\,\text{mm}$ tiles used in the AHCAL to compare the performance. Furthermore, since the setup of a single channel is the same, the influence of the AHCAL electronics on the time resolution can be extracted. Additionally, two datasets using the BC408 scintillator have been recorded, one with a tile of the same size as the AHCAL tiles and another one with smaller $20\,\text{mm} \times 20\,\text{mm} \times 3\,\text{mm}$ tiles. This scintillator features a higher light output and is used to investigate the influence of the scintillator properties and size on the time resolution. During the recording of events with a $3\,\text{GeV}$ particle beam, dedicated calibration runs are performed at regular intervals. These runs contain single pixel waveforms of the SiPMs on every channel to calibrate the energy scale of the signals and to monitor the detectors stability. The coincidence trigger threshold on channel A and G to record the beam events was set to $25\,\text{mV}$ (see right side in Figure 6.2). This is necessary to reduce the fake trigger rate due to coincident single photon noise with an amplitude of about $12\,\text{mV}$. For recording the calibration waveforms each individual channel was set to a trigger threshold of $7.5\,\text{mV}$ without coincidence (see left side in Figure 6.2) to reliably trigger on the random single photon signals.

ID	Scintillator	Scintillator Size	Absorber	Timebase	Events
1	AHCAL	$30\,\text{mm} \times 30\,\text{mm} \times 3\,\text{mm}$	No	400 ps	$1.87 \cdot 10^8$
2	AHCAL	$30\,\text{mm} \times 30\,\text{mm} \times 3\,\text{mm}$	20 mm Tungsten	400 ps	$1.16 \cdot 10^8$
3	BC 408	$30\,\text{mm} \times 30\,\text{mm} \times 3\,\text{mm}$	No	400 ps	$1.45 \cdot 10^8$
4	BC 408	$20\,\text{mm} \times 20\,\text{mm} \times 3\,\text{mm}$	No	400 ps	$1.29 \cdot 10^8$

Table 6.1: Datasets used for the time resolution studies in this thesis. The AHCAL scintillator features the same properties as the one used in the AHCAL technological prototype (Chapter 4). The tungsten absorber is placed in front of the setup to create electromagnetic showers to reach higher hit energies.
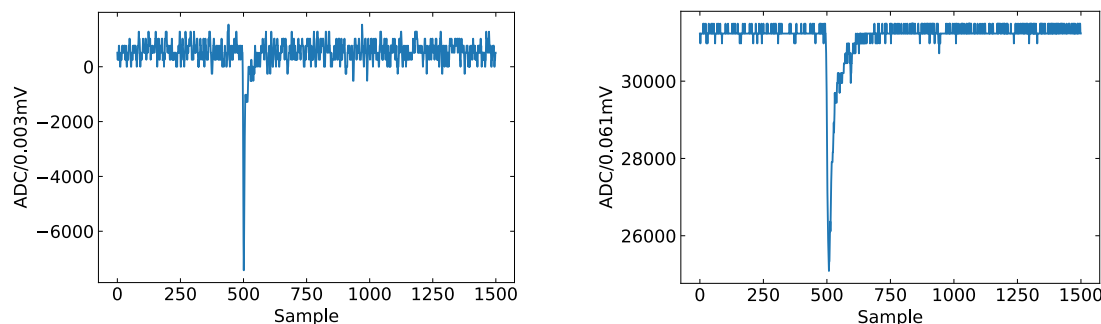

Figure 6.2: Left: Raw calibration waveform. It corresponds to a single detected photon, higher signals are a superposition of these waveforms. Right: Raw signal waveform. It is caused by an electron traversing the scintillator and creating photons, which get detected by the SiPM.

6.2 Event Reconstruction and Calibration

After recording and saving of the data and calibration waveforms they have to be reconstructed and calibrated to obtain the time and energy information of the individual channels. Typical raw calibration and data waveforms before any event reconstruction is performed are shown in Figure 6.2.

The amplitude and timescale of these waveforms is saved in terms of ADC counts and sample numbers, respectively, so the first step in the event reconstruction is the transformation to the mV and nanosecond scale. Every sample index corresponds to a time interval of 0.4 ns. For recording the calibration waveforms a maximum channel voltage of 50 mV was used, which results in a conversion factor of 1ADC = 50mV/32512 = 0.0015mV, using a maximum ADC value of 32512. The data was taken with a maximum channel voltage of 1000 mV so the conversion factor is 1ADC = 1000mV/32512 = 0.0308mV. Additionally, the pedestal value of the waveform is subtracted. The scaled waveforms are shown in Figure 6.3. The next step is the calibration of the energy scale. Depending on the type of analysis two units of energy deposition may be needed. The number of detected photons
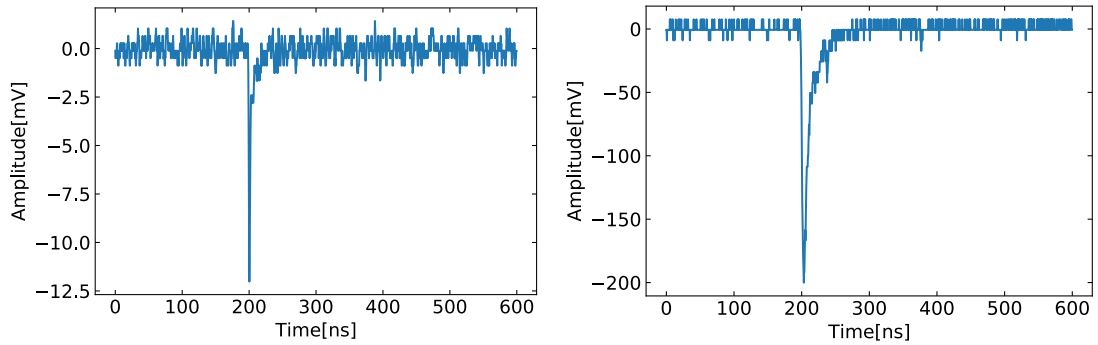
Figure 6.3: Left: Scaled calibration waveform. The sample number and ADC counts are transformed to SI units. Right: Scaled signal waveform. As a superposition of calibration waveforms they have a larger amplitude and longer decay time.
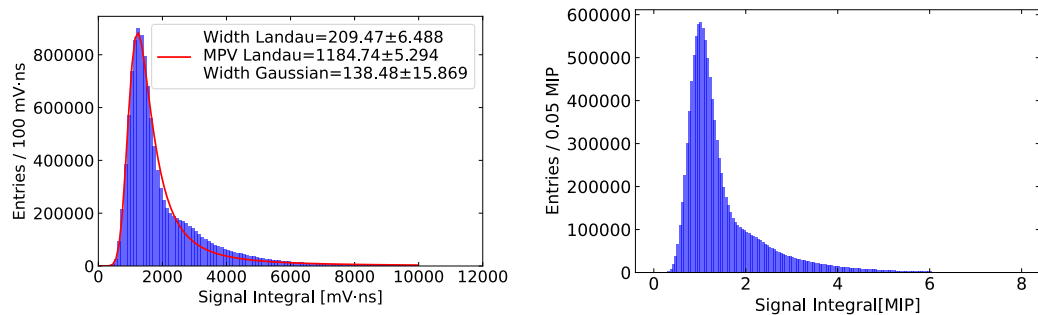
Figure 6.4: MIP calibration. The left image shows the distribution of the signal integral as well as a convolution of a landau and gaussian distribution fitted to it. The mismatch at around $3000\,\mathrm{mV\,ns^{-1}}$ is caused by double particle events. The most probable value of the convolution is used to scale the data to the MIP scale shown in the right histogram.

(PE - photon equivalent), or the MIP equivalent which is the most probable energy a minimum ionizing particle (MIP, see Chapter 3) deposits in one channel.

MIP Calibration

First, the energy spectrum is obtained by integrating the scaled signal waveforms of one run and filling the results into a histogram. Subsequently, a Langaus distribution (see Section 3.1.3) is fitted to the histogram to extract the most probable value (MPV) which is used as the calibration factor from mVns to MIP as it is shown in Figure 6.4. Since the MPV of the convolution is not a fit parameter, its value and error are estimated by numerical methods using the fit parameters.

To calibrate each individual event to the MIP scale, the integrated waveforms are scaled with the resulting calibration factor. Depending on the light yield of the scintillator, its dimensions and the characteristics of SiPM and electronics, these calibration values differ

ID	Channel A mVns/MIP	Channel C mVns/MIP	Channel E mVns/MIP	Channel G mVns/MIP
1,2	1224.07±0.32	942.88±0.28	1031.34±0.26	1110.85±0.30
3	1663.98 ±0.38	1487.46±0.36	1227.35±0.27	1607.16±0.28
4	1499.82±0.20	1570.96±0.29	1696.34±0.31	1203.36±0.37

Table 6.2: MIP calibration constants for the different datasets. These constants are used to scale the hit energy from mVns to MIP.

ID	Channel A mVns/PE	Channel C mVns/PE	Channel E mVns/PE	Channel G mVns/PE
1,2	65.16±0.08	65.37±0.08	63.48±0.06	66.73±0.07
3	66.07±0.07	65.49±0.06	63.53±0.06	68.75±0.07
4	66.20±0.07	71.93±0.07	70.71±0.08	66.24±0.07

Table 6.3: PE calibration constants for the different datasets. These constants are used to scale the hit energy from mVns to PE.

from dataset to dataset and from channel to channel. The MIP calibration absorbs these differences so performance parameters of the setup like energy or time resolution can be directly compared on a common energy scale. The calibration factors for the different channels and datasets are shown in Table 6.2.

PE Calibration

In contrast to the MIP calibration, the PE calibration retains the characteristics of scintillator and SiPM so the impact of different detector setups on the performance can be compared. To calibrate the energy scale from mVns to PE, the integral of the signal waveform has to be divided by the average area of the calibration waveforms. These waveforms correspond to a single fired pixel. Since a SiPM signal is a sum of the waveforms of individual pixels, the ratio of the areas results in the number of fired pixels, hence the number of detected photons. The calibration factors for the different channels and datasets are shown in Table 6.3.

The last step in the event reconstruction is the calibration of the hit times in channel C and D relative to the trigger time obtained with channel A and G. Two ways of obtaining hit times are used in this work, the constant threshold discrimination and the constant fraction discrimination.
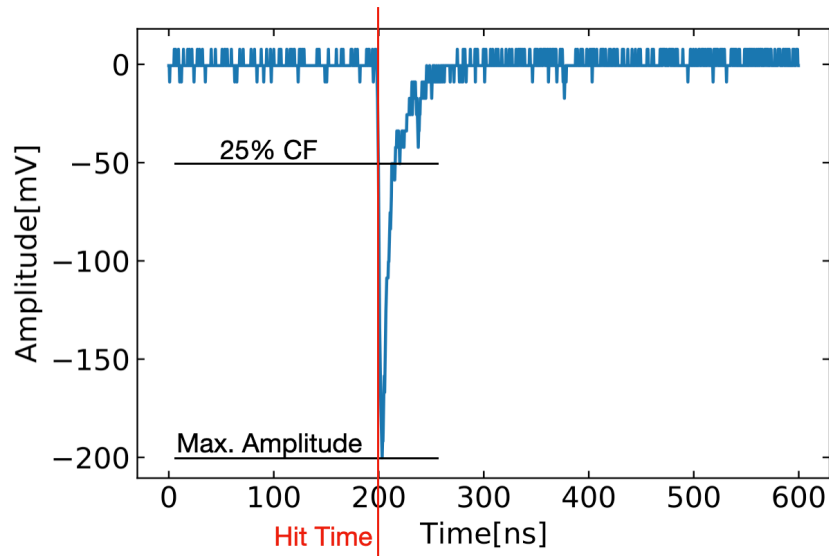
Figure 6.5: Constant fraction discrimination. The threshold (CF) is applied at 25% of the maximum amplitude.

Constant Threshold Discrimination

As shown in Figure 6.3 on the right the scaled waveforms consist of a steeply rising flank and a slower falling flank. The hit time corresponds to the signal time at which the rising flank crosses a predefined threshold voltage. This threshold has to be high enough to be above the pedestal value of the signal and low enough to cross the signal at all. A value of 25 mV has shown to be well suited for the total energy range of the signals, since it rejects the single photon noise with an amplitude of 12 mV while keeping the higher signals from the electrons. The trigger time is calculated as the average hit time of the trigger channels A and G. The hit times in channel C and E are obtained relative to the trigger time by subtraction.

Constant Fraction Discrimination

In contrast to the previous method, constant fraction (CF) discrimination uses a variable threshold. For every individual signals it is set to a predefined fraction of the signals maximum amplitude to mitigate the impact of time walk previously discussed in Section 4.3. This also makes sure that the threshold is never higher than the maximum amplitude of the signal. A sketch of the method is shown in Figure 6.5. A constant fraction of 25% is used for the analyses presented in this chapter. Trigger and hit times are obtained in the same fashion as the constant threshold discrimination.
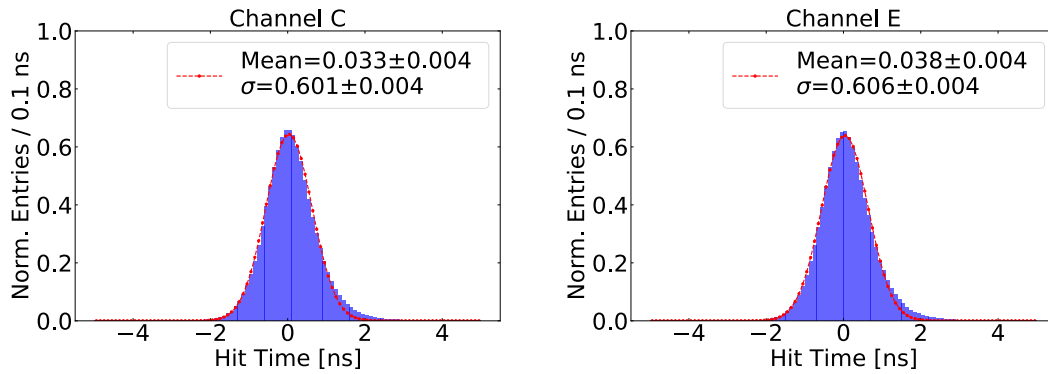After the event reconstruction the data is saved for subsequent analysis.

Figure 6.6: Time distribution of channel C and E of the AHCAL dataset. The slight mismatch of fit and distribution is caused by different hit energies and is investigated in Section 6.4.

6.3 Measurement of the MIP Time Resolution

This section explains the details of the analysis performed to obtain the intrinsic time resolution for MIPs. By comparing the result to the achieved MIP time resolution of the AHCAL prototype the impact of its front end electronics and time calibration procedure can be investigated. Furthermore, this measurement serves as a guideline for simulation studies as it provides realistic performance parameters for the design of future detector systems based on SiPM-on-Tile technology.

To calculate the single channel time resolution the hit time distributions for the individual channels C and E are obtained from the calibrated data files. For this analysis, hit times obtained with constant fraction discrimination are used and the time walk correction is omitted because it was proven that it has no effect. The distributions for channel C and E from the dataset collected with the AHCAL scintillator (data set 1 and 2) are shown in Figure 6.6. Additionally, a gaussian function is fitted to the histograms to extract their properties. As expected, the distributions are in very good agreement. The overall shape of the gaussian is reproduced in the histograms with a slight mismatch on the right flanks. This mismatch is caused by the fact that this analysis is not sensitive to the different signal amplitudes which cause an energy dependence of the timing performance. This effect is investigated in detail in Section 6.4.

The distributions still contain the finite trigger resolution and systematics that affect both channels in the same way. These effects are suppressed by calculating the difference of both hit times per event. The resulting distribution and the fitted gaussian function are shown in Figure 6.7. Under the assumption that the two channels C and E are independent and follow the same underlying distribution, the single channel time resolution for MIPs is obtained by dividing the width of the gaussian fit by $\sqrt{2}$ (see Section 5.3) resulting in a value of 466 ± 4 ps.

The results for the datasets 1, 3 and 4 are summarized in Table 6.4:

The difference in time resolution of sample 1 and 3 can be attributed to the higher
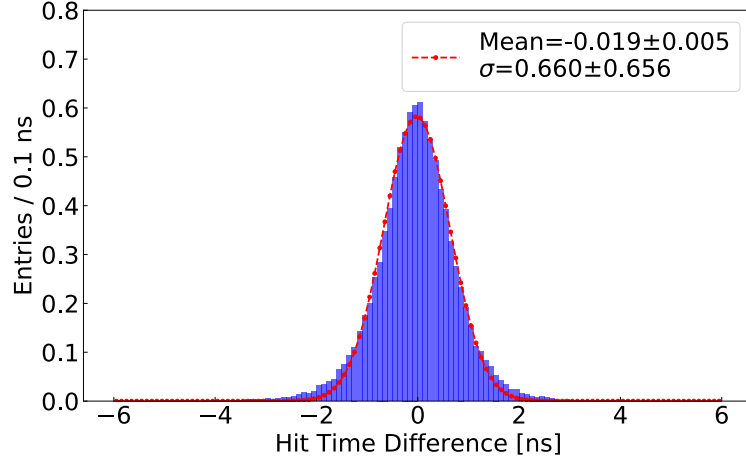
Figure 6.7: Hit Time Difference for the AHCAL dataset. From the width of this distribution the single channel time resolution can be calculated by dividing the width by $\sqrt{2}$ resulting in a value of $466\pm4\,$ps.

ID	Scintillator	Scintillator Size	Timebase	MIP Time Resolution
1	AHCAL	$30\,\mathrm{mm} \times 30\,\mathrm{mm} \times 3\,\mathrm{mm}$	400 ps	$466\pm4\,$ps
3	BC 408	$30\,\mathrm{mm} \times 30\,\mathrm{mm} \times 3\,\mathrm{mm}$	400 ps	$445\pm4\,$ps
4	BC 408	$20\,\mathrm{mm} \times 20\,\mathrm{mm} \times 3\,\mathrm{mm}$	400 ps	$340\pm2\,$ps

Table 6.4: Single channel MIP time resolutions of the used data sets. Data set 2 is not used, because it contains events of electromagnetic showers.

scintillation yield of BC408. A higher light output leads to a steeper rising edge of the analog waveform and reduces the statistic event-by-event fluctuations. This reduces the width of the distribution of the hit times in the individual channels and consequently increases the time resolution. The significantly increased resolution of sample 3 is caused by multiple factors. First, the reduced size of the tiles increases the light collection efficiency of the setup and leads to an increased number of detected photons per event. Similar to increasing the scintillation yield of the scintillator, this also leads to a steeper rising flank and reduced statistical fluctuations. Previous work has shown, that the light yield of the setup scales with $1/\sqrt{A}$, with A being the area of the tile [74]. A second reason is the decreased path length of the scintillation photons from the creation point to the SiPM. Whether this effect depends on the volume of the tile or its area, or a combination of both, is currently under study and in some aspects discussed in the next section. The different timing properties have to be considered in the design of a calorimeter since one can significantly increase the resolution by reducing the area of the channels without changing the material budget, thus maintaining the uniformity of the

detector. An increased channel count has to be considered for obtaining a reasonable cost estimate of the detector, but dedicated timing layers with optimized layout could be installed at optimized positions within the system to tailor the timing capabilities to specific needs of an experiment.

In the next section the hit energy dependence of the time resolution is investigated.

6.4 Energy Resolved Time Resolution

Since calorimeters are used to perform measurements on particle tracks as well as showers and individual particles created within them, the possible hit energies are distributed over a wide range. The high energy density within electromagnetic showers produces hit energies often exceeding 100 MIP, while isolated energy depositions from neutrons produced in hadronic showers are often considerably below an energy of 1 MIP. Using only the MIP time resolution to characterize a detector is not enough to correctly describe the performance over the full energy range. Additionally, investigating the energy dependence of the timing properties of different scintillating materials is valuable for tailoring the calorimeter to a specific experimental task and enables fine tuning of the energy and timing response of the device.

Due to the large amount of recorded events it is possible to study the scaling of the time resolution with respect to the deposited energy in the scintillating tile. Therefore, the reconstructed hit energy is binned and only events for which both channels C and E fall into the same bin are accepted. This only applies to about 10% of the taken events. For this analysis, the trigger time is obtained using the constant fraction discrimination to mitigate time walk, while the hit times are obtained with constant threshold discrimination to explicitly retain the time walk effect for subsequent quantification. This is necessary to later disentangle the different effects on the timing performance. This study is motivated by a naive toy Monte Carlo study that reproduced the asymmetric time distribution in Figure 6.6. According to this study, which will not be discussed further, the cause of this asymmetry are low energy signals with only a few detected photons. There are two main sources of asymmetry that are investigated in the following. First, the time walk effect caused by differences in the hit energies (Section 4.3) and secondly, the statistical signal fluctuations of signals with similar energy.

Influence of Time Walk

To investigate the impact of the time walk (TW) correction on the hit time distribution the correction factors have to be obtained. This is done by parameterizing the evolution of the median hit time over the studied hit energy range by an exponential function (Figure 6.8) of the following form:

$$T_{Median} = A + B \cdot e^{\left(CE - D\sqrt{E}\right)} \tag{6.1}$$

The median hit time is chosen because it is known that the distributions are asymmetric and to make sure that the influence of the outlying data points is mitigated. To apply
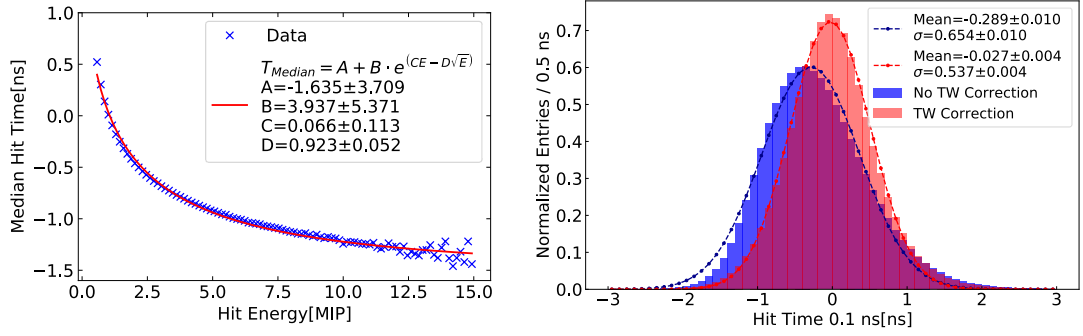
Figure 6.8: Left: An example of the time walk effect in channel C of data set 1. The function parameterizes the evolution of the median hit time and is used to correct the hit times. Right: Comparison of uncorrected (blue) and corrected (red)) hit times. The correction centers the distribution at 0 and decreases its width, the slight mismatch of data and fit on the right flank remains.

the time walk correction, T_{Median} is calculated for every hit and subtracted from its hit time. Figure 6.8 shows a comparison of the hit time distribution in channel C before and after the time walk correction for data set 2. Evidently the mean of the distribution is moved closer to 0 and the overall width is decreased, but the asymmetry still persists in the right tail. This observation applies to all studied data sets.

Influence of Statistical Signal Fluctuations from Photon Counting

For further investigation the events are now binned depending on their hit energies. For the low energy region from 0.5 MIP to 5.1 MIP the bin width is 0.2 MIP, the intermediate region up to 7.5 MIP is binned in 0.5 MIP steps and the energies up to 15.5 MIP are binned in 1 MIP steps. Only events in which both channels C and E are within the same bin get accepted for the subsequent analysis.

In contrast to the previous MIP study, this analysis aims obtaining the time resolution for every bin. This binning ensures that only events with a similar amount of detected photons in both channels are used, therefore the statistical fluctuations from the photon counting are at a comparable level within each bin. This enables an energy resolved, quantitative and qualitative analysis of the timing properties. As a first step, the time distributions in the two signal channels are investigated. Example distributions for four different bins of channel E are shown in Figure 6.9.

It can be seen that the width of these distributions decreases with increasing hit energy, an effect that is caused by the poissonian counting fluctuations. Since the number of detected photons N scales linearly with the hit energy E, the counting uncertainties scale like $\frac{1}{\sqrt{N}} \propto \frac{1}{\sqrt{E}}$. Effectively, this decreases the event-by-event fluctuations of the rising flank of the analog signal at similar amplitudes which also decreases the fluctuations of the reconstructed hit times. Additionally, the skew of the distributions decreases and their shape approaches a normal distribution. Figure 6.10 shows the development of the
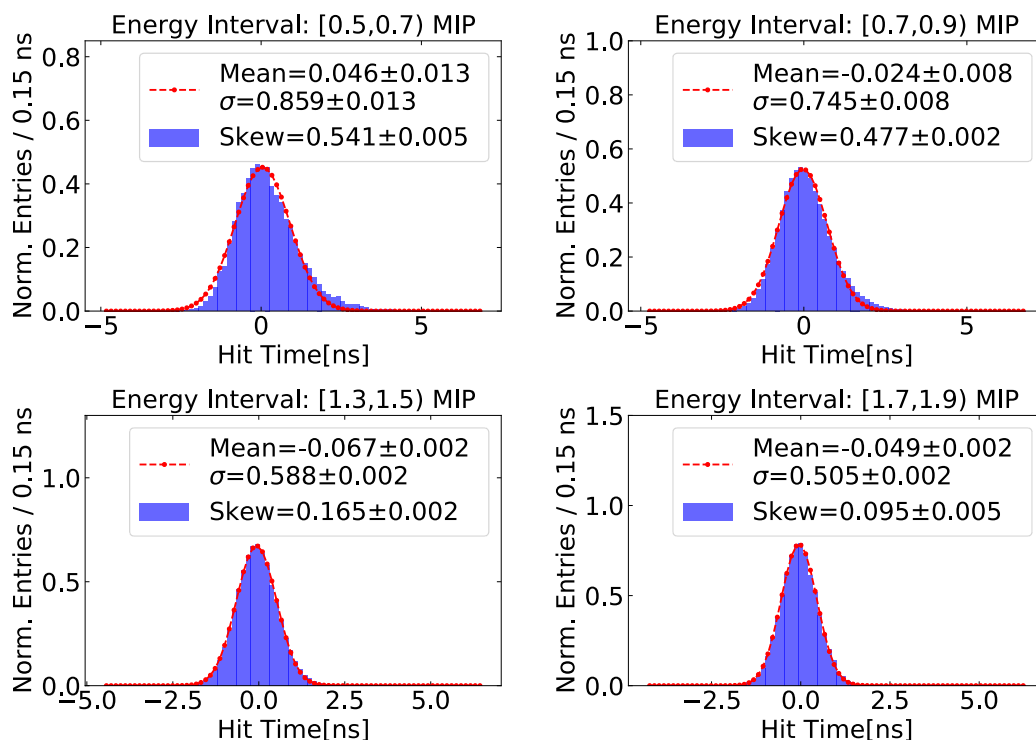
Figure 6.9: Examples of binned hit time distributions of channel E of data set 1. The skew decreases with rising hit energy and the distributions narrow down.

skew of the hit time distribution in channel C for the different data sets. In any case the skew decreases until it approaches a plateau at 0, but data set 4 reaches this plateau earlier than the other data sets. The reason for this is an increased light yield caused by the smaller tile dimensions compared to data sets 1, 2 and 3. This causes the hit times to reach an unskewed normal distribution at ∼1 MIP while for the other data sets this happens at around ∼3 MIP. Since the majority of events have a hit energy around 1 MIP the overall resolution is intrinsically increased. This observation agrees with the significantly increased MIP time resolution of data set 3 shown in the previous section. By calculating the time resolution in the same fashion as for the MIP measurement, but for every bin individually, the energy dependence can be investigated. The results are shown in Figure 6.10 on the right. The evolution is parameterized by

$$\text{Resolution} = \frac{A}{\sqrt{E[MIP]}} \oplus \frac{B}{E[MIP]} \oplus C. \qquad (6.2)$$

In fact, for lower energies the accuracy of the time measurement scales with the poissonian fluctuations of the photon counting, parameterized by A (stochastic term). As these fluctuations decrease with rising energy the resolution approaches a constant value C (constant term) which is mainly influenced by the light emission characteristics of the scintillator and effects introduced by electronics and signal processing. The
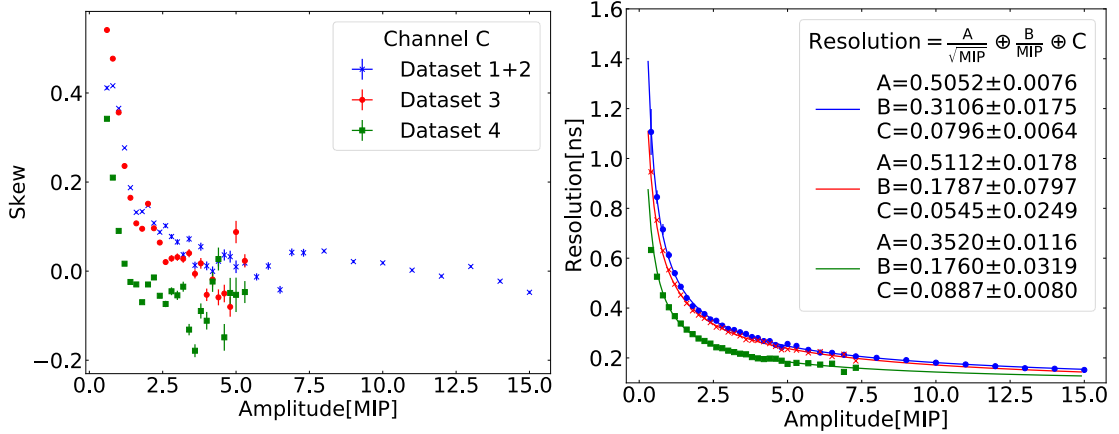
Figure 6.10: Left: Evolution of the skew of the hit time distributions over the studied energy range. Data set 1 and 2 are combined to reach higher hit energies. Right: Energy dependent time resolution. The colors identify the same data sets shown on the left. The legend shows the parametrization and the fitted parameters.

significantly lower stochastic term of data set 4, and thus the overall increased resolution, is caused by the higher light yield which is in agreement with the conclusions drawn from the investigation of the skewed hit time distributions. The constant term is very similar for data set 3 and 4, but differs from data set 1 and 2. A possible reason might be the different scintillator and light emission characteristics, but more data taken with different SiPM-On-Tile configurations are needed to establish a firm conclusion.

In addition to the MIP scale, the energy dependence can also be investigated at the PE scale. In contrast to the MIP calibration it retains information on the number of detected photons per event and is therefore more sensitive to effects introduced by imperfections in the manufacturing and the light collection characteristics of the setup. Furthermore, the different light yield of the tiles does not influence the energy binning, because events are binned according to the number of detected photons only, regardless of the primary energy deposit in the scintillator. Consequently, comparing events of the same energy from different datasets in terms of PE can reveal geometrical contributions to the time resolution.

In this scale, the tail of the hit time distributions towards later times for low energies can be investigated further. This tail is influenced by the asymmetric emission time of the scintillator. If the detected photons from the fast emission are not enough to reach the hit detection threshold, the photons from the slow decay eventually cause the signal to become high enough, but later in time. This explanation is backed by the similar light yield in channel C of dataset 3 and 4(Section 6.4). Due to imperfect wrapping, the number of photons per MIP in channel C of data set 4 is lower than the expected value of around 24 of channel E (see Section 6.4). Nevertheless, the skew in channel C (Figure 6.11) decreases faster for the small tiles in dataset 4. This implies that the

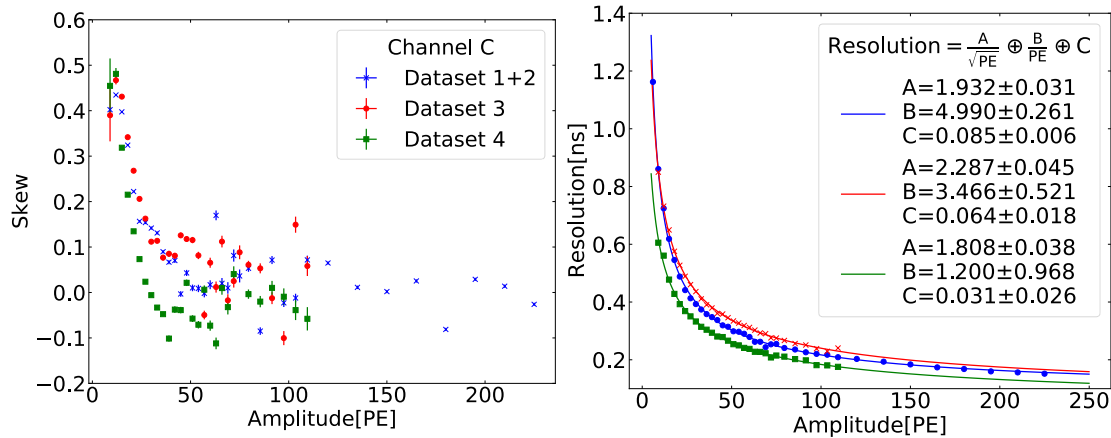| ID	Channel A PE/MIP	Channel C PE/MIP	Channel E PE/MIP	Channel G PE/MIP
1,2	18.8± 0.2	14.4± 0.1	16.2± 0.2	16.6± 0.2
3	25.18± 0.4	22.7± 0.3	19.3± 0.3	23.3± 0.4
4	22.6±0.3	21.8± 0.3	24.0±0.4	18.2± 0.3

Table 6.5: Conversion from PE to MIP.

Figure 6.11: Left: Evolution of the skew of the hit time distributions over the studied energy range in PE. Data set 1 and 2 are combined to reach higher hit energies. Right: Energy dependent time resolution. The colors identify the same data sets as on the left. The legend shows the parametrization and the optimized parameters.

performance is not exclusively influenced by the light yield but also by the geometry of the tile.

Analogous to Figure 6.10 the evolution of the skew and the time resolution in the PE scale are shown in Figure 6.11.

6.5 Lessons Learned

In conclusion, this analysis investigates the timing properties of different scintillators and tile dimensions used for the SiPM-On-Tile configuration. By comparing the MIP time resolution of data set 1 (AHCAL scintillator) with the one obtained with the AHCAL in Section 5.3 one can conclude, that the front-end electronics of the AHCAL contribute about $\sqrt{700^2\text{ps} - 466^2\text{ps}} = 522\,\text{ps}$ to the single channel time resolution of the full prototype. Furthermore, the MIP timing performance depends on the scintillator and the tile dimensions, since both quantities change the light output and thus the number of photons that arrive at the SiPM. The symmetry of the hit time distribution increases with rising energy since a higher number of generated photons decreases the

event-by-event fluctuations. Comparing the energy binned performance in the PE scale for different tile sizes, shows that the evolution of the symmetry and width of the time distribution is not only influenced by the light yield alone. Apparently, also geometric effects play a significant role in the signal generation. Further detailed investigations of this effect are reported in a separate master thesis [75].

Chapter 7

The DUNE Near Detector Gaseous Argon System (ND-GAr)

The second part of the studies conducted in the course of this thesis deal with simulation studies on particle identification for a subsystem of DUNEs near detector, called ND-GAr (see Section 2.3). The systems under study are the electromagnetic calorimeter, based on experience from the CALICE AHCAL(Chapter 4), and the muon identification system. Results presented in the following sections contain time-of-flight reconstruction of the energy of neutrons for a range of assumed time resolutions. The studied range is motivated by the performance of the CALICE AHCAL and standalone measurements of the intrinsic time resolution of the SiPM-on-Tile technology (Chapter 6). Furthermore, a boosted decision tree is implemented to study the separation power of Muons and Pions. The chapter introduces the setup of the simulation, explains the study and its results and concludes with a discussion on the impact of the results on the neutrino oscillation measurements of DUNE.

7.1 The Role of ND-GAr within the DUNE Experiment

The role of ND-GAr within DUNE and the near detector (ND) complex is a high precision, multi-purpose detector tuned to reconstruct the full final state of various neutrino-nucleus interactions and to catch muons that exit ND-LAr unreconstructed. Neutrinos undergo different interactions with matter depending on their momentum as shown in Figure 7.1. DUNEs momentum range spans all three shown channels, while the most probable interactions are resonant (RES) and deep-inelastic (DIS) scattering because the beam momentum peaks at 2.4 GeV. Examples of these are shown in Figure 7.2.

The precise knowledge of the cross-sections of these interactions is immensely important for the neutrino oscillation analysis since the event rates in the far detector have to be extrapolated precisely from the near detector data. The uncertainties, both statistical and systematical, present in todays modeling of this momentum region have to be mitigated. Especially in deep-inelastic scattering the multi-hadron final states are governed by complicated nuclear processes, hence resolving the full set of particles is vital to increase the precision of these models. The low density of the magnetized gaseous Time Projection Chamber (TPC), that forms the central detector of ND-GAr and serves as the neutrino target, allows even the low momentum particles to travel a significant distance from the interaction vertex in order to be resolved. Neutral final states are impossible to
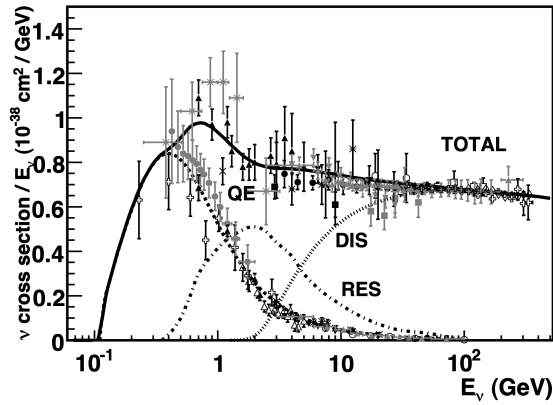
Figure 7.1: Charged current cross-section per nucleon of neutrinos normalized to their energy. The spectrum changes from being dominated by quasi-elastic (QE) interactions to an intermediate region driven by nuclear resonances (RES). Towards high energies the cross-section increases linearly and the most probable interactions are deep-inelastic (DIS). The broadband beam of DUNE peaks at 2.4 GeV but spans all three regions of the spectrum. Taken from [76].
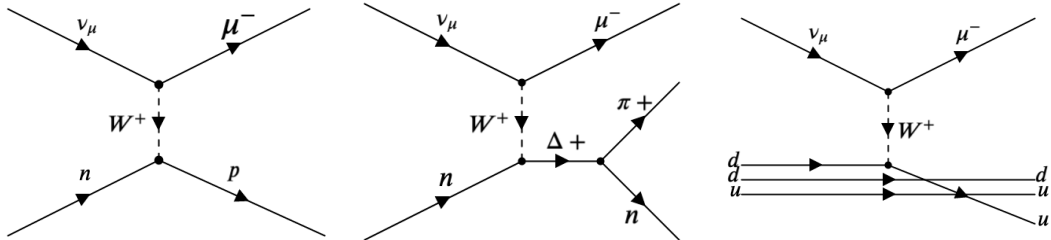

Figure 7.2: Left: Quasi-elastic charged current neutrino interaction. Depending on the momentum transfer the produced proton is knocked out of the target nucleus and can be resolved in the TPC. Middle: Resonant charged-current neutrino interaction producing a pion and a neutron via the excitation of a positive delta resonance. Right: Deep-inelastic charged-current neutrino interaction. The neutrino transfers a significant amount of momentum to a quark inside a neutron. Depending on the detailed kinematics, this interaction can produce a multi-hadron final state by intra-nuclear reactions and hadronization. Both interactions are also possible in anti-neutrino mode, but are helicity suppressed by a factor of 3 [76].

reconstruct in a detector relying on ionization for signal generation, so the TPC is surrounded by a calorimeter. To increase the particle separation capability an additional muon identification system is embedded in the return yoke of the magnet. ND-GAr also has an ancillary BSM physics program like searching for neutrino tridents or heavy neutral leptons, further reading can be found in [39]. A detailed detector description is provided in the next section.

Detector Setup

Its innermost system, a TPC of about 5 m diameter, is filled with gaseous argon serving as neutrino target. The gas is pressurized to 10 bar to increase the target mass and therefore the event rate. Due to the low density the TPC offers a low detection threshold and a long range of the charged final state particles. Precise momentum reconstruction is achieved with a 0.5 T solenoidal magnetic field normal to the beam direction. Since the neutral final state particles like photons and neutrons are invisible to the TPC, its volume is surrounded by a highly granular calorimeter housed inside the pressure containment vessel. The barrel and end cap calorimeter both consist of 42 layers of alternating lead absorber plates and plastic scintillator. The first 8 layers consist of 0.7 mm lead absorber followed by 5 mm thick scintillating plastic tiles with an area of $25{\times}25\,\text{mm}^2$ to achieve spatial resolution. The segmentation enables direction reconstruction of photons by sampling the longitudinal evolution of electromagnetic cascades and aids the assignment of TPC tracks to energy depositions in the calorimeter. The following 34 layers consist of 1.4 mm lead absorber followed by 10 mm thick scintillator. In these layers, the active volume is segmented into crossed strips spanning the full width of the calorimeter to achieve three dimensional position resolution within one layer. Inspired by the CALICE AHCAL (Chapter 4) tiles and strips are read out by Silicon Photomultipliers embedded in the detector. The initial concept and first optimizations of this calorimeter have already been studied as part of the master thesis of the author of this work, further information can be found in [40] [77]. TPC and calorimeter are surrounded by four super-conducting magnet coils which generate a solenoid field of 0.5 T. The cryostat of the magnet system is surrounded by a return yoke containing a muon identification system (MuID). To accommodate the MuID the yoke is segmented into three layers of 5 cm thick iron plates followed by crossed scintillator strips with a total thickness of 1.67 cm. A cross-section of the detector is shown in Figure 7.3.

7.2 Simulation Setup and Data Generation

The detector setup for ND-GAr is parameterized in a GDML (Geometry Description Markup Language) file specifying the detectors location to place it correctly in the neutrino beam, as well as the dimensions, materials and placements of the sub-components. The generation of Monte Carlo data samples and basic reconstruction is implemented in the *art* event processing framework developed at Fermilab [79]. It is a collection of libraries written in object oriented C++ that invoke user-specified *modules* to perform event
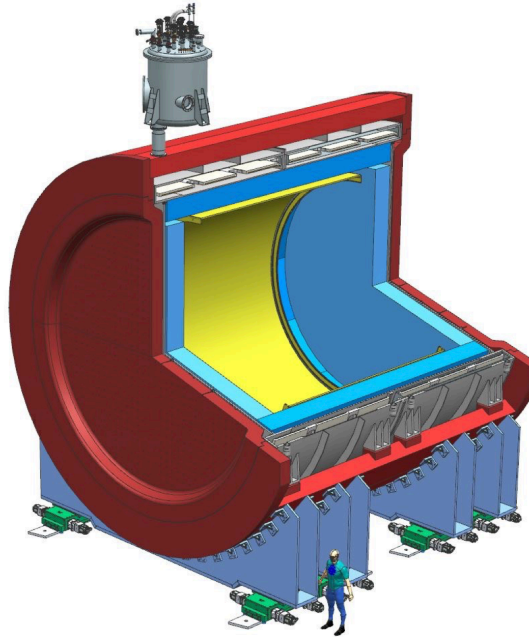
Figure 7.3: The ND-GAr detector. The central yellow volume shows the gaseous argon TPC, surrounded by the calorimeter in blue and the magnet coils and cryostat in grey. The return yoke shown in red contains the muon identification system. Taken from [78].

simulation, digitization, reconstruction, filtering, analysis and data output. Additionally, the framework allows the usage of *services* to communicate between the modules. The program flow is defined by *FHiCL* files which list the needed modules and services for any step and define analysis specific input parameters. The detector model and *art* program flow for this analysis is explained in the following.

Event Generation and Tracking

In the first step of event generation the responsible art module parses the GDML file containing the detectors description and chooses the event generator. Two generators are used for the studies in this chapter, the first and most basic one is a simple particle gun which allows the specification of a set of primary particles with specific origin, momentum and direction inside the detector volume. These properties can be fixed or drawn from a uniform or gaussian distribution to simulate more realistic scenarios. The second option is a neutrino event generator called GENIE3 [80]. This generator uses the parameterized neutrino beam parameters and most recent interaction models as input to generate the final state particles of a neutrino interaction with an argon nucleus. Subsequently, GENIE calculates the kinematic and intra-nuclear processes and generates a list of secondary particles and their properties, similar to the set of final state particles a real neutrino interaction would create inside the detector. The information produced by any event

generator is then passed on to GEANT4 (GEometry ANd Tracking) [67][81][82], a toolkit to track particles as they traverse the detector volume. By providing a physics list that parameterizes physical processes, it calculates the interactions of the tracked particles with the detector volume like ionization, but also more complex processes like inelastic scattering and decays producing secondary particles. Additionally, the deflection of charged particles in the magnetic field is accounted for. The most important information produced by GEANT4 is the location and amount of energy the tracked particles deposit in the different parts of the detector. To be able to accurately calculate these energy losses, GEANT4 also requires the definition of materials the detector components are made of. After the tracking is completed and all particles are either stopped inside or have exited the detector volume, an output stream is generated. It contains the information on the deposited energy in GeV as well as the *Monte Carlo truth* including the particles and processes responsible for this deposition. The output of the GEANT4 module is then passed on to the first step in the reconstruction flow, the digitization.

Digitization

The digitization parses information from GEANT4 and translates it into data resembling the response of the different detector systems. In case of the calorimeter the positions and time of energy depositions in the scintillator are assigned to the readout channels depending on their position. All depositions falling within the area of one channel are summed up and detector related effects are added to it. To model the response of the Silicon Photomultiplier (SiPM) the constants implemented in this simulation are taken from previous experience with the CALICE AHCAL. The energy deposition in the respective channel is converted from GeV to MIP by a conversion factor of $0.814\,\mathrm{MeV\,MIP^{-1}}$, and subsequently from MIP to the unsaturated number of fired pixels of the SiPM by a conversion factor of $20\,\mathrm{Pixel\,MIP^{-1}}$. The saturation effect of the SiPM is parameterized by

$$\text{Saturated Number of Pixels} = \text{Effective Pixels} \cdot \left(1 - e^{-\frac{\text{Unsaturated Pixels}}{\text{Effective Pixels}}}\right), \qquad (7.1)$$

with Effective Pixels = 3000. The number of saturated pixels is smeared by a binomial distribution to account for the statistical nature of the photon counting and another gaussian smearing with a width of $0.4\,\mathrm{Pixel}$ accounts for electronic noise. The resulting number of fired pixels is converted to Analog-to-Digital Converter units (ADC) by multiplication with a gain factor of $15\,\mathrm{ADC\,Pixel^{-1}}$. A gaussian smearing with a default width of $700\,\mathrm{ps}$, inspired by the AHCAL, is applied to the time stamp of the energy deposition to simulate the time resolution of the system. The digitized values are then added to an output stream and transferred to the reconstruction step.

Reconstruction

The reconstruction step translates the simulated electronic response from the digitization to a format that is used to perform meaningful data analysis. It can be compared to the

data acquisition and event building software of a real experiment. The scale of calorimeter energy deposits (Hits) is converted to GeV and the position of the Hits is transformed from channel number encoding to a Cartesian coordinate system that has its origin at the center of the detector. The hits are sorted in categories depending on the subsystem they are created in (ECAL, MuID or TPC). Additionally, clustering algorithms can be applied if the user chooses and the charged tracks in the TPC are associated to the energy depositions in the ECAL, if the particle deposits energy in both systems.

Analysis and Output

The analysis module is the most modular one in the data flow. It can be used to only write the data from the reconstruction step to a file, but also for involved, user specific analysis tasks. For the studies explained in the following sections, the information is written to a file format called ROOT [83], used by a data analysis framework developed at CERN for use in high energy particle physics. The analyses are implemented as standalone projects written in Python.

Chapter 8

Neutron Kinetic Energy by Time of Flight

A major drawback of a TPC is the inability to reconstruct neutral particles if they traverse the fiducial volume without an inelastic interaction. It is the task of the calorimeter to detect neutrons and photons produced in association with a neutrino interaction on argon within the TPC. Since most of these neutrons are relatively low energetic they rarely develop a particle shower in the calorimeter, but cause isolated hits by knock-on protons or de-excitation from struck nuclei. Since these reactions lead to a large fraction of invisible energy the time-of-flight (TOF) technique provides a way to reconstruct the total kinetic energy and is (to first order) independent of the energy containment in the calorimeter. This chapter introduces the analysis strategy and reports the performance of the detector.

8.1 Time-of-Flight Technique and Detector Requirements

In order to identify the detector parameters that drive the TOF energy resolution the measurement principle has to be understood. In most neutron events the particle does not deposit the full energy in the calorimeter, but scatters of a nucleus with comparably small energy transfer. Compared to electromagnetically interacting particles like photons, the correlation between visible and true energy is very weak. Therefore, the unfeasible calorimetric measurement of summing up the energy depositions belonging to one particle is substituted by a time and distance measurement from the neutrino interaction vertex to the neutron interaction in the calorimeter. The mathematical formula for the kinetic energy of relativistic neutrons by TOF reads as follows:

$$\mathrm{E_{TOF}[GeV]} = \mathrm{m_n[GeV]} \cdot \frac{1}{\sqrt{1 - \left(\frac{\mathrm{d[cm]}}{\mathrm{c[\frac{cm}{ns}] \cdot t_{TOF}[ns]}} \right)^2}} - \mathrm{m_n[GeV]} \tag{8.1}$$

Here $\mathrm{m_n}$ represents the rest mass of the neutron, c is the speed of light, d $= \|\boldsymbol{P_{Vertex}} - \boldsymbol{P_{Hit}}\|$ is the measured distance between the vertex and the neutrino interaction in the calorimeter and $\mathrm{t_{TOF}} = \mathrm{t_{Hit}} - \mathrm{t_{Vertex}}$ is the time it takes the neutron to traverse this distance. Since d and t are differences of observables obtained with two individual detectors, the TPC and the calorimeter, position and time resolution of of both detectors are equally important. The timing capability of a standalone TPC is negligible compared to modern calorimeters that can reliably achieve resolutions on the

order of 100 ps so alternatives have to be implemented in order to precisely determine t_{Vertex}. Possible solutions include the detection of fast scintillation light of the gaseous argon with photon detectors inside the gas volume, or the extrapolation of the time of a relativistic charged track from the calorimeter to the vertex. Using the latter requires a charged particle in the final state that reaches the calorimeter, as well as successful particle identification and momentum measurement, since the speed of particles cannot always be assumed to be close to the speed of light. Consequently, the particles mass matters. Therefore, this method substitutes the limited time resolution of the TPC with the superior position and momentum resolution of the TPC and the time resolution of the calorimeter. In this case, the time of the vertex is defined as

$$t_{\text{Vertex}} = t_{\text{Track}} - \frac{d}{v}, \text{ with } v = \sqrt{\frac{p^2/m^2}{1 + \frac{p^2/m^2}{c^2}}}. \tag{8.2}$$

Using gaussian errors and assuming a muon track (m=0.105 GeV) with a length of d=250 cm and momentum of p=1 GeV, a TPC momentum resolution of 1%, a position resolution of 1 mm in TPC and calorimeter and a time resolution of the calorimeter of 247 ps[1], the error on t_{Vertex} is 247 ps. This shows that, in the given case, the driving parameter is the time resolution of the calorimeter. This value is used for the simulation study discussed in the following sections. Different approaches to obtain the time of the vertex are currently under study and will not be covered in this thesis.

8.2 Properties of Neutrons from Neutrino Interactions

The striking difference between neutrons originating from high energy collisions in a particle accelerator and neutrons produced inside ND-GAr is their momentum distribution. In the range of 10 GeV to 100 GeV neutrons will in most cases produce distinctive hadronic showers in the calorimeters, but in the case of DUNE about 90% of the neutrons are below 1.2 GeV as shown in Figure 8.1 on the left. Another difference arising from the fixed target nature of DUNE is the direction along which the neutrons are emerging from the interaction vertex. Depending on the fraction of momentum the neutron carries from the neutrino interaction they get more or less boosted in downstream direction, along the neutrino beam, as shown in Figure 8.1 on the right.
This plot shows that the majority of the particles, also the ones with a lower momentum, are emitted within 50° around the beam axis. A significant tail still exists towards larger angles, even along the upstream direction, which supports the design choice of the calorimeter surrounding the TPC, but also motivates an asymmetric design that increases the depth and possibly also the capability of the system in downstream direction. This however heavily depends on the available funding and space constraints on the full ND-GAr system and is not covered by the studies presented here.

---

[1]The single channel time resolution for MIPs of the AHCAL is 700 ps. Assuming a muon creates on average 1 hit in every highly granular layer of the calorimeter of ND-GAr, the resulting time resolution is $700\text{ps}/\sqrt{8} = 247\text{ps}$
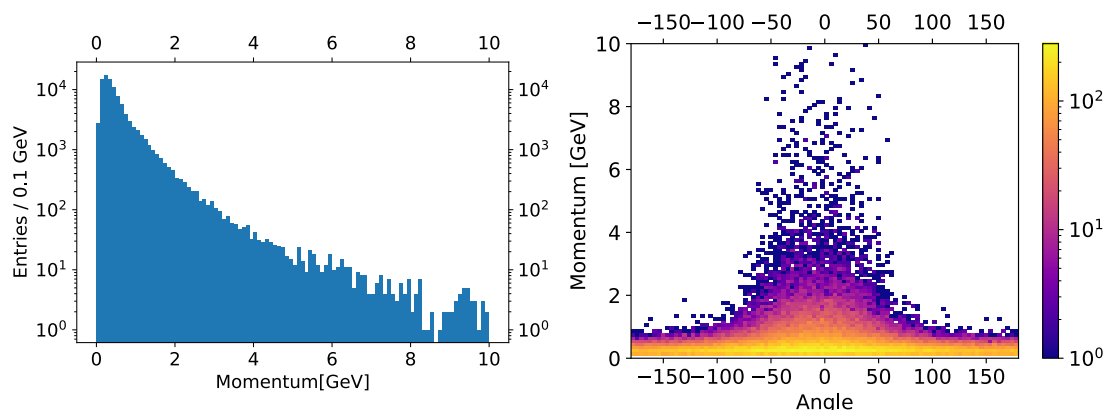
Figure 8.1: Left: Momentum distribution of the neutrons as produced by the GENIE event generator on Argon nuclei. About 90% of the events are accumulated below 2 GeV with a most probable value at 0.35 GeV. Right: Angular distribution of the neutron momentum direction with respect to the beam axis. The majority of particles is emitted within 50° around the nominal beam direction. At low momentum, the entire solid angle is covered.

8.3 Data Samples and Quality Cuts

This study uses two Monte Carlo data samples of pure neutrons in the TPC, one is generated with GENIE and represents the neutron momentum spectrum and vertex distribution produced in neutrino interactions (left side of Figure 8.1). Another one is generated with a particle gun placed at the center of the TPC with discrete energy steps of 100 MeV in the range of 50 MeV to 2.05 GeV and 10000 events per step. The samples are generated with a perfect time resolution to study the general functionality of the method with less distortions to the data, a realistic parametrization of the time resolution shown in Section 6.4 is implemented in the analysis code. Furthermore, only neutrons with the first interaction in the calorimeter are selected from the sample, because the time-of-flight measurement gets distorted if the neutron did not travel in a straight line to the first hit in the calorimeter. In reality, neutrons interacting in the TPC can be resolved if charged particles are produced but neutrons penetrating the calorimeter will be missed. The impact of this selection on the discrete data set is shown in Figure 8.2, along with the fraction of remaining events split into elastic and inelastic interactions. Due to the broad momentum range the nature of possible interactions changes. While most of the neutrons around 50 MeV undergo elastic interactions in the calorimeter, the ratio quickly changes with increasing momentum until inelastic interactions dominate. The cut rejects about 15% to 20%. In a realistic application, the neutrons reaching the calorimeter have to be correctly classified to in order to reconstruct the kinetic energy. The currently used identification [39] reaches an efficiency of about 45% and a sample purity of 40% in neutrino mode and 55% in anti-neutrino mode. Since this is only a multiplicative factor, it is no included in the study presented below.
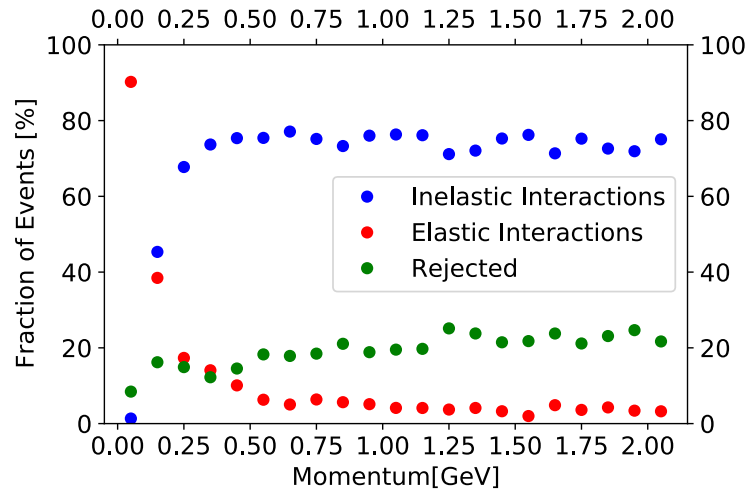
Figure 8.2: This figure shows the fraction of inelastic (blue) and elastic (red) interactions in the detector. Only events that undergo their first interaction in the calorimeter are considered. The green points show the fraction of neutrons that undergo the first interaction outside of the calorimeter.

8.4 Energy Reconstruction

In case of more than one hit associated to a neutron, the first hit in the collection is used to define the time of flight. Since the clustering in the used software framework is still under heavy development the time of the full neutron hit cluster cannot be used. It is also questionable if this would increase the effective time resolution, since processes like neutron evaporation and de-excitation lead to low hit energies in the adjacent channels, typically below 1 MIP as shown in Figure 8.3, and deteriorate the time resolution.

In the following section the performance of the reconstruction is first investigated with the discrete data set, to compare perfect time resolution with the parametrization following Section 6.4 and to study the scaling of the energy response with momentum. The second part reports the achievable energy resolution of the GENIE data set.

Discrete Data Set

For this data set, the energy is reconstructed individually for every momentum step according to the procedure described previously. To compare the impact of finite time resolutions of the detectors the performance is calculated first for the reconstructed data with perfect time resolution, second including the time resolution of the calorimeter and third including the time resolution of both calorimeter and vertex. Figure 8.4 shows examples of the resulting distributions for a momentum of 0.75 GeV and 1.75 GeV. The distribution with perfect time resolution shows a sharp peak at the true energy of the neutrons of about 0.27 GeV and 1.05 GeV and a slight tail towards lower energy. This tail is caused by events that undergo an elastic interaction in the calorimeter without depositing
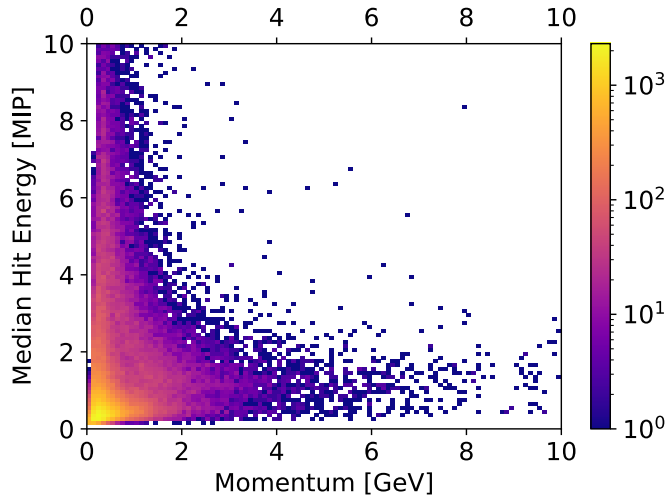
Figure 8.3: This histogram shows the median hit energy per event up to a particle momentum of 10 GeV. The vast majority of events are contained below 1 MIP which implies, that the time resolution for the majority of the events is below the MIP time resolution quoted in Section 5.3 and Section 6.3.

energy, enter the cryostat where they produce secondaries in an inelastic interaction that propagate back into the deeper layers of the calorimeter. This causes the measured time of flight to be significantly longer than the expectation obtained by measuring the distance from vertex to the calorimeter hit, thus resulting in a deficit of reconstructed energy. Including the calorimeter time resolution and the previously discussed vertex time resolution the distribution broadens as expected. In these scenarios the reconstruction can also fail for up to 25% of the events for the highest momentum, because the time smearing can lead to a negative argument of the square root in Equation (9.9).
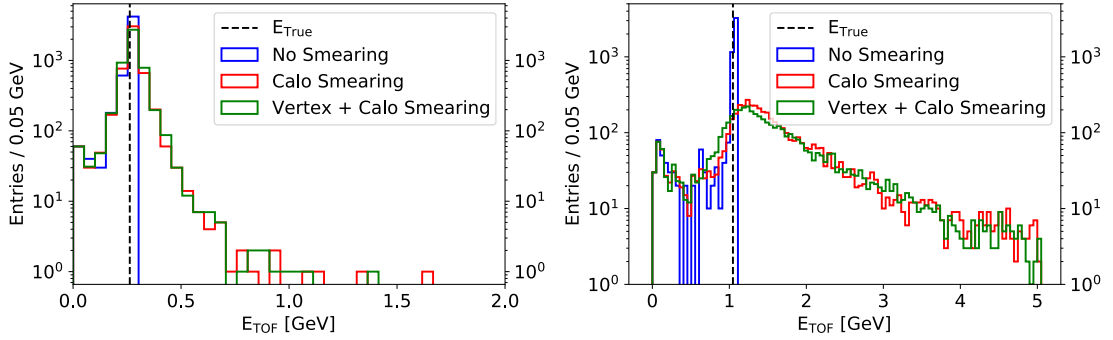
Figure 8.4: Reconstructed energy for different contributions to the time resolution. The left histogram shows distributions for a momentum of 0.75 GeV (a kinetic energy of 0.27 GeV), the right one for a momentum of 1.75 GeV (a kinetic energy of 1.05 GeV) . The blue histogram shows the performance without time smearing, red shows the impact of only the time smearing in the calorimeter and green shows the combined effect of the vertex and calorimeter time resolution. The tail to low energy is caused by particles that back scatter from the cryostat and return yoke.

Since the distribution of the reconstructed energy features pronounced and asymmetric tails as shown in Figure 8.4, a simple gaussian description is not suited to quote results. To reduce the impact of these tails on the quoted reconstructed energy and energy resolution, the median and its standard error are computed by a bootstrap method. First, a kernel density estimator is used to obtain a smooth representation of the underlying distribution. From this representation, 100 distributions with 10000 samples each are drawn and their medians are calculated. The mean and variance of the resulting 100 medians are used to quote the median reconstructed energy and its error. The width of the distribution is described by the standard deviation of the smallest interval containing 90% of the entries (STD_{90}) along with the standard error of the standard deviation for large data samples [84]. Figure 8.5 shows the performance of the reconstruction for every momentum step. To increase the interpret ability of the figures, the reconstructed energy is not compared to the true momentum, but the true kinetic energy instead.

This figure shows the reconstructed energy (Median E_{TOF}) versus the true energy for the three time resolution scenarios. To illustrate the very good intrinsic linearity of the procedure with perfect time resolution a linear function is fitted to the data points. It is also free of constant offsets since the function extrapolates back to the origin. Adding the smearing leads to increasing deviations from linearity that become significant at 0.4 GeV. The lower part of Figure 8.5 shows the fractional deviation of the median reconstructed energy from the true energy and shows a similar behavior. As the neutrons get more relativistic, the correlation between time of flight and true momentum gets weaker because of the relativistic relation of particle momentum and velocity. Slight distortions in the measurement of the time of flight have an increasingly severe impact on the energy measurement and since the technique does not allow negative reconstructed energies, the median gets biased towards higher energies. Since this resolution, in contrast
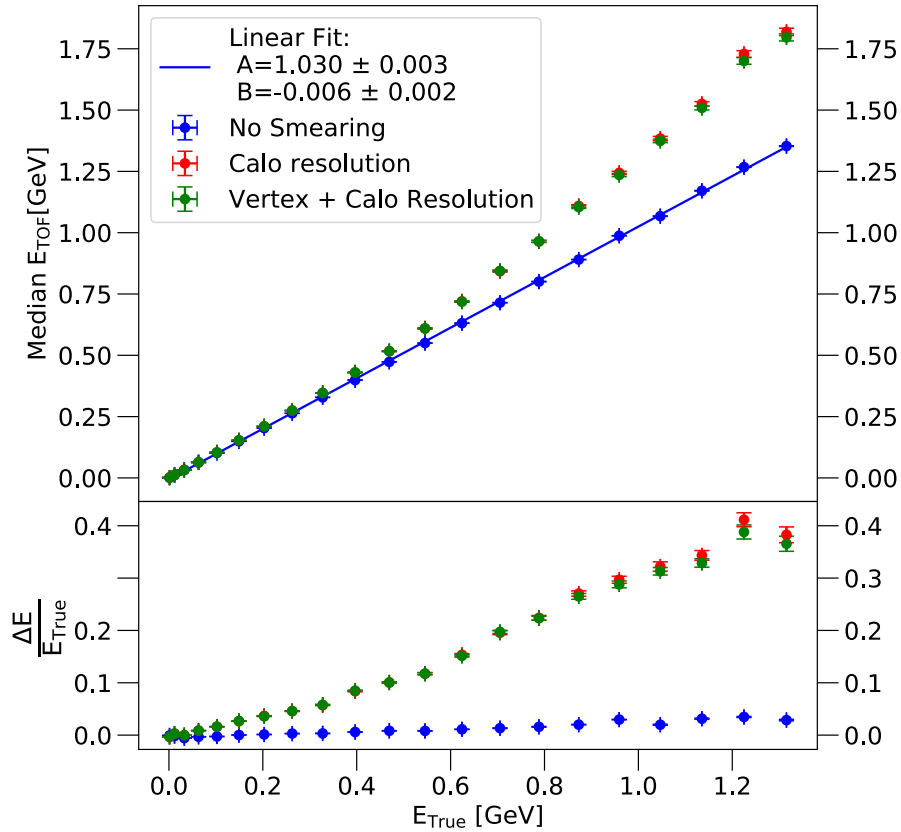
Figure 8.5: The upper part of the plot shows the median of the reconstructed energy versus the true energy. The blue data points show the performance without time smearing, red shows the impact of only the time smearing in the calorimeter and green shows the combined effect of the vertex and calorimeter time resolution. For illustration of the linearity of the TOF method, a linear function is fitted to the blue data points. The lower part shows the fractional deviation of the median reconstructed energy from the true energy.
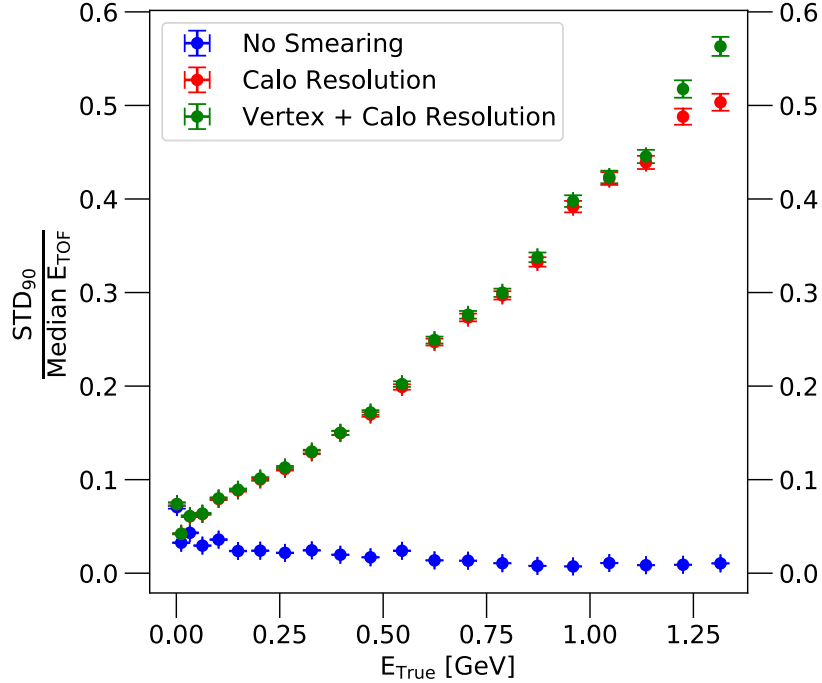
Figure 8.6: Resolution of the TOF reconstruction parameterized by the ratio of STD_{90} and median reconstructed energy. A value of 0.1 corresponds to 10%.

to the calorimeter resolution, only changes the time-of-flight but not the actual distance from the vertex to the calorimeter hit, it creates artificially slower particles in some cases. The energy resolution shown in Figure 8.6 is parameterized by the ratio of the (STD_{90}) and the median of the reconstructed energy. As expected, the best resolution is achieved at low energy because the correlation of velocity and kinetic energy is still strong, so minor distortions on an already large time of flight don't have a severe impact. Increasing the energy however, quickly reduces the resolution, because not only the width of the distribution increases but also the median deviates from the true energy as shown in the left plot. This behavior however is a natural consequence of the theory of relativity and any detector system with finite time resolution will loose performance with increasing relativity of the particles.

While this numbers might be discouraging, one hast keep in mind that the majority of the neutrons produced in the detector have a momentum around $0.35\,\mathrm{GeV}$, corresponding to a kinetic energy of $0.06\,\mathrm{GeV}$, and the relativistic effects are moderate. The performance on the realistic data set generated with GENIE is investigated in the next chapter.

GENIE Data Set

The events in this data set are selected and reconstructed in the same way as described for the discrete data set. The neutrons are generated throughout the fiducial volume of
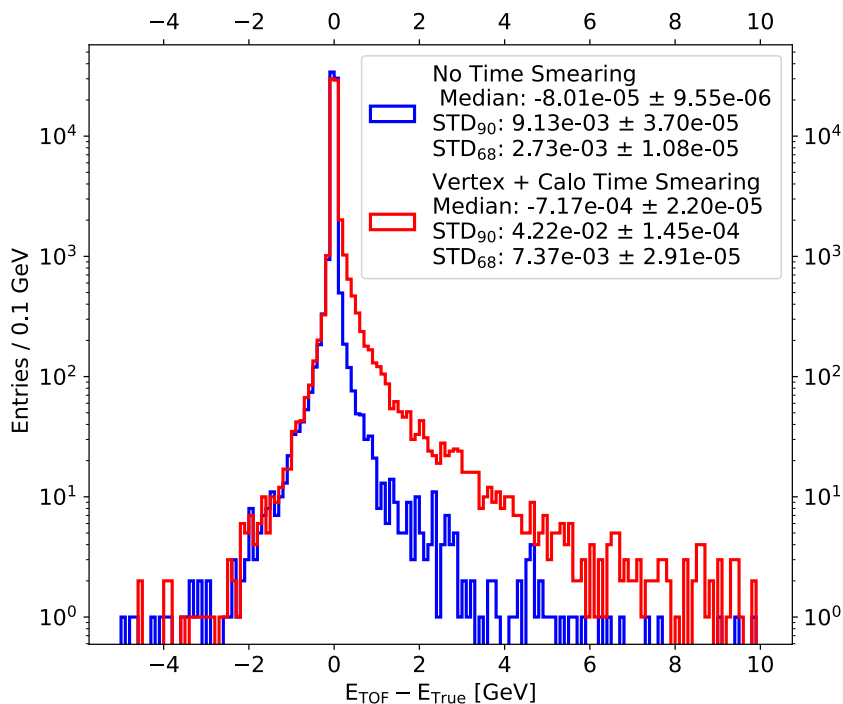
Figure 8.7: Performance of the TOF reconstruction for the GENIE Data Set. The blue histogram shows the difference of reconstructed and true kinetic energy for perfect time resolution and features a rather symmetric distribution. The red histogram includes the time resolution of vertex end calorimeter. This distribution is asymmetric with a tendency of an excess in reconstructed energy.

the TPC and the momentum distribution follows the ones shown in Figure 8.1. Both the time resolution of the ECAL and the vertex are simulated. From the 100000 initially generated events, 67677 remain after event selection and data quality cuts. The resulting distribution of the difference between true and reconstructed energy, shown in Figure 8.7 , features a sharp peak around zero with a median at -0.00072±0.000 02 GeV. Due to the asymmetric tails the width is again quoted as the standard deviation of the 68% and 90% smallest interval and has a value of 0.00737±0.000 03 GeV and 0.0422±0.0001 GeV respectively.

The pronounced tail towards positive entries is caused by the limited time resolution for low energy hits in the calorimeter caused by neutrons with low momentum. Since faster than light neutrons are not allowed, the possible values are limited to $E_{True} - E_{TOF} = E_{True}$ which can be see in the cutoff in Figure 8.8. These histograms show the difference of reconstructed and true energy with and without simulated time resolution. A comparison shows, that the cutoff at zero reconstructed energy is equally pronounced in both scenarios,
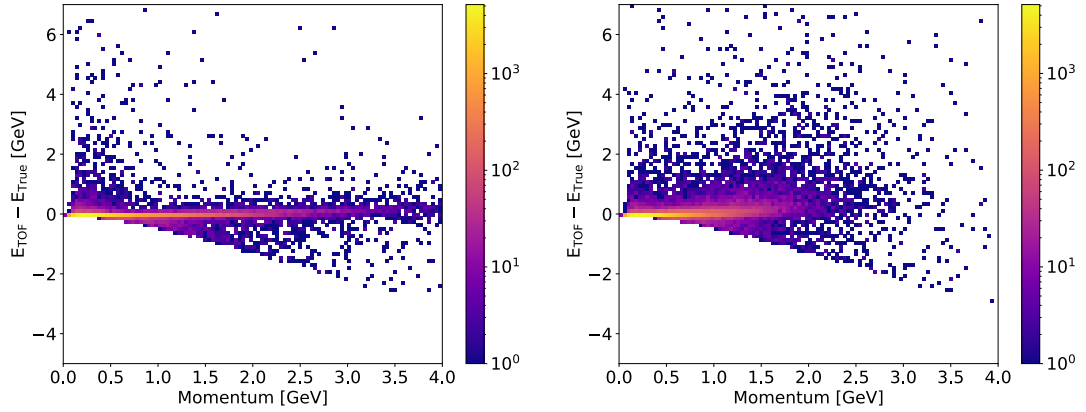
Figure 8.8: Left: Distribution of the difference of true energy and reconstructed energy versus neutron momentum. The time smearing is not included and the data corresponds to the blue histogram in Figure 8.7. Right: Distribution of the difference of true energy and reconstructed energy versus neutron momentum. This histogram includes time smearing and corresponds to the red histogram in Figure 8.7.

while the time smearing primarily causes a tail towards an excess of reconstructed energy. For low momentum, thus low kinetic energy, this leads to an asymmetric tail because Equation (9.9) becomes invalid if the measured distance and time of flight would lead to a neutron that is faster than light. Since these events fail the reconstruction, they do not enter into this histogram, thus promoting the asymmetry. Increasing the momentum reduces the tail but the overall distribution is widened, corresponding to the deterioration in energy resolution already seen in the previous section for the discrete data set.

8.5 Lessons Learned

The two driving factors that influence the TOF performance are the time resolution of the calorimeter and the vertex and, depending on the reconstruction, they are related as explained before. The vertex resolution of 247 ps, derived from the time resolution for minimum ionizing particles of the AHCAL, only has a minor impact on the resolution. As shown with the discrete data set, the limited time resolution of single channels with low energy deposition dominate the high energy performance of the reconstruction. This resolution is mainly driven by the processes happening in the scintillator before the photons get detected. At this point it is a matter of optimization, since the majority of the neutrons produced in ND-GAr have low energy. This is also reflected in the resolution of the GENIE data set of 42 MeV (STD_{90}). Increasing the time resolution for neutrons in a calorimeter is not an easy task, because they do not interact in a specific region of the detector. While highly sensitive timing layers at the beginning of the calorimeter are beneficial for charged particles and photons, they are also expensive. Equipping a

full calorimeter with this technology might not be within the allocated budget. Another possibility to increase the neutron performance is an increased plastic scintillator content in the calorimeter, since neutrons primarily interact with the light nuclei. On the contrary, this also increases the overall size of the calorimeter which is already at the limit of available space. In conclusion, the most straight forward way to increase the high energy performance is the implementation of sensitive timing, especially focusing on the low energy performance of the scintillator. A redundant way to determine the vertex time is also beneficial, since the calorimeter can only extrapolate this time if a charged particle reaches it, which is, e.g. in neutral current interactions, not necessarily the case.

An accurate neutron reconstruction is vital to quantify the relation between true and reconstructable energy of neutrino interactions on argon nuclei. This reduces systematic uncertainties in the far detectors energy reconstruction and aids the neutrino oscillation measurements. Since deep inelastic events potentially produce multiple neutrons in the hard scattering and subsequent nuclear reactions, an estimate of the neutron multiplicity is used to reduce misidentification of neutral particles like photons and neutrons in the liquid argon detectors. For the measurements conducted with ND-GAr correct neutron reconstruction also enhances the determination of the neutral pion spectrum, since they are a background source for the photon reconstruction.

Chapter 9

Multivariate Separation of Muons and Pions

The analysis presented in this section aims on establishing the expected performance of ND-GAr in separating muons and charged pions produced in neutrino interactions. Usually, the central drift chamber is used to identify particles based on their energy loss as they traverse the drift volume, an approach that relies on different masses of the particles in question. The mass difference of muons and pions is only 34 MeV and separation is only possible up to a particle momentum of ~ 250 MeV [39] in the current configuration of the gaseous argon TPC. This chapter studies the separation of muons and pions withe the calorimeter and muon identification (MuID) system. It motivates the analysis, describes the Boosted Decision Tree (BDT) classifier and reports on the performance.

9.1 The Need for Separation of Muons and Pions

In order to identify the nature of the neutrino reaction and to reconstruct its total momentum it is vital to identify the full final state. In resonant charged current (CC) muon-neutrino interactions for example, which contribute 25% to the total event rate [39], muons and pions are produced alongside as shown in Figure 9.1. Although most of the momentum in a typical reaction will be carried by the muon the risk of confusion rises with increasing neutrino momentum since the particle separation and momentum resolution performance of the TPC decreases. This directly impacts the flux predictions for the far detector and the systematics of the cross-section measurement. Also a false association of charge and particle species leads to a mistake in reconstructing the neutrino flavor and type and thus to errors in the estimation of the beam contamination. Furthermore, since ND-GAr is designed to be a high precision machine, the correct identification of neutral current events producing a charged pion is important to constrain the errors on cross-sections. Since a significant number of events will also be deep-inelastic and produce a multitude of final states including charged pions, it is essential to identify the corresponding muon in order to improve the interaction model at higher energies.

Since muons and pions are not the same particle species the accessible interactions in dense material like the absorbers of the calorimeter or the return yoke of the magnet, which houses the muon detector, are different. This can be exploited to separate them using the two systems. While most of the particles, especially the ones with lower momentum, will stop in the calorimeter, a considerable fraction of muons and pions will
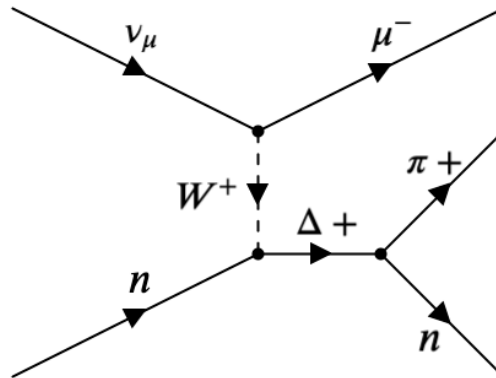
Figure 9.1: A tree level diagram of resonant pion production. A muon neutrino interacts with a neutron of the target nucleus and excites a Δ baryon. Its decay produces a pion and a neutron alongside the corresponding muon of the charged current interaction, so it is vital to correctly associate the charge to the particle to identify the type of primary neutrino.

traverse it without interacting and leave only a minimum ionizing track making them inseparable. Since the return yoke is much more dense compared to the calorimeter, the chance for pions to interact hadronically is increased. Muons cannot interact in this way so the most probable interaction is still ionization and the muon will likely traverse the MuID as well, so pions and muons can be distinguished.

9.2 Simulation Samples

To train the BDT several data sets are generated. The GENIE event generator is used to generate a labeled set of muons and a set of pions for training, as well as a labeled data set that contains both muons and pions. By using GENIE the momentum distribution of the final state particles is directly computed from the estimated neutrino beam spectrum and therefore resembles a realistic scenario. Furthermore, the relative amount of created muons and pions is intrinsically reproduced from the currently known input cross-sections to the event generator and amounts to 86% muons and 14% pions. Additional equally sized data sets of muons and pions are produced with a particle gun in a momentum range of 250 MeV to 5 GeV in 50 MeV steps with a flat momentum distribution. They are used to investigate the bare performance of the BDT without the underlying realistic momentum distribution and relative particle rates. Regardless of the data set, only particles that start inside the volume of the TPC and create at least one hit in the calorimeter are considered, particles decaying in the TPC are rejected. The percentage of decaying particles is shown in Figure 9.3 on the left. The amount of decaying muons is negligible, but about 13% of the pions at low momentum decay because their lifetime is two orders of magnitude shorter than the muon lifetime. After rejection the normalized
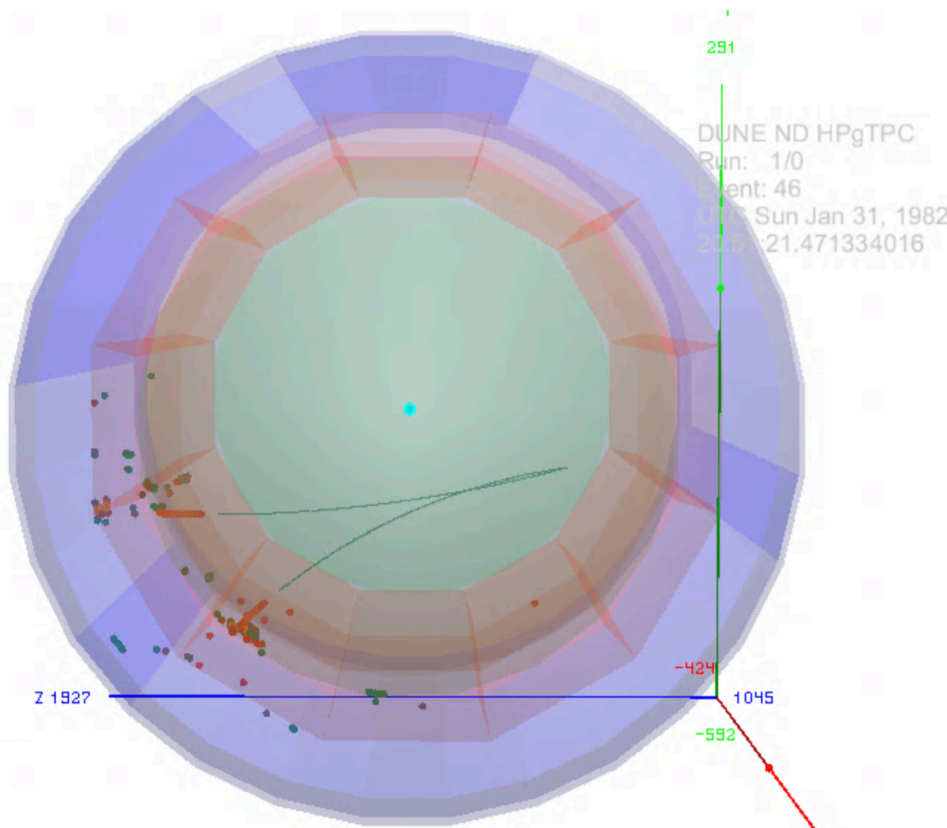
Figure 9.2: A typical event display of charged current resonant muon and pion production. In the TPC, apart from the opposite charge, no obvious visual property can be used to identify the particles. Since the energy of the particles is to high, the separation cannot be done in the TPC (green) so the calorimeter (red) and muon system (blue) have to be used. Additionally, the produced neutron is not visible in the TPC but may be the source of one of the isolated clusters in the calorimeter.

momentum spectrum for muons and pions as produced by GENIE is shown in Figure 9.3 on the right .

9.3 Boosted Decision Tree (BDT) Classification

The identification of muons and pions in the energy region of 250 MeV to 5 GeV is a challenging task, since typical calorimetric observables like hit energy and number of hits follow a similar distribution. It is therefore necessary to use multivariate techniques to harness subtle differences or correlations in the observables, that would otherwise pass unnoticed in a cut based analysis. To be able to judge the performance of the multivariate classifier it is necessary to understand the features of the input variables.
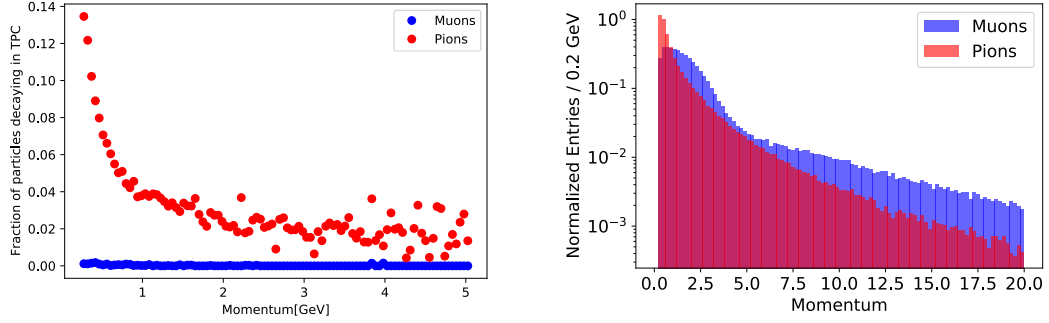
Figure 9.3: Left: The fraction of muons ad pions decaying inside the TPC for the studied momentum range. Since the mean lifetime of a pion is about two orders of magnitude shorter compared to the muons more particles are decaying, especially at low momentum. Right: Resulting normalized momentum spectrum of muons and pions as produced by GENIE. The following study will focus on the region between $250\,\mathrm{MeV}$ to $5\,\mathrm{GeV}$ which includes the majority of the particles and covers the first and second neutrino oscillation maximum. This region is especially interesting from a detector development point of view because the relative abundance of muons and pions and the relevant interaction channels with the detector vary considerably.

Figure 9.4 shows two examples of such distributions for the muon and pion samples, more are shown in Appendix A.

Most of these basic distributions have a huge overlap so it is necessary to implement variables sensitive to the different particle type. One possibility is the asymmetry in the energy deposition throughout the layers of the calorimeter and is defined by:

$$\mathrm{Asymmetry} = \frac{\mathrm{E_{max,Layer}} - \mathrm{E_{min,Layer}}}{\mathrm{E_{max,Layer}} + \mathrm{E_{min,Layer}}} \tag{9.1}$$

In this equation $\mathrm{E_{min,Layer}}$ and $\mathrm{E_{max,Layer}}$ denote the minimum and maximum energy sum per layer. The resulting distribution is shown in Figure 9.5.

As expected, the two particle types behave differently. Pions tend to undergo hadronic interactions leading to large but localized energy depositions in adjacent layers causing the asymmetry. Muons however, tend to pass the ECAL leaving an ionization track or stop within the detector. None of these interactions cause massive localized energy depositions, therefore the asymmetry is less pronounced. Since pions can also penetrate the detector or generate secondary particles with low energy, the distributions also have an overlapping tail. To further increase the amount of sensitive variables, the muon identification (MuID) system is used. Because of the large material content of $15\,\mathrm{cm}$ of Iron, the probability for a pion to undergo a hadronic interaction is increased. This behavior is reflected in the distributions shown in Figure 9.6.

While in Figure 9.6 on the left the vast majority of muons either passes through the MuID leaving on average three hits[1] or is stopped in the ECAL, pions have a pronounced

---

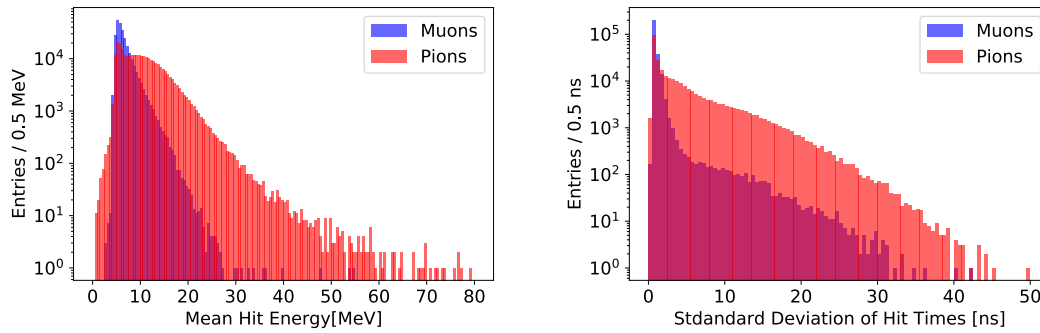[1] The MuID has three active layers, see Section 7.1

Figure 9.4: Left: Mean hit energy in the ECAL produced by muons and pions. Due to the hadronic nature the pions can produce particle showers, increasing the local energy density and therefore the hit energy. Right: Standard deviation of hit times in the ECAL for muons and pions. The higher yield of slow neutrons produced by hadronic processes caused by pions leads to a longer and more pronounced tail.
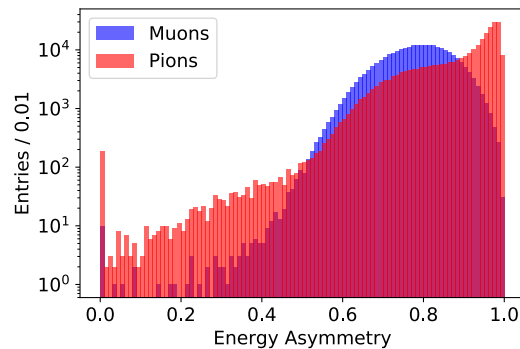

Figure 9.5: A measure of the asymmetric energy deposition in the calorimeter. The asymmetry scales with the difference of the maximal layer energy to minimal layer energy (Equation (9.1)).

tail towards large numbers of hits, a signature for secondary particle production. Similar arguments hold for the standard deviation of the hit energies in the MuID shown in Figure 9.6 on the right. Most muons leave an ionization track with a relatively narrow energy spectrum while the pions produce secondary particles thus increasing fluctuations in the deposited energy within one event and broadening the spectrum.

To identify muons and pions in the ECAL and MuID a binary classifier in the form of a Boosted Decision Tree (BDT) [85] is used. In contrast to a single decision tree a BDT adds multiple decision trees, thus sequentially reducing the error of the previous tree. While an individual tree represents as a weak learner and potentially yields only a slight improvement compared to random guessing, the ensemble of trees forms a strong classifier with a much higher accuracy. This method of tree learning is called gradient boosting. The approach is capable of picking up small differences in the distributions
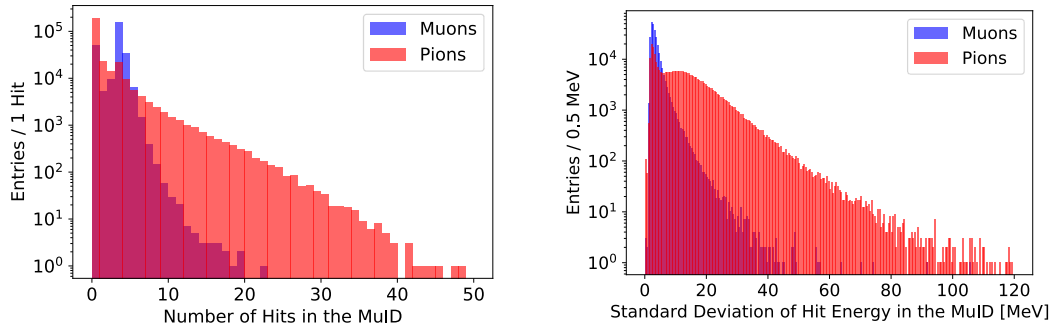
Figure 9.6: Left: Reconstructed number of hits in the MuID. This shows the working principle of the MuID in identifying the punch-through muons producing on average 3 hits corresponding to the number of layers. Pions have a higher chance to produce more hits, if they penetrate the calorimeter and interact hadronically inside the cryostat or MuID. The entries at 0 are caused by particles, mostly at low momentum, stopping in the calorimeter. Right: Standard deviation of the hit energies in the MuID. This distribution shows the tendency of pions to interact hadronically and produce hits of higher energy, while the hit energies in muon events are less spread.

of the input variables and produces a floating point number between 0 and 1 as output. In the setup used for this classification task this number denotes the probability of the event to fall into the muon category (Signal). Its complement denotes the probability to belong to the pion category (Background). The used input variables are shown in the following list, all of them are event based:

- **Energy Sum**: Reconstructed energy sum of an event in the calorimeter

- **Energy Sum - MuID**: Reconstructed energy sum of an event in the muon ID

- **Number of Hits**: Reconstructed number of hits in the calorimeter

- **Number of Hits - MuID**: Reconstructed number of hits in the muon ID

- **Mean Hit Energy**: Mean hit energy in the calorimeter

- **Mean Hit Energy - MuID**: Mean hit energy in the muon ID

- **StdDev Hit Energy**: Standard deviation of hit energies within one event in the calorimeter

- **StdDev Hit Energy - MuID**: Standard deviation of hit energies within one event in the muon ID

- **Maximum Hit Energy**: Maximum hit energy in the calorimeter

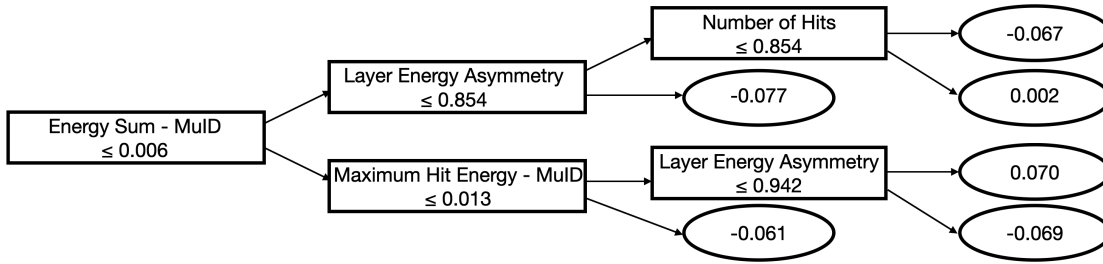- **Maximum Hit Energy - MuID**: Maximum hit energy in the muon ID

Figure 9.7: An individual decision tree. Many of those trees evaluated in succession by adding up the values in the respective leafs (ovals). The output of the classifier denotes the probability of the event to belong to the muon category.

- **StdDev Energy per Layer**: Standard deviation of the energy sum per layer in the calorimeter

- **Layer Energy Asymmetry**: Energy asymmetry per layer (see Equation (9.1))

- **Layer CoG**: Layer wise center of gravity of energy depositions

- **StdDev Hit Time**: Standard deviation of the hit times in the calorimeter

The classifier is implemented and trained using the python package of the LightGBM framework [86] for tree learning algorithms using gradient boosting. An example of an individual tree is shown in Figure 9.7.

It consists of nodes, branches and leafs. The nodes are holding a condition on an input variable (event based observable) which, in this case, is a threshold placed on a numerical value to produce a binary output (yes/no) indicating whether the variable is above or below the threshold. Depending on the outcome of the evaluation, the branches connect to the deeper nodes holding the next condition. After the deepest nodes are evaluated the branches connect to leafs holding the probabilistic output p_i of the respective tree. By subsequently evaluating the full ensemble of N trees and adding up all the outputs, the result of the classification P is obtained.

$$P = \sum_{i=1}^{N} p_i \tag{9.2}$$

In order to generate the ensemble of trees, obtaining the thresholds in the nodes and probabilities in the leaves, the BDT has to be trained. The first step of this procedure is the generation of a set of events that contains all the input variables as well as a label indicating the affiliation to the pion or muon category. This data set is split into two subsets called training and validation. In this case the training set contains 80%, the validation set contains 20% of the original set. The training procedure starts with a single initial tree. In the first iteration the algorithm tries to classify a random sub-sample of the training set and compares the performance to the truth information encoded in the

labels. The second iteration adds a new tree to the ensemble that tries to improve on the performance of the first trees output p_0. This iterative procedure continues until the maximum number of trees is reached or a stopping condition is fulfilled. In this case, training is stopped if no significant improvement in classifying the validation set was achieved during the last 5 iterations. Mathematically the algorithm tries to minimize a so called *loss function* . A common loss function for a binary classification task is the binary cross-entropy

$$H_p(q) = \frac{-1}{N} \sum_{i=1}^{N} y_i \cdot \log(p(y_i)) + (1 - y_i) \cdot \log(1 - p(y_i)) \tag{9.3}$$

In this function, N is the number of data points (number of events), y_i are the labels of the data points (0 for muon, 1 for pion) and $p(y_i)$ is the predicted probability of the event being a muon. A detailed derivation of this formula is given in [85]. This function reaches its minimum if the predicted probability distribution $p(y)$ is equal to the true distribution q. In other words, the final ensemble of decision trees represents an approximation of the real momentum dependent distribution of muons and pion.

The procedure described above is applicable to arbitrary shapes of trees as long as at least one node and two leaves are present. In reality however, an appropriate tree structure is vital for a successful classification and to prevent over-fitting. This happens if the tree learns to perfectly predict the training sample by tuning its parameters to every single data point. This usually happens if the BDT has too many free parameters, i.e. the number of generated trees is to large or the individual trees are to big. Consequently, the model performs very good in predicting the training set but fails when applied to an unknown data set without labels. Under-fitting occurs if the trees don't have enough free parameters to pick up the features of the input distributions and thus the BDT lacks information. A first method to prevent these effects was already implemented as the stopping condition mentioned earlier, by evaluating the performance using a validation set that is not used for training. Under-fitting is characterized by bad performance for training and validation set. Hence, if the accuracy for the training set increases while the accuracy for the validation set decreases, over-fitting might occur. LightBGM provides additional means to control the tree structure, the following list shows the most important ones:

- **Number of boost rounds**: The maximum number of subsequent trees generated in training of the classifier. To many trees might increase the tendency to over-fit the training data.

- **Maximum depth**: The maximum depth D_{max} of the individual trees. The maximum depth corresponds to the maximum number of nodes $N_{\mathrm{Nodes}}^{\mathrm{max}}$ by a simple sum rule:
$$N_{Nodes}^{max} = \sum_{i=0}^{D_{max}-1} 2^i$$

Shallow trees might lead to poor performance, but too many nodes increase the chance of over-fitting.

- **Number of leaves**: The maximum number of leaves. A leaf holds the probabilistic output of the particular tree.

To optimize the performance of the algorithm it is usually not enough to choose the best suited trees, the training itself must be appropriate as well. The list below explains the parameters used to steer the training of the classifier.

- **Learning rate:** The learning rate is a number between 0 and 1 and limits the improvement per iteration of the training process. A low learning rate results in a potentially larger ensemble of trees and prolongs the duration of the training. A large learning rate leads to a faster learning but may reduce the accuracy of the model.

- **Minimum child samples:** The minimum number of data points used to create a new node. If this number is to small, the algorithm creates nodes that only describe small sets of specific data points and therefore looses the ability to generalize to unknown data. This promotes over-fitting.

- **Feature fraction:** This parameter describes the fraction of features used to generate a new tree. This fraction is chosen randomly for every tree in the ensemble and mainly impacts the training time by reducing the number of evaluations of the data set to create a new node.

- **Bagging fraction and bagging frequency:** Bagging describes a training procedure using multiple random samples of the training data set. For example, a bagging frequency of 5 and a bagging fraction of 0.75 results in re-sampling of the training set without replacement every 5 iterations, and draw samples in size of 75% of the full training set.

How to set these so-called *hyper parameters* to optimize the performance is a time consuming process. Usually a set of parameters is used to train multiple BDTs and compare them based on their accuracy in predicting the validation data set. The BDT parameters reported in the following have been obtained with a grid search over the parameters *Maximum Depth*, *Number of leaves*, *Bagging fraction*, *Minimum child samples* and *Feature fraction*.

9.4 Performance in Separation of Muons and Pions

This section reports on the capabilities of the simulated ND-GAr design to separate Muons from Pions produced by neutrino interactions. To classify the events a Boosted Decision Tree (BDT), introduced in the previous section, is used. The first study will investigate the full detector including the MuonID, to set a baseline for neutrino and

anti-neutrino mode. In subsequent studies the impact of the MuonID will be examined by excluding parts of the information or the full system from training and testing. To investigate the impact of the momentum distribution produced by GENIE, an additional study using a flat muon and pion momentum distribution is conducted.

Baseline Performance

In order to compare variations in the detector setup or in the data sample, the baseline performance is chosen to include the full calorimeter and MuID information. The training data set consists of 280000 labeled events of muons and pions each, the test set contains 530000 events of muons and pions at a ratio of 75.3% to 24.7%. For neutrino mode, in the following called forward horn current [2] (FHC), the muons have negative charge, the pions have positive charge. For anti neutrino mode, termed reverse horn current (RHC), the charge is reversed according to charge conservation in weak interactions (Figure 9.1). To evaluate the performance of the BDT during training, 20% of the training set is used for validation. The evolution of the binary cross-entropy, which is used as a loss function during training of the FHC data set, is shown in Figure 9.8. The training continues until the loss does not change for the last 5 iterations, in this case 1357 trees are produced. Within the first 100 iterations the value of the loss function decreases rapidly, hence the probability of a correct classification increases. After training, an important information to evaluate the usefulness of the features is the so called *feature importance*. Two popular types of measures are used to quantify this, the gain and split method. The gain method is based on the relative contribution of a given feature to the output of the model and is calculated by summing its contribution for each tree in the model. A higher gain value implies a higher importance for making a prediction. The split method is purely based on the number of times a given feature occurs in the trees of the model. Both methods are shown in Figure 9.9.
The ranking of the features differs significantly between the two methods. The most important feature according to gain is the standard deviation of the deposited energy per layer while for the split method it is the standard deviation of the hit time. This behavior is based on the hadronic nature of the pion, since it is much more likely to cause a particle shower in the calorimeter. In contrast to the minimal ionizing track of the muon, the energy deposition in such a shower is subject to high fluctuations (Section 3.1). Also the features associated to the MuonID score higher using the gain metric, a first hint on the usefulness of this system. Features scoring high in gain, but lower in splits are used in few trees to make strong predictions while features scoring higher in splits probably tweak the end result with an overall smaller impact on the classification score. Features with less importance in both metrics, like the reconstructed energy sum, are less useful for the end result and removing them does not deteriorate the overall performance significantly. In order to evaluate the prediction power of the trained BDT it is used to classify the test set without knowing the true particle species. For each of the 530000 events a probability

---

[2]This nomenclature is based on the direction of the current through the magnetic focusing horns. Neutrino mode is defined as forward horn current, anti neutrino mode as reverse horn current.
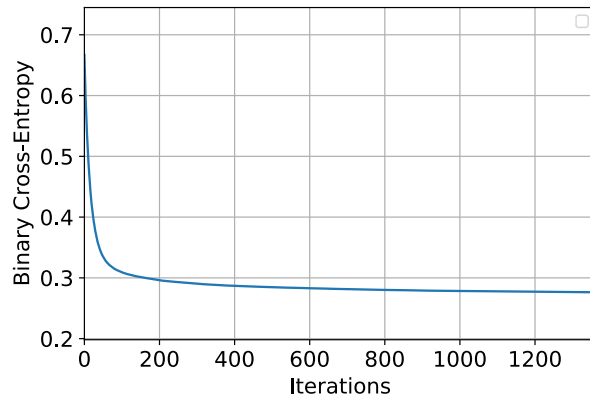
Figure 9.8: Evolution of the binary cross-entropy (Equation (9.3)) during training. During every iteration a new tree is added to the ensemble and the loss function is evaluated. After no significant change is achieved within 5 iterations, the training is stopped.
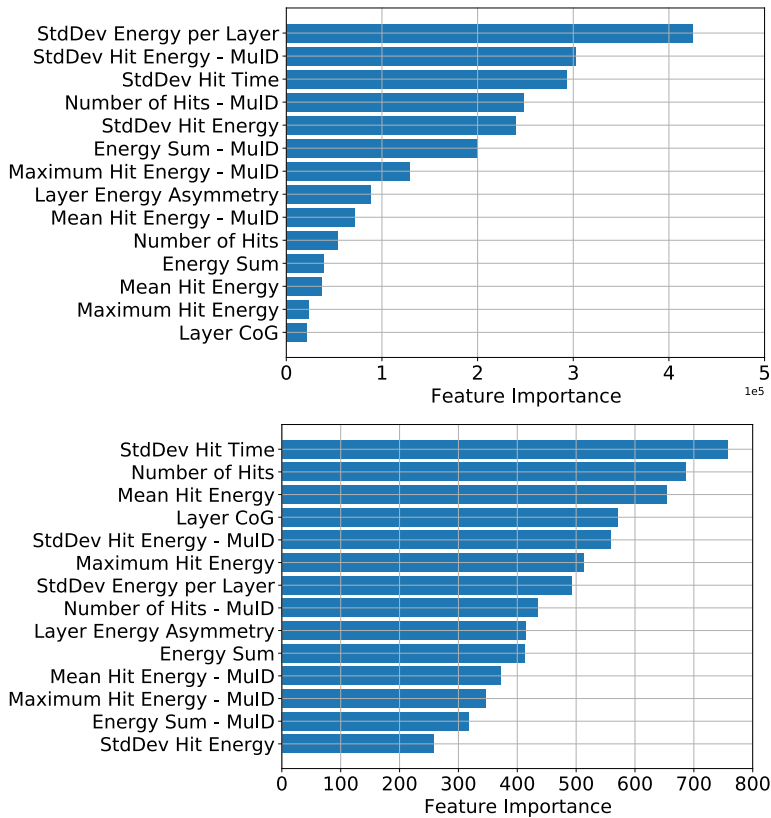

Figure 9.9: Top: Feature importance by gain. The numbers represent the information gain associated to the respective input variable for the ensemble of trees. Bottom: Feature importance by splits. The numbers indicate the amount of decisions taken with the respective feature.
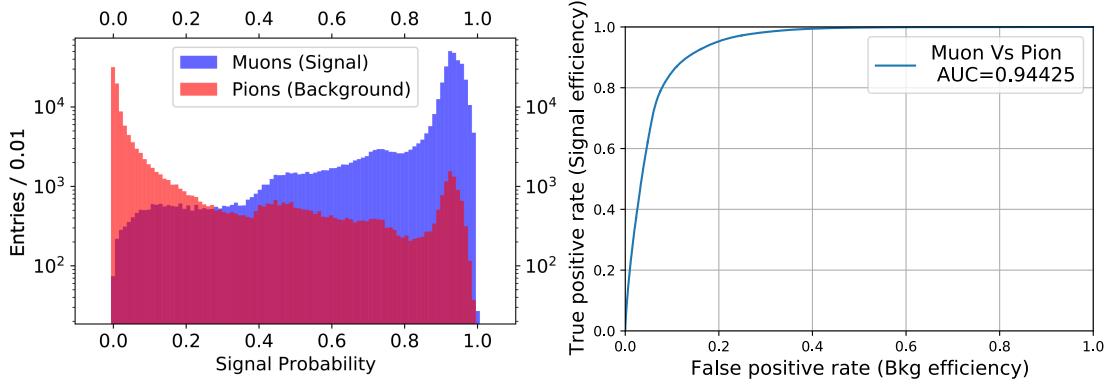
Figure 9.10: Left: Distribution of the signal probabilities assigned to muon and pion events by the BDT. The colors encode the true particle species. Right: Receiver-operating-characteristic (ROC) curve representing the correlation of false positive and true positive rate. This curve is obtained by scanning the classification threshold an the signal probability (right image) and calculating the rates.

to belong to the muon (Signal) category is calculated, the distribution for the muon and pion truth labels is shown in Figure 9.10 on the left.

As expected, the signal probability for the muons accumulates at high values while the majority of pions accumulate at low values. However, the tails of the distributions overlap across the full probability range and especially the pions show a secondary accumulation at high signal probability. The reason for this is the small mass difference of only $34\,\mathrm{MeV}$, therefore both particle species can be considered minimum ionizing over the studied energy range. Regardless of its hadronic nature the pion has a considerable probability to traverse the detector without undergoing a hard interaction. The topology of these so called *punch-through* pions is very similar, in some cases even identical, to a muon signature. The probability for punch-through depends on the detector thickness in terms of the nuclear interaction length λ.

$$P_{punch-through} = \mathrm{e}^{-\lambda} \tag{9.4}$$

For a combined thickness of calorimeter and MuID of about 2λ the probability is 13.5%. Hence, for a muon to pion ratio of 75.3% to 24.7% as produced by GENIE, assuming a 90° incidence, about 3% of pions will only produce an ionizing track throughout the two detectors. This is to be understood as a maximum value, further possible nuclear interactions at low momenta and the effective increase of traversed material by curved tracks diminish this chance. Furthermore, as discussed in Section 3.1, the topology of hadronic showers is subject to large fluctuations. A soft hadronic shower with minimal particle multiplication may get confused with a delta electron produced by a minimal ionizing muon.

Depending on the choice of classification threshold the true positive rate (TPR) and false positive rate (FPR) can be tuned. The receiver-operating-characteristics (ROC)

curve provides the relation between these two quantities as shown on the right side of Figure 9.10. This curve is obtained by calculating TPR and FPR for every classification threshold, making it a useful tool to evaluate the performance of the classifier for the given data set. A linear relation like TPR=FPR characterizes a random classification, the BDT is behaving like a coin toss experiment and the area under the ROC curve (AUC) equals 0.5. A perfect classification is characterized by FPR=0 for every possible threshold and AUC=1.0. The AUC is often used to quote the quality of a binary classification task since its definition is identical for any mechanism of classification. Usually, classifiers are tuned to produce either a very pure signal sample or a very efficient signal identification by adjusting the classification threshold. The shape of the ROC curve can be used as a guideline. In the given case, a threshold of P=0.5 corresponds to a TPR of 92% and a FPR of 15.5%. In order to make the classification efficient and increase the TPR to 99%, the threshold has to be lowered to P=0.11 which in turn results in an increased FPR of 36%. If a very pure muon sample has to be obtained (FPR<1%), the threshold has to be increased to P>95% which leads to a rejection of about 80% of true muons. This trade-off has to be considered in every classification task and strongly depends on the type of analysis the produced dataset is used for.

In the following part of the analysis, the purity and efficiency for muons and pions at a classification threshold of 0.5 are evaluated to obtain a baseline for the performance. For a detailed view on the core region of the DUNE beam the studied momentum ranges from 0.25 GeV to 5 GeV. The range is subdivided into bins of 0.15 GeV and efficiency and purity are obtained for every bin. The quantities are defined in the following way:

$$
\mathrm{PionEfficiency} \quad = \quad \frac{\#\mathrm{TruePositivePions}}{\#\mathrm{TruePions}} \tag{9.5}
$$

$$
\mathrm{PionPurity} \quad = \quad \frac{\#\mathrm{TruePositivePions}}{\#\mathrm{TruePositivePions} + \#\mathrm{FalsePositiveMuons}} \tag{9.6}
$$

$$
\mathrm{MuonEfficiency} \quad = \quad \frac{\#\mathrm{TruePositiveMuons}}{\#\mathrm{TrueMuons}} \tag{9.7}
$$

$$
\mathrm{MuonPurity} \quad = \quad \frac{\#\mathrm{TruePositiveMuons}}{\#\mathrm{TruePositiveMuons} + \#\mathrm{FalsePositivePions}} \tag{9.8}
$$

The results are shown in Figure 9.11.

Above 1 GeV the efficiency and purity for muons is stable above 95%, reaching up to 98% for purity and 99% for efficiency. The low momentum efficiency for muons increases from 82% at 0.25 GeV to 94.5% at 1 GeV. The main reason for this is the ratio of muons and pions in this energy range. While the ratio of muons to pions is at 75.3% to 24.7% for the full data set, the ratio is 1:1 for momenta below 0.8 GeV leading to an increased probability of misclassification. Therefore, the sample purity of muon and pion decreases, while the efficiency for pion classification increases. For momenta below 400 MeV the data set contains twice as many pions, hence the increased efficiency. Additionally, the distributions of the input data get very similar at low momenta so the ambiguity increases.

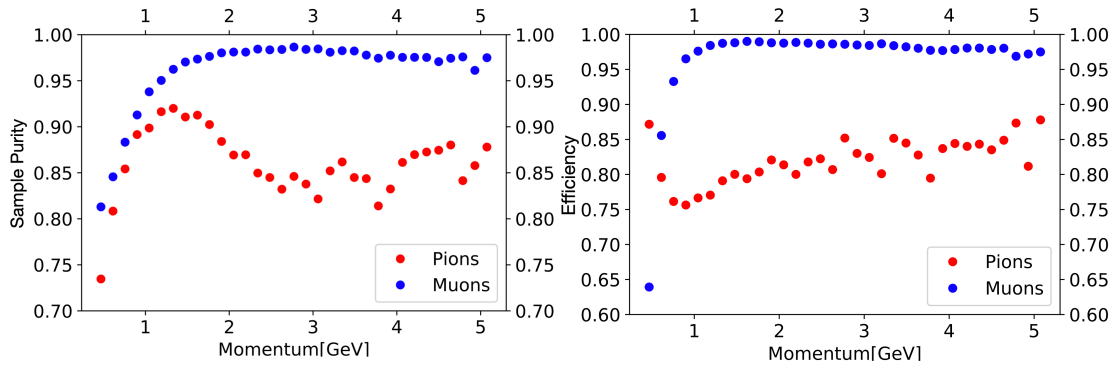A possibility to mitigate this issue is the inclusion of the reconstructed momentum in the

Figure 9.11: Left: Purity of the classified muon and pion events in the studied momentum range. The numbers are obtained according to Section 9.4 in bins of 0.15 GeV. Right: Efficiency of the classification of muon and pion events in the studied momentum range. The numbers are obtained according to Section 9.4 in bins of 0.15 GeV. The numbers shown in both figures are used as a baseline performance to study the impact of the MuonID system in Section 9.5.

input features. Since the TPC provides a precise measurement, the BDT could pick up a sensitivity for the relative abundance of muons and pions depending on their momentum. This however is a dangerous approach, since momenta above 5 GeV are mainly populated by muons (Figure 9.3) so the bias towards muon identification in this region increases. Even though these high momentum pions are rare, their identification may be vital for analyses aiming on precise cross section measurements so an artificial bias based on the momentum distribution is undesirable. Since the momentum of the unidentified particle is known, specialized classifiers can be trained for high momentum particles.

Particle Interactions at Low Momenta

To understand the behavior of the BDT at momenta of 1 GeV and below the interactions have to be investigated on the Monte Carlo truth level. The large number of events at these momenta are increasing the types of nuclear interactions that are usually not present in typical high energy particle physics experiments. It is important to note that, even though the minimal final state momentum is 250 MeV, the particles loose energy while they traverse the TPC and the ECAL and ionize the medium. At the minimum momentum both muons and pions are considered minimum ionizing particles (MIPs) according to Bethe-Bloch (Section 3.1), but an energy loss at the order of 100 MeV already leads to a steep increase in stopping power. Considering the curvature of the particles in the magnetic field and thus the increase in traversed absorber and scintillator, combined with the occasionally large energy loss by landau fluctuations, this energy loss becomes significant. Nuclear effects like capture reactions and resonances, as well as the pion decay, begin to play a role.
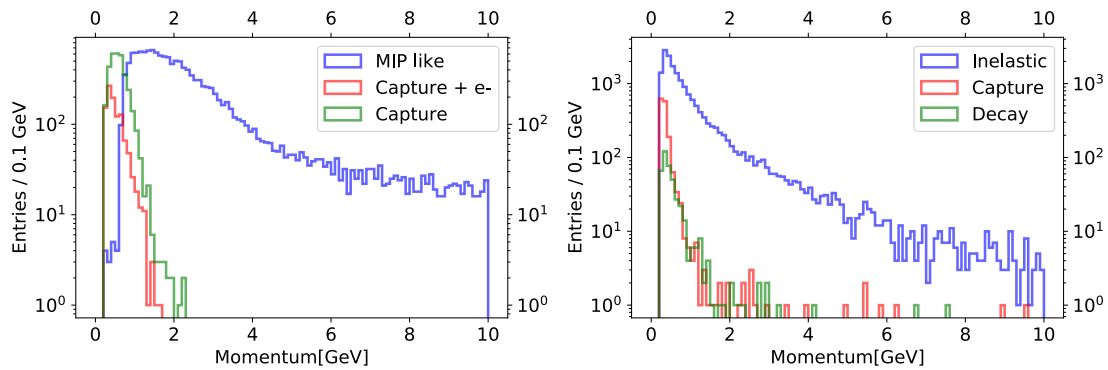
Figure 9.12: Left: Momentum spectrum of muons produced with GENIE for capture and MIP like events in the calorimeter. Below 1 GeV the majority of muons is captured in the detector either by transferring the charge to the nucleus (green) or electron emission (red). Above this threshold the vast majority of muons traverse the detector volume and leave an ionization track (blue). Right: Momentum spectrum of pions produced with GENIE for inelastic (blue) or capture reactions (red) and decay at rest (green) inside the calorimeter.

In Figure 9.12 the three most important types of interactions in the detector are shown for muons and pions in the studied momentum range. Below 1 GeV the majority of muons is captured by a nucleon of the material in the ECAL. This transfers recoil energy to the nucleus and causes a subsequent nuclear de-excitation and production of neutrons, gammas and alpha particles in rare cases. The decay of the muon inside the nucleus and release of an electron is possible but less likely. Above 1 GeV the topology is dominated by MIP like events without captures or other reactions that destroy the muon. While most of the pions undergo inelastic interactions with the detector, at low momenta a considerable amount of them is either captured or decays at rest. Since these reactions are causing different signatures in the detector, the BDT will pick them up. Figure 9.13 and Figure 9.14 show the distributions of the reconstructed hits and the energy sum in the ECAL separately for the different event categories. While the MIP like events and the inelastic pion interactions show their distinctive signatures, the difference between captured muons and captured or decaying pions decreases resulting in largely overlapping distributions. Additionally, the relative amount of muons and pions in the data sample changes with momentum. In contrast to the muons, the pion sample is never dominated by nuclear reactions which only make up a minor part of the low momentum spectrum, but there are about three times more pions below 1 GeV. The combination of these effects leads to a decreasing sample purity in Figure 9.11 while the pion efficiency increases due to the excess of events.
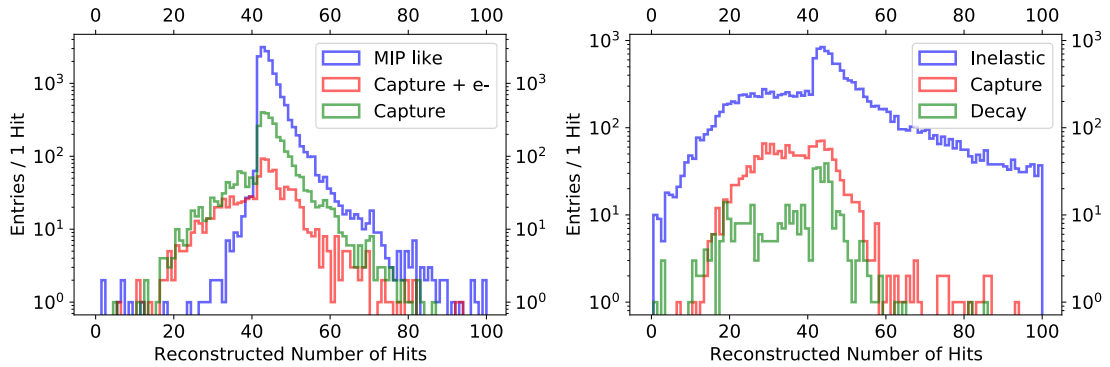
Figure 9.13: Left: Reconstructed number of hits in the ECAL for MIP like muons (red), captured muons with electron emission (green) and captured muons with charge absorption by the nucleus. Right: Reconstructed number of hits in the ECAL for pions interacting inelastically (blue), captured pions (red) and decays at rest (green). The range of the histogram is restricted to better visualize the interesting region.
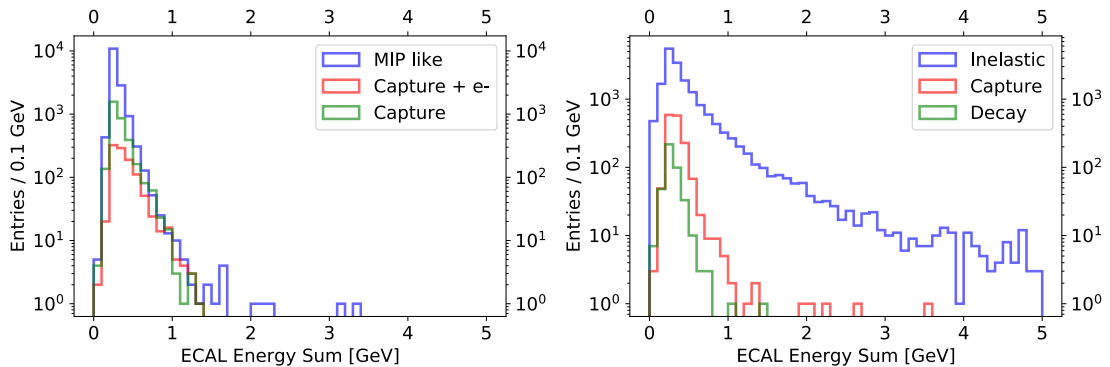

Figure 9.14: Left: Reconstructed energy sum in the ECAL for MIP like muons (red), captured muons with electron emission (green) and captured muons with charge absorption by the nucleus. Right: Reconstructed energy sum in the ECAL for pions interacting inelastically (blue), captured pions (red) and decays at rest (green). The range of the histogram is restricted to better visualize the interesting region.

Tuning for Efficiency and Purity

The detection threshold of P=0.5 is an intuitive choice for compromise between efficiency and purity but may not always be optimal with regard to the analysis. Depending on the physics case, very pure data samples may be needed so the admixture of false positives has to be minimized. By tuning the threshold these quantities can be adjusted within a certain margin. Figure 9.15 and Figure 9.16 show the efficiency and purity for muons and pions for various classification thresholds.
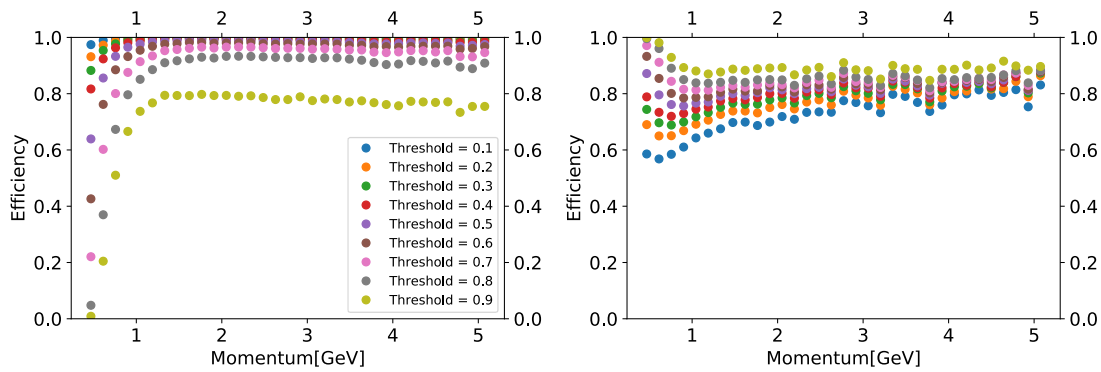
Figure 9.15: Left: Muon identification efficiency for different classification thresholds. Right: Pion identification efficiency for different classification thresholds. In both cases a threshold of 0.5 corresponds to the baseline performance discussed before.
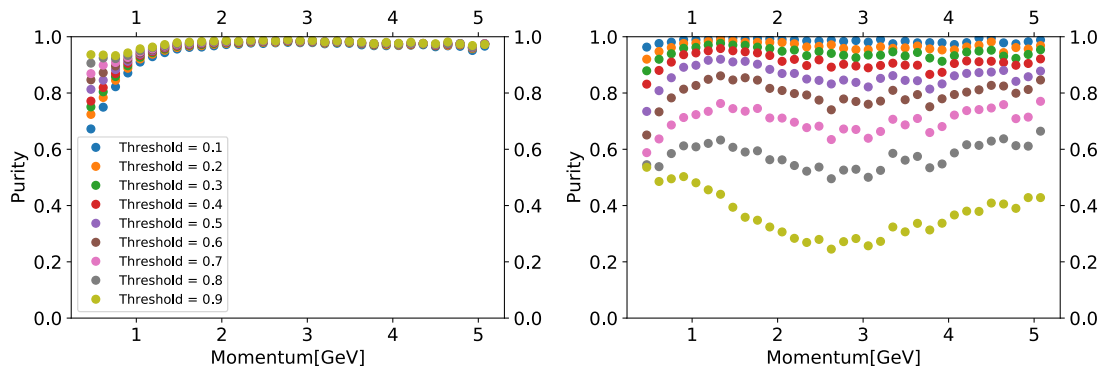

Figure 9.16: Left: Purity of the classified muon sample for different classification thresholds. Right: Purity of the classified pion sample for different classification thresholds. In both cases a threshold of 0.5 corresponds to the baseline performance discussed before.

A global observation shows that a decreasing threshold increases the muon efficiency but decreases the pion efficiency. Furthermore, it decreases the muon purity while increasing the pion purity. Consequently, the tuning for efficiency or purity always deteriorates the performance for the opposite particle species. A more detailed comparison of the figures shows that the muon purity (left plot in Figure 9.16) is almost independent of the threshold for momenta above 1 GeV. The muon efficiency in Figure 9.15 on the left shows higher sensitivity to the threshold for values of P>0.4 but a rather small sensitivity for P<=0.4. It is therefore possible to tune the classification to a high pion purity (right side in Figure 9.16) without deterioration of the muon purity. At the same time the pion efficiency (right plot in Figure 9.15) suffers considerably from an increased purity, especially in the lower momentum region.

Training with a Flat Momentum Distribution

As explained before, the momentum distribution of the particle in the training sample, and therefore the topology of the events shown to the BDT, plays a crucial role in classification. These events produced with the GENIE generator cannot reflect the true distribution because of the limited accuracy of the input models and datasets from which the events get generated. Especially the modeling of final state interactions (FSI) of hadrons, generated in neutrino interactions (e.g. Figure 9.1), with the surrounding nucleus is a source of large uncertainties. Comparisons with other neutrino generators like NuWro [87] or NEUT [88] using slightly different implementations are described in [89]. In order to study the behavior of the classifier with different momentum distribution for training and test data set, the BDT is trained with flat muon and pion momentum distributions between 250 MeV and 5 GeV in steps of 50 MeV. Each step contributes about 3150 events to the training sample. Besides the different total momentum distribution, the direction of the muons and pions also differs considerably from the GENIE distribution. Due to the limitations of the simulation framework, it is not possible to provide a momentum dependent distribution of the emission angle of the primary particles, therefore it can not model the Lorentz boost of the final states. Instead, a gaussian distribution of the emission angle with a variance of 90° around the beam direction is used. The origin of the primary particles is also randomized within the fiducial volume of the TPC. The output of the classifier is shown in Figure 9.17 for the BDT with and without the reconstructed momentum as input feature.
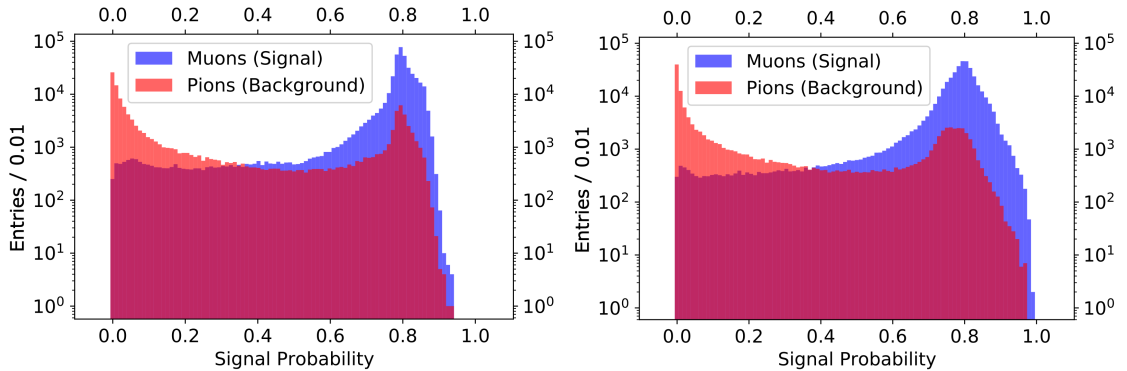

Figure 9.17: Left: This histogram shows the output of the BDT, trained with the flat momentum and particle distribution and tested on the GENIE dataset. The reconstructed momentum of the particle is not included in the input features. Right: This histogram shows the output of the BDT, trained with the flat momentum and particle distribution and tested on the GENIE dataset. Here, the reconstructed momentum of the particle is included in the input features.

In both cases the Pion identification features a pronounced spike at zero probability, similar to the output for the GENIE data set. In the left plot however, the muon identification never reaches a probability of 100% due to the fact that pions and muons can look very

similar and even identical in some cases. The missing momentum information together with an equal amount of muons and pions in the training sample for the full momentum region takes away the most valuable feature for muon identification. Including the momentum information recovers the muon performance considerably for probabilities between 85% and 100%. This behavior is expected since the momentum of the test data set is distributed according to the realistic expectation produced by GENIE.

Figure 9.19 compares the purity (left) and efficiency (right) of the classification of the GENIE test data set, obtained with a BDT trained on the flat and the GENIE training data set, respectively. The filled circles correspond to the baseline scenario discussed before.
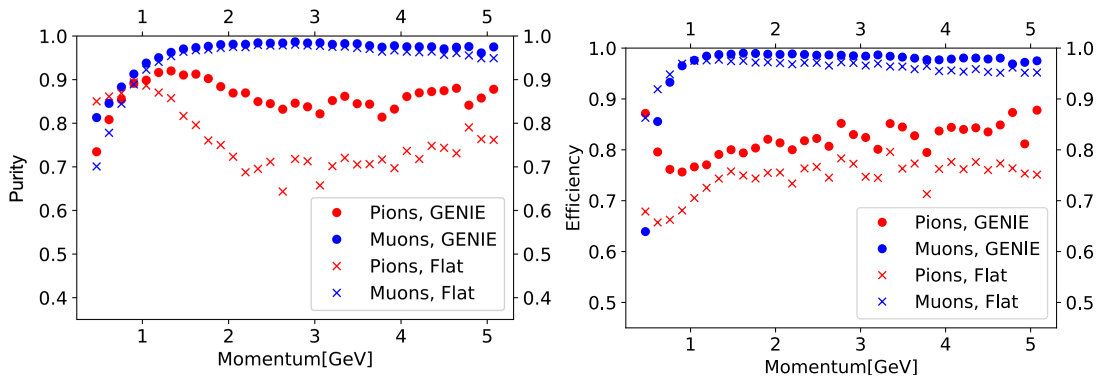
Figure 9.18: Left: Comparison of the sample purity achieved by the BDT for the GENIE momentum distribution (filled circle) and the flat momentum distribution (cross). Right: Comparison of the efficiency achieved by the BDT for the GENIE momentum distribution (filled circle) and the flat momentum distribution (cross). The BDT trained on a flat momentum distribution does not include the reconstructed momentum as feature (left side in Figure 9.17).
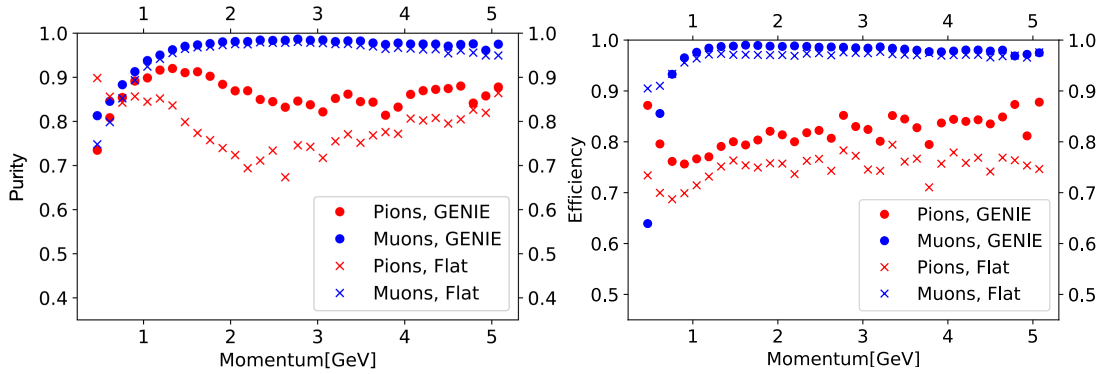
Figure 9.19: Left: Comparison of the sample purity achieved by the BDT for the GENIE momentum distribution (filled circle) and the flat momentum distribution (cross). Right: Comparison of the efficiency achieved by the BDT for the GENIE momentum distribution (filled circle) and the flat momentum distribution (cross). The BDT trained on a flat momentum distribution includes the reconstructed momentum as feature (right side in Figure 9.17).

Compared to the GENIE case, the performance changes considerably when using a flat momentum distribution. For momenta below 1 GeV the pion purity exceeds the muon purity, which is not the case in the baseline scenario. The pion efficiency, however, deteriorates drastically. This is likely caused by the fact that the BDT sees a comparable amount of high energy and low energy signatures in training, while the occurrence of different event signatures is naturally weighted according to the realistic momentum distribution when using the GENIE training set. As explained before, the event signatures change drastically with increasing particle momentum. The efficiency deteriorates because the BDT cannot reliably correlate certain event signatures to a momentum region. This explanation is further backed by the performance of the BDT trained with the flat distribution, but including the reconstructed momentum as input feature as shown in Figure 9.19. In this case the low momentum purity is significantly increased for muons and pions, while also the efficiency increased slightly. The high momentum performance receives only subtle performance gains.

Reverse Horn Current

A key necessity to perform the measurement on CP violation in the neutrino sector is the option to do the oscillation measurement with anti neutrinos and observe possible deviations. For the standard charged current neutrino interaction this implies that the charges of the final state particles are reversed and the expected event rates are different, because of a different initial flux and beam composition. Since the opposite charges of the final states are not expected to introduce significant changes in the response of the detector, the general setup of the classifier is unchanged. The initial muon to pion ratio

for reverse horn current is 65% to 35% and the corresponding momentum distribution is shown in Figure 9.20.
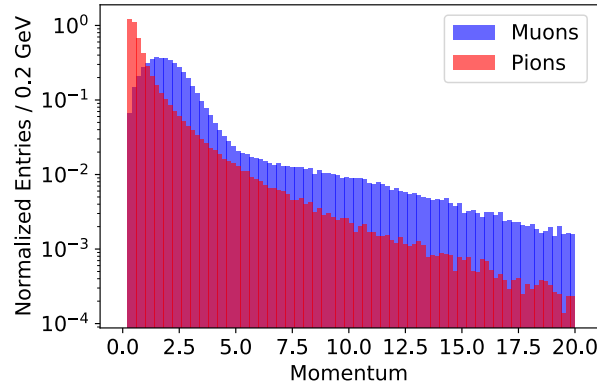

Figure 9.20: The momentum distribution of muons and pions in reverse horn current.

A fundamental difference compared to forward horn current is in the muon momentum distribution at low energies. Between 250 MeV and 1 GeV fewer muons are produced reducing the overlap with the pion distribution. As explained before, for decreasing momentum muons and pions look increasingly similar in the ECAL and MuID due to the different processes in the detector, hence a better performance is expected. Looking at figure Figure 9.21, the left side shows the probabilities assigned by the BDT for true muons and pions, the right side shows the ROC curve. Compared to forward horn current, the probability distributions are better separated and the intermediate region between the two extremes is less pronounced. The area under the ROC curve also covers more of the parameter space and indicates that, for a detection threshold of P=0.5, a true positive muon rate of 99% can already be reached at the cost of 15% false positive rate. The same performance in forward horn current was reached at a 37% false positive rate. Especially at momenta up to 1 GeV the efficiency and purity for pions is increased due to the decreased number of muons. The overall pion efficiency also increases by about 10%. The increased performance for reverse horn current is especially beneficial for the oscillation measurement, since the event rates in this mode are lower. A more accurate particle identification reduces systematics and leads to a statistics dominated nature of the measurement. This means that the uncertainty can be lowered by gathering more data, which is not the case in a systematics dominated measurement that usually involves upgrades of the detector and reconstruction algorithms. The lower the systematic uncertainty, the lower the combined uncertainty of an already small dataset.
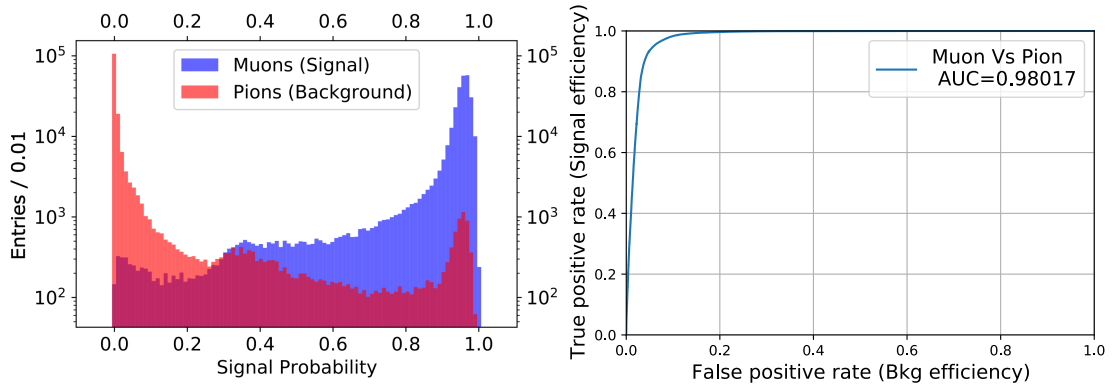
Figure 9.21: Left: BDT output for reverse horn current. The overall separation is better compared to forward horn current because of an already smaller overlap in the momentum spectrum at low values. As explained previously, this is th most difficult range for separation. Right: Receiver-Operating-Characterisitc for reverse horn current. A 99% true positive rate is achieved already at 15% false positive rate.
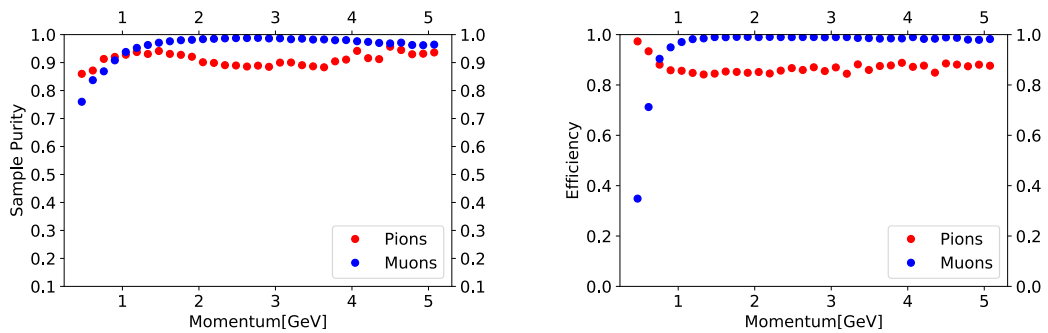

Figure 9.22: Left: Sample purity versus momentum for muons and pions in reverse horn current. Right: Efficiency versus momentum for muons and pions in reverse horn current.

9.5 Impact of the Muon Identification System

The detector configuration studied in this analysis contains, besides the TPC and calorimeter, a muon identification system (MuID) to enhance the capability of identifying muons. Since this system is embedded in the steel return yoke of the magnet, it will increase the cost of the system significantly because the yoke cannot be manufactured as one solid body but has to be segmented. It is therefore vital to study the impact of this system on the particle identification performance, especially the separation of muons and pions. The general concept behind this system is exploiting the hadronic nature of the pion. A dense metal absorber is used to induce hadronic interactions that will increase the local energy and particle density in the detector. The stopping power of muons in
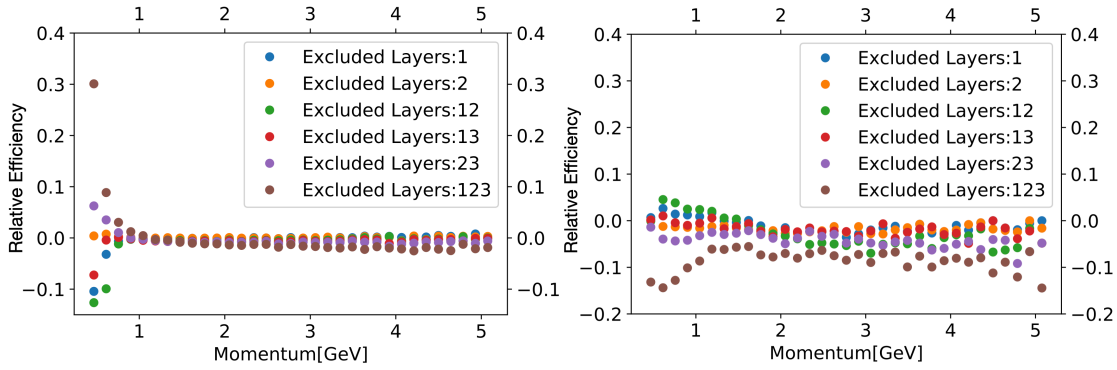
Figure 9.23: Left: Efficiency of the muon identification relative to the baseline scenario. Right: Efficiency of the pion identification relative to the baseline scenario. The colors denote the different cases of muon ID layers excluded from the reconstruction.
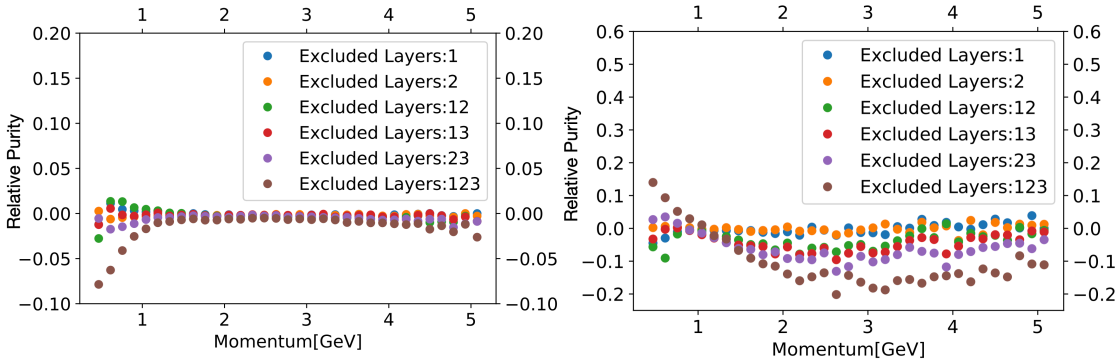

Figure 9.24: Left: Purity of the muon identification relative to the baseline scenario. Right: Purity of the pion identification relative to the baseline scenario. The colors denote the different cases of muon ID layers excluded from the reconstruction.

dense matter is solely governed by the Bethe-Bloch equation (Section 3.1) and is nearly minimal in the studied energy range. Since the MuID consists of three active layers, the expected signal topology for a muon would be three hits with landau distributed energies produced by the minimum ionizing particle. Besides ionization, the pion has a high chance to interact hadronically within the cryostat or yoke, and will produce more hits with a higher energy density. Additionally, pions stopped inside the yoke will be identifiable by the lack of energy in the outermost layer. This section will study the usefulness of the system depending on the particle energy and number of active layers. Furthermore, the importance of the observables provided by the MuID will be studied for high and low particle momenta.

To study the impact of the MuonID the classification is performed for different configurations of the system. This is achieved by excluding the information from one, two or all three layers from the input information of the BDT and training a separate classifier for

all possible configurations. The variables used to benchmark the classification are the efficiency and purity relative to the baseline scenario discussed previously. Figure 9.23 and Figure 9.24 show the relative efficiency and relative purity respectively for muons and pions. The colors encode the layers that are excluded from the classification with layer 1 being the innermost layer, layer two is the middle layer and layer 3 is the outermost layer. In front of every layer there is 5 cm of steel belonging to the return yoke. For muons, changing the different configurations only affects the low energy behavior up to a momentum of 1 GeV. Especially the scenario that excludes every layer of the MuID shows significant deterioration from the baseline and, contrary to the expectations, the efficiency for muons increases steeply. Hence, the general lack of information also reduces the risk to reject a true muon. This however goes with a deterioration of the muon purity and only implies that the detector has lost part of its capability to correctly identify pions, an effect that is enhanced by the excess in the number of pions in this momentum range. A look at the pion efficiency and purity further supports this argument. Here, the efficiency is deteriorated while the purity increases. This means that a pion is correctly identified if it leaves a distinctive signature in the ECAL in the form of a hard hadronic interaction raising the local energy and hit density. Without this feature it is difficult to differentiate them from stopping muons because of their similar rest mass, hence a similar deposited energy in the detector. An additional complication at low momenta arises from the potentially huge curvature of the tracks as they enter the calorimeter. Even at similar momenta, the angle at which the particles enter the calorimeter can vary considerably depending on the distance traveled through the TPC. A large angle of incidence leads to an increase in the amount of absorber the particle has to traverse, thus increasing the event by event fluctuations. As the momentum increases this effect vanishes by the increasing bending radius of the particle tracks. The pions show an increased sensitivity to the configuration of the MuID throughout the studied momentum range. Besides the already discussed increase in purity at low energies without MuID, the performance deteriorates as more and more layers are excluded from the classification. If only one layer is removed, the performance is not affected compared to the baseline. The three scenarios with a removal of two layers show a deterioration of the performance of 5% to 10% in purity, while the worst of the three is the one excluding the two outermost layers. Removing every layer deteriorates the purity by up to 20% and the efficiency by up to 10% at higher momenta. In conclusion, the MuID system overall increases the performance, especially the capability of identifying pions. Apart from the counter intuitive behavior at low momenta and the complications arising from the curvature of the tracks, excluding layers from the classification also deteriorates the performance. The inclusion of only one layer increases the pion purity by 10% to 15%, while the effect is largest for the outermost layer. This agrees with the expectation that the separation power rises with additional material in front of the last active detector layer. The pions have an increased chance to interact, while the chance of a muon stopping in the additional material remains small (see Section 3.1).

Feature Importance at Low and High Momenta

To confirm the importance of the MuID for higher momenta, the feature importance of the training of the classifier can be investigated. In the following, the feature importance is shown separately for momenta below 1 GeV (Figure 9.25) and above 1 GeV (Figure 9.26). The top five features in the low momentum classification only include a single feature from the MuID, the standard deviation of the hit energies, regardless if the split importance or gain importance is used. The reconstructed number of hits and the reconstructed energy in the MuID play a minor role, which means that the majority of the particles deposit most of their energy in the calorimeter. Looking at the higher momenta, the top five features of the gain importance include four features of the MuID and three in case of the split importance. The highest information gain is obtained from the reconstructed number of hits in the MuID which scores almost three times higher than the reconstructed energy sum in the MuID scoring second. This shows that the MuID performs as intended by inducing hadronic interactions of the pions in the return yoke and pick up the produced secondaries in the active layers.

Conclusion

The impact of the MuID system on the separation capability for muons and pions depends on various factors. For lower momenta the event topology varies considerably depending on the curvature of the particle track as it enters the calorimeter. For particles produced further away from the front face, the absorber thickness is increased by the large angle of incidence and the chance of containing the particle in the calorimeter rises. As the momentum increases, this effect vanishes and the cross section for hadronic interactions of the pions increases. Hence, the benefits of the system manifest themselves at momenta above 1 GeV. Compared to the performance of the calorimeter alone, the full MuID system including all three layers boosts the pion purity by up to 20% and the efficiency by up to 10% while the muon performance is almost unchanged. Since a three layered MuID also requires the return yoke of the magnet to be segmented and thus drives the cost of the system, the option of having a reduced system is investigated. The importance of the layers rises with increasing material content in front of them, so only having the outermost layer increases the performance by up to 10% compared to the calorimeter alone. From an integration point of view this is very convenient since the return yoke can in principle remain untouched while a single layer of scintillator with crossed strips is fitted around it.
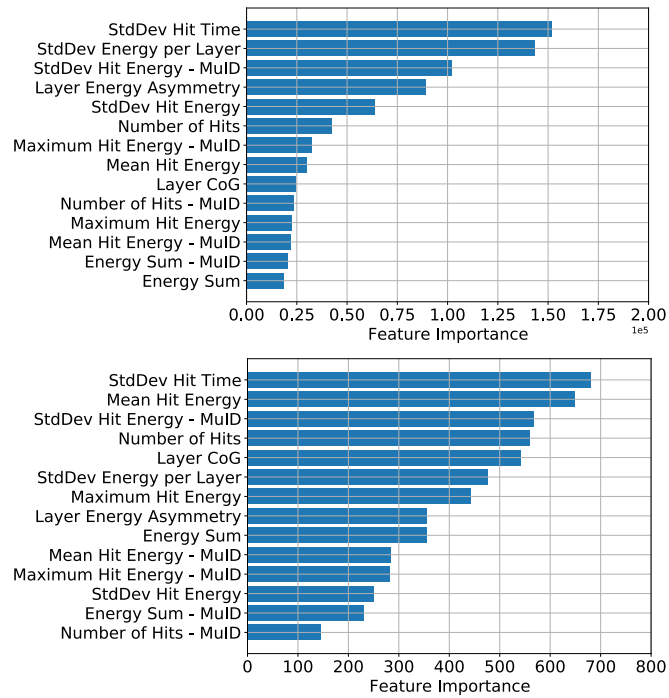
Figure 9.25: Gain (top) and split (bottom) importance of the input features for events below a momentum of $1\,\text{GeV}$.
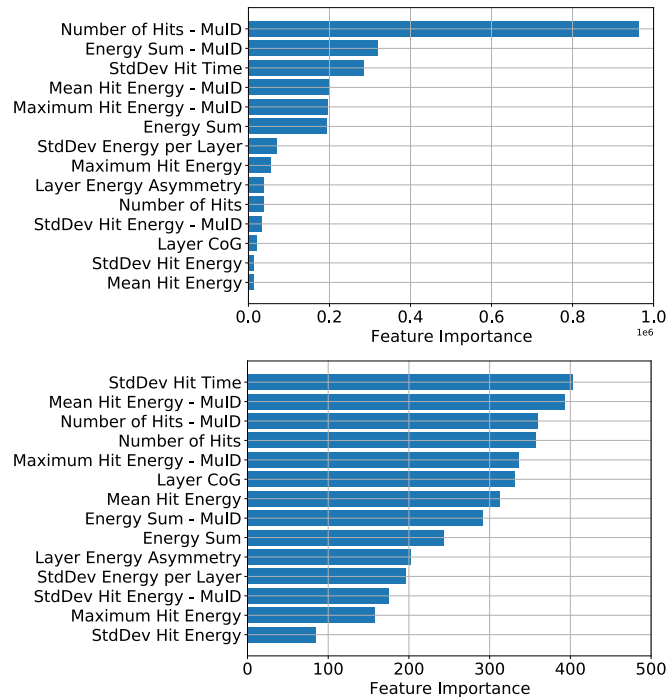

Figure 9.26: Gain (top) and split (bottom) importance of the input features for events above a momentum of $1\,\text{GeV}$.

9.6 Importance of the Particle Reconstruction Performance for the Neutrino Oscillation Measurements

Besides the near detectors main task, the characterization and monitoring of the neutrino flux, the unprecedented beam intensity can be exploited to improve the understanding of neutrino interactions and enhance the accuracy of the modeling. These models have an impact on the flux predictions as well as the flux measurement at the DUNE far detectors. The main observable at the far site, the electron neutrino appearance, is defined as the flux ratio for all neutrino energies E_ν and reads

$$P(\nu_\mu \to \nu_e) = \frac{\Phi_e^{FD}(E_\nu)}{\Phi_\mu^{ND}(E_\nu)}. \tag{9.9}$$

This effectively translates to an electron counting experiment at the far detector because it is the signature of a charged-current electron neutrino interaction inside the TPCs. The number of counted electrons however is a product of flux Φ, cross-section σ and detector acceptance ϵ and defined like

$$N_e^{FD}(E_\nu) = \Phi_e^{FD}(E_\nu) \cdot \sigma_e(E_\nu) \cdot \epsilon_e^{FD}(E_\nu). \tag{9.10}$$

Since the detectors don't measure the neutrino energy directly, the transformation D from neutrino energy to reconstructed energy E_{reco} has to be integrated out, so the number of reconstructed electrons including all detector effects reads

$$N_e^{FD}(E_{reco}) = \int dE_\nu D^{FD}\left(E_\nu \to E_{reco}\right) \cdot \Phi_e^{FD}(E_\nu) \cdot \sigma_e(E_\nu) \cdot \epsilon_e^{FD}(E_\nu). \tag{9.11}$$

All factors in this equation are subject to systematic uncertainties coming from imperfections in the neutrino interaction models, energy dependent detector effects, hardware and more. To cancel some of the detector related systematics in the final calculation of the ratio of electrons and muons, the DUNE near detector features liquid and gaseous argon targets to take data with the same material as the far detector. Parameterizing the number of muons in the near detector in a similar fashion, this ratio reads

$$\frac{N_e^{FD}(E_{reco})}{N_\mu^{ND}(E_{reco})} = \frac{\int dE_\nu D^{FD}\left(E_\nu \to E_{reco}\right) \cdot \Phi_e^{FD}(E_\nu) \cdot \sigma_e(E_\nu) \cdot \epsilon_e^{FD}(E_\nu)}{\int dE_\nu D^{ND}\left(E_\nu \to E_{reco}\right) \cdot \Phi_\mu^{ND}(E_\nu) \cdot \sigma_\mu(E_\nu) \cdot \epsilon_\mu^{ND}(E_\nu)}. \tag{9.12}$$

The important role of ND-GAr is constraining the $D^{ND}\left(E_\nu \to E_{reco}\right)$ which depends on the cross sections of all possible final states of the neutrino interactions. Since DUNEs energy range enables quasi-elastic (QE), resonant and deep-inelastic (DIS) neutrino scattering the variety of the final states is large. While QE and resonant channels feature a relatively clear signature in both liquid and gaseous argon detectors, especially the multi-hadron final states produced in DIS cannot be resolved in liquid argon because of the short mean-free-path of these particles. Since the first oscillation maximum is located at about $2.4\,\mathrm{GeV}$, these interactions are quite frequent. Accurate predictions for the momentum dependent far detector event rates require precise knowledge of
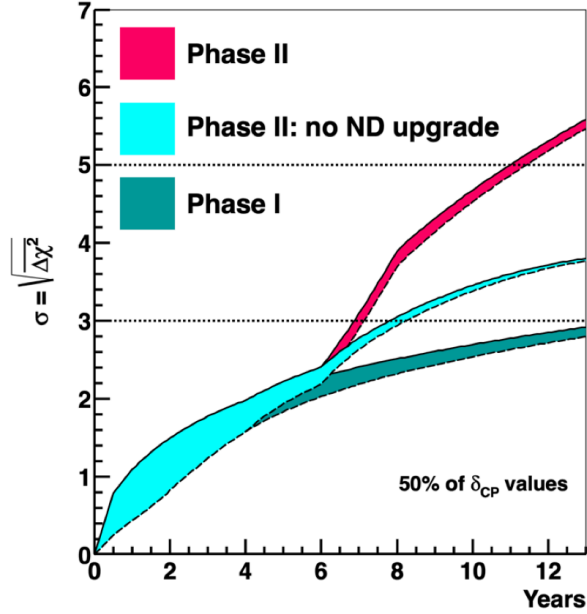
Figure 9.27: Predicted precision on the value of δ_{CP} for 50% of the parameter space versus the runtime of the experiment. Three different scenarios are shown corresponding to configurations of the experiment. Phase 1 consists of half of the far detectors fiducial mass and a near detector without ND-GAr. A Temporary Muon Spectrometer is placed instead. Phase 2 consists of the full far and near detector including ND-GAr. Additionally, the prediction for Phse2 without ND-GAr is shown. Taken from [90].

the kinematics and composition of these final states to model its response. Without these measurements DUNE will run into systematic limitations on the precision of the oscillation measurements, especially for the milestone of 5σ precision on 50% of the δ_{CP} values after 11 years of runtime.

ND-GAr is designed around this task. Its low density gaseous argon TPC allows the final state hadrons to propagate far enough from the vertex to be resolved. Calorimeters add additional capability to reconstruct neutral particles, like photons from neutral pion decays, or neutrons. As shown in this chapter, the calorimeter together with a muon identification (MuID) system can extend the TPCs limited range of separating muons and pions from 250 MeV to several GeV. This is vital in correctly identifying the leading muon from a DIS event as well as all pions produced as final states. Improved information on the cross-section and topology of these events can directly be implemented in Monte Carlo event generators like GENIE or NuWro. Figure 9.27 shows the expected precision on 50% of the δ_{CP} values for different Phases of the DUNE experiment [90]. The Phase 1 detectors feature half of the far detectors fiducual mass and ND-GAr is missing in the near detector. A temporary muon spectrometer (TMS) is placed after ND-LAr to catch exiting muons. Phase 2 features the full far detector as well as the upgraded near detector where ND-GAr replaces TMS. Additionally, the precision is shown for a case

that does not feature ND-GAr and consequantly does not reach the milestone of 5σ within the runtime of the experiment. ND-GAr with its high precision measurements is vital for this aspect of DUNEs physics program.

Chapter 10

Summary and Concluding Remarks

This thesis is focused on applications of highly granular calorimeters and their single cell timing capability in future high energy particle physics experiments. A calibration and analysis of test beam data recorded with the technological prototype of the CALICE AHCAL shows the capabilities of such a system, while an additional study investigates the limits of the timing properties of the SiPM-on-Tile technology. Based on this experience, a simulation study for the DUNE ND-GAr detector is conducted which focuses on the time of flight reconstruction of neutrons as well as muon–pion separation.

Due to the increased channel count in modern highly granular calorimeters the calibration procedures are increasingly difficult, involving millions of individual constants. The basic calibration procedure performed for the analyses within this thesis is developed in [91] and adapted in [64].The technological prototype of the AHCAL, which is the subject of this thesis, is equipped with a new generation of ASICs that introduced previously unknown effects in the time measurement. By extending the calibration procedure these effects have been quantified and subsequently corrected to achieve the expected timing behavior of the detector. A novel calibration scheme to correct occupancy related distortions on a channel level has been implemented. This is especially important for the time measurement within electromagnetic and hadronic particle showers since the occupancy is typically high. The achieved single channel resolution for MIPs in fast clock mode is 700±3 ps, therefor surpassing the design goal of 1 ns. A subsequent beam test study on the intrinsic, single channel time resolution of the SiPM-on-Tile technology, as it is used in the AHCAL, has been conducted at DESY. As a result, the achievable resolution for MIPs using the AHCAL scintillator is determined to be 466±4 ps. Since this value is at the same order of magnitude as the AHCAL MIP time resolution, improving the intrinsic properties of this technology alone does not improve the prototypes performance. The read out and electronics have to be adapted as well to significantly increase the resolution of the full system. Furthermore, this dedicated study provided hints on a dependence of the time resolution on the geometry of the scintillator tile. This was recognized by comparing the response of tiles with similar light yield but different size. Exploiting the large recorded data set the timing performance is also investigated in an energy resolved study. Without distortions from calibration or electronics the maximum achievable resolution with the AHCAL scintillator is 73 ps for the highest energies. Based on this results, the study was extended in the scope of a separate master thesis providing detailed experimental studies on individual processes

influencing the time response [75].

The calorimeters response to electrons and hadrons has been investigated in a separate study. The width of the hit time distribution for electromagnetic showers is 6.6 ns. While these showers are expected to evolve on a sub-nanosecond timescale, the residual effects of the occupancy related distortions decrease the accuracy of the measurement. This poses a problem, especially for the investigation of the time structure of hadronic showers. Since a multitude of low energetic processes like elastic neutron scattering or capture and spallation reactions evolve on a timescale of several tens of nanoseconds, they are shadowed by detector effects in the time domain. This part of the time signature of hadronic showers however is especially interesting for software compensation algorithms since the time information correlates with the visible and, most importantly, the invisible energy created in the respective processes with strong neutron contribution [92]. The late components of the hadronic shower evolving over several 100 ns to 1 μs are reliably resolved and appear as the expected tail in the hit time distribution. As already shown in [64] Monte Carlo simulation with FTFP–BERT–HP overestimates this tail slightly. Also the contribution of hits later than 100 ns does not match with the Monte Carlo data set. In order to successfully use the unprecedented channel count of these novel calorimeters also in the time measurement, several improvements are still required. While the calibration procedures are working as expected and can be applied to a full scale detector, the read out has to be improved in order to profit from the intrinsically fast SiPM-on-Tile technology. The limitations introduced by the occupancy related effects are not recoverable to the full extent. Since not only the mean of the hit times is shifted depending on the ASIC occupancy, but also the spread of the distribution is increased, an event by event correction cannot fully compensate this. A correction on the hit level will break the correlation of hit time and energy deposition, hence the usage of such a procedure is out of question. Ultimately this issues have to be addressed in hardware.

The second aspect of this thesis addresses the applicability of highly granular detectors in the field of future long baseline neutrino experiments. Similar to future accelerator experiments the need for precise particle separation in high background environments poses comparable challenges between the two fields. The CDR design of the ND–GAr subsystem of the DUNE ND features a highly granular calorimeter inspired by the CALICE AHCAL. The simulation studies conducted in the course of this work investigate the kinetic energy measurement of neutrons by time of flight as well as the separation of muons and pions.

Since the high pressure gaseous argon TPC in the center of ND–GAr is not capable of reconstructing neutral particles, they have to be picked up by the calorimeter. In DIS events a large number of secondary neutrons can be produced which carry a non-negligible fraction of total energy in the reaction. Typically these neutrons interact softly with the detector without inducing a particle shower, therefore causing a huge mismatch between visible and true kinetic energy. Since the majority of them are not fully relativistic a time-of-flight reconstruction is feasible. The test beam studies on the SiPM-on-Tile technology serve as an input to the simulation for a realistic parameterization of the timing

behavior. The study shows an energy resolution of between 5% and 10% for neutron energies up to 230 MeV measured with the 90% smallest interval of the reconstructed energy distribution. This interval already includes the most probable kinetic energy. For energies up to 1 GeV and higher the resolution drops to about 40% due to the increasing relativity of the neutrons. This can only be countered with a better time resolution of the calorimeter. The cumulative resolution obtained for the studied energy spectrum up to about 1.3 GeV is 7.37±0.03 MeV based on the 68% smallest interval and 42.2±0.1 MeV based on the 90% smallest interval. This performance can be increased by enhancing the timing properties of the system but since the majority of the final state momentum is distributed among charged particles this may not be necessary. Furthermore, increasing the scintillator thickness for faster timing and higher neutron cross section also decreases the depth in collision length of the system and may compromise the overall stopping power for hadrons. A sufficient stopping power is required for hadron identification as shown in a separate study.

To fulfill the near detectors primary task of characterizing the flux and composition of the initial neutrino beam, it is absolutely vital to correctly reconstruct the charge of the final state leptons in CC reactions. In the majority of RES and DIS interactions a pion of opposite charge is produced. The rest mass of those is comparable to the muons rest mass and therefore the energy loss in the TPC is similar. This quantity, however, is used for particle identification, so for momenta exceeding 250 MeV the separation of muon and pion gets challenging. The calorimeter and muon tracker exploit the fact that, unlike the muon, the pion is a hadron and can therefore undergo a variety of hadronic interactions. The requirement is a sufficient budget of dense material, preferably metal, throughout the detector to increase the chance of hadronic interactions. The classification of muons and pions is studied with a BDT using calorimetric variables based on energy and time obtained with the calorimeter and MuID. Applied to a data set featuring a realistic ratio and momentum distribution of muons and pions, the BDT achieved a muon purity exceeding 90% for momenta exceeding 1 GeV. The pion purity lies between 80% and 90% for the studied momentum range. The classification threshold of the BDT was set to 50%. Above 1 GeV the muon and pion efficiency are reliably above 96% and 75%, respectively. A study for different configurations of the MuID underlines the necessity of this system. Excluding it from the classification deteriorates the overall pion efficiency by about 10% and the purity by about 20%. Only including the outermost layer almost recovers this. Consequently, the MuID layers gain importance with increasing material budget in front of them. This offers potential for cost optimization since multiple layers of MuID also require a segmented return yoke of the magnet and therefore drive the complexity of the system. In general, the calorimeter combined with some form of MuID is absolute crucial for the success of the detector since it extends the muon identification performance to the GeV range to cover the first and second oscillation maximum. The correct association of charge and particle is vital for the quantification of the beam contamination with different neutrino flavors. Furthermore, this ability aids the role of ND–GAr as high precision machine capable of the reconstruction of the full final state of the neutrino interaction. This will provide unprecedented measurement on multi-hadron

final states and neutrino–nucleus cross sections. Knowledge of the energy distribution of this final states also helps in constraining the mismatch of true and visible energy in the far detector, since the liquid argon TPCs are blind to the low energy particles.

Chapter 11

Outlook

With the development of the AHCAL technological prototype a major step has been taken towards a full scale detector. This thesis should serve as a report of the status of timing in this system and provide directions for further improvement. While the MIP timing goals are achieved the performance for showers, especially in the high occupancy regions, needs to be improved. Novel read out chips like the KLAUS ASIC [93] are promising candidates implementing a different kind of TDC for time measurement.

Timing is a valuable ingredient for the energy reconstruction of hadronic showers as discussed in [64]. Especially the classification of processes inside the showers offers a playground for novel machine learning applications [94] exploiting correlations of time, energy and position of individual hits using the 5-dimensional information. As shown in this thesis, the simulation of particle showers also profits from new insights in their time evolution to increase the performance of existing models. Machine learning approaches to event simulation [95] are an interesting new concept directly profiting from precise experimental data. The AHCAL currently undergoes further beam test campaigns to record particle showers with the fast ILC mode. These data sets will explore the their time evolution with higher accuracy and may provide better understanding of the currently still relatively unexplored region of a few ns to order 10 ns after shower start. The first large scale detector utilizing the SiPM-On-Tile technology will be the CMS HGCAL upgrade for HL-LHC. This system aims at at time resolution of 50 ps for electromagnetic showers [96]. This is also necessary to cope withe the pile-up of collisions at the upgraded collider.

As discussed previously, high granularity is also beneficial for machine learning applications at long baseline neutrino experiments like DUNE. The particle identification study presented in this thesis utilizes basic calorimetric variables and already achieves efficiencies and purities above 90% for the major part of the momentum region. More complex algorithms like convolutional neural networks [97] and deep-learning [98] are promising approaches to extract features from image–like, naturally voxelized data.

Currently ongoing studies target the mechanical implementation of the calorimeter in the existing ND-GAr design as well as detailed studies on the timing behavior of scintillating tiles. The properties of elongated scintillating strips are especially interesting since those will make up a large part of the planned calorimeter design. As discussed earlier, the energy range in which the time-of-flight reconstruction performs sufficiently well is directly related to the time resolution of the respective area in the detector. This requires a deep understanding of the interplay between light yield and geometric effects in order

to optimize for the detectors main tasks. A master thesis at the Max-Planck-Institute for Physics currently addresses these questions using the well understood test beam setup already discussed in the present thesis.

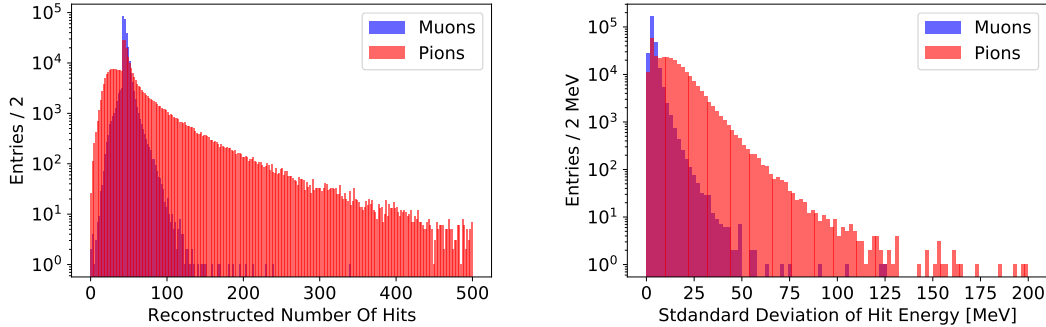# Appendix A

Distributions of Additional BDT Features

Figure A.1: The left figure shows the reconstructed number of hits in the calorimeter, the right one shows the standard deviation of the hit energy.
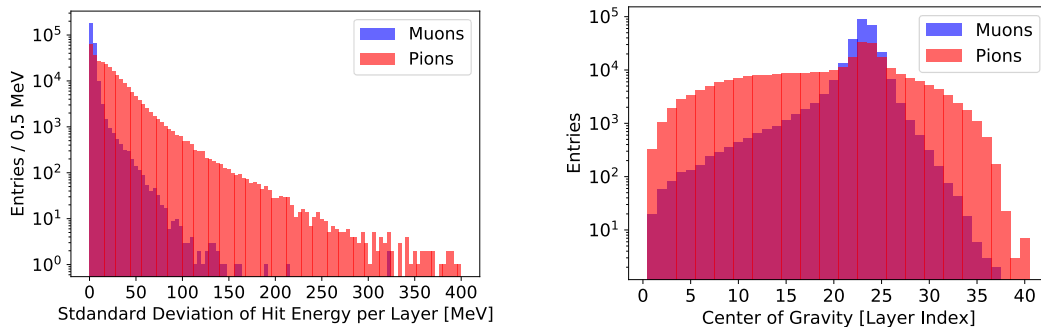
Figure A.2: The left figure shows the standard deviation of the reconstructed energy per layer, the right figure shows the layer number of the center of gravity.
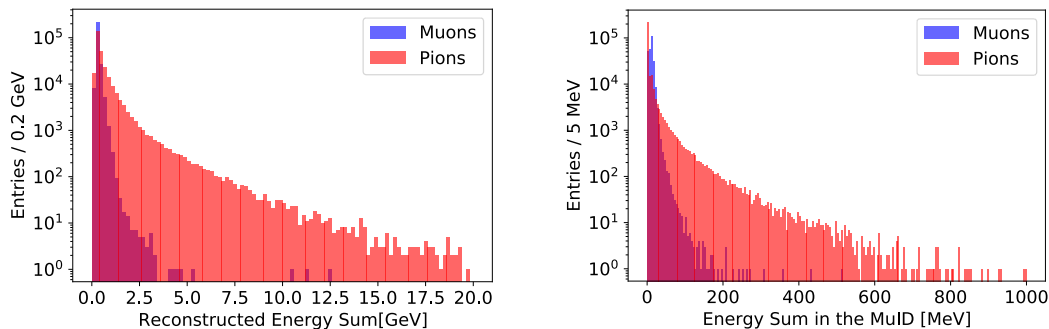
Figure A.3: Reconstructed energy sum in calorimeter (left) and MuID (right).
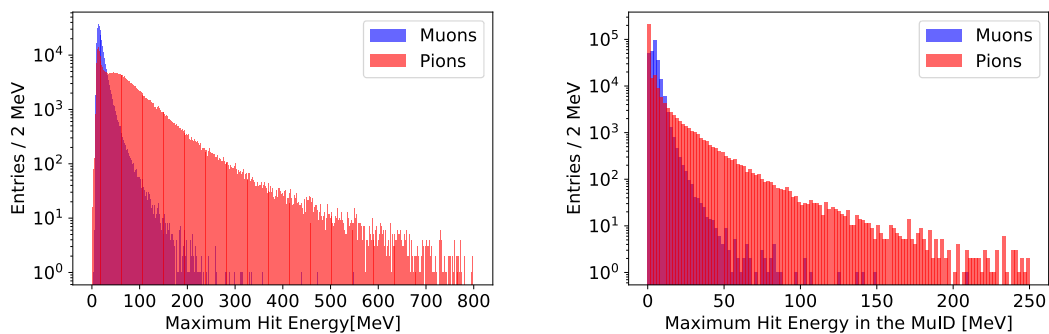
Figure A.4: Maximum hit energy in calorimeter (left) and MuID (right).
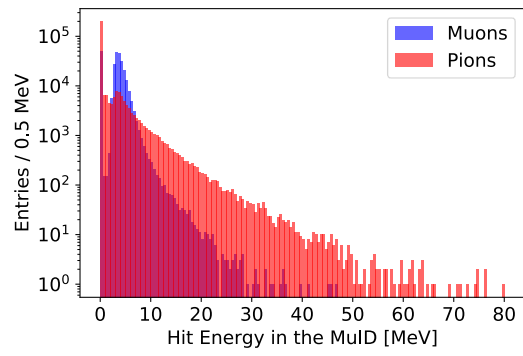
Figure A.5: Mean hit energy in MuID (right).

Bibliography

[1] B. Hübner et al. "Test of a scintillating-fiber calorimeter for photons with energies below 1 GeV". In: *Nuclear Instruments and Methods in Physics Research Section A: Accelerators, Spectrometers, Detectors and Associated Equipment* 382.3 (1996), pp. 413–418. ISSN: 0168-9002. DOI: https://doi.org/10.1016/S0168-9002(96)00815-7. URL: https://www.sciencedirect.com/science/article/pii/S0168900296008157.

[2] D.W. Hertzog et al. "A high-resolution lead /scintillating fiber electromagnetic calorimeter". In: *Nuclear Instruments and Methods in Physics Research Section A: Accelerators, Spectrometers, Detectors and Associated Equipment* 294.3 (1990), pp. 446–458. ISSN: 0168-9002. DOI: https://doi.org/10.1016/0168-9002(90)90285-E. URL: https://www.sciencedirect.com/science/article/pii/016890029090285E.

[3] Peter Jenni et al. *The high resolution spaghetti hadron calorimeter: proposal*. Tech. rep. Geneva: CERN, 1987. URL: https://cds.cern.ch/record/181281.

[4] Felix Sefkow and Frank Simon. "A highly granular SiPM-on-tile calorimeter prototype". In: *J. Phys.: Conf. Ser.* 1162 (Aug. 2018). 5 pages, 5 figures, proceedings of CALOR 2018, Eugene, OR, USA, May 2018, 012012. 5 p. DOI: 10.1088/1742-6596/1162/1/012012. arXiv: 1808.09281. URL: http://cds.cern.ch/record/2636699.

[5] The CALICE collaboration et al. "Construction and commissioning of the CALICE analog hadron calorimeter prototype". In: *Journal of Instrumentation* 5.05 (May 2010), P05004–P05004. ISSN: 1748-0221. DOI: 10.1088/1748-0221/5/05/p05004. URL: http://dx.doi.org/10.1088/1748-0221/5/05/P05004.

[6] Chris Adolphsen et al. *The International Linear Collider Technical Design Report*. Tech. rep. arXiv:1306.6328. Comments: See also http://www.linearcollider.org/ILC/TDR . The full list of signatories is inside the Report. Geneva, June 2013. URL: https://cds.cern.ch/record/1601969.

[7] Philip T. Burrows et al. "The Compact Linear Collider (CLIC) 2018 summary report". In: *CERN Yellow Reports: Monographs* (2018). DOI: 10.23731/CYRM-2018-002.

[8] S. Chatrchyan et al. "Observation of a new boson at a mass of 125 GeV with the CMS experiment at the LHC". In: *Physics Letters B* 716 (Sept. 2012). DOI: 10.1016/j.physletb.2012.08.021. URL: https://doi.org/10.1016%2Fj.physletb.2012.08.021.

[9] G. Aad et al. "Observation of a new particle in the search for the Standard Model Higgs boson with the ATLAS detector at the LHC". In: *Physics Letters B* 716 (Sept. 2012). DOI: 10.1016/j.physletb.2012.08.020. URL: https://doi.org/10.1016%2Fj.physletb.2012.08.020.

[10] Peter W. Higgs. "Broken Symmetries and the Masses of Gauge Bosons". In: *Phys. Rev. Lett.* 13 (16 Oct. 1964), pp. 508–509. DOI: 10.1103/PhysRevLett.13.508. URL: https://link.aps.org/doi/10.1103/PhysRevLett.13.508.

[11] Manuel Reichert et al. "Probing baryogenesis through the Higgs boson self-coupling". In: *Phys. Rev. D* 97.7 (2018), p. 075008. DOI: 10.1103/PhysRevD.97.075008. arXiv: 1711.00019 [hep-ph].

[12] Giorgio Arcadi, Abdelhak Djouadi, and Marumi Kado. "The Higgs-portal for dark matter: effective field theories versus concrete realizations". In: *The European Physical Journal C* 81.7 (2021), p. 653. DOI: 10.1140/epjc/s10052-021-09411-2. URL: https://doi.org/10.1140/epjc/s10052-021-09411-2.

[13] M. Cepeda et al. *Higgs Physics at the HL-LHC and HE-LHC.* 2019. DOI: 10.48550/ARXIV.1902.00134. URL: https://arxiv.org/abs/1902.00134.

[14] Howard E. Haber. *Non-Minimal Higgs Sectors: The Decoupling Limit and its Phenomenological Implications,* 1995. DOI: 10.48550/ARXIV.HEP-PH/9501320. URL: https://arxiv.org/abs/hep-ph/9501320.

[15] Howard Baer et al. *The International Linear Collider Technical Design Report - Volume 2: Physics.* 2013. arXiv: 1306.6352 [hep-ph].

[16] P.N. Burrows et al. *The Compact Linear Collider (CLIC) - 2018 Summary Report.* Ed. by P.N. Burrows. Vol. 2. CERN Yellow Reports: Monographs. Dec. 2018. DOI: 10.23731/CYRM-2018-002. URL: http://cds.cern.ch/record/2652188.

[17] Henning Bahl et al. "HL-LHC and ILC sensitivities in the hunt for heavy Higgs bosons". In: *The European Physical Journal C* 80.10 (2020), p. 916. DOI: 10.1140/epjc/s10052-020-08472-z. URL: https://doi.org/10.1140/epjc/s10052-020-08472-z.

[18] Savas Dimopoulos and Howard Georgi. "Softly broken supersymmetry and SU(5)". In: *Nuclear Physics B* 193.1 (1981), pp. 150–162. ISSN: 0550-3213. DOI: https://doi.org/10.1016/0550-3213(81)90522-8. URL: https://www.sciencedirect.com/science/article/pii/0550321381905228.

[19] Michael Benedikt et al. *FCC-ee: The Lepton Collider: Future Circular Collider Conceptual Design Report Volume 2. Future Circular Collider.* Tech. rep. CERN-ACC-2018-0057. 2. Geneva: CERN, Dec. 2018. DOI: 10.1140/epjst/e2019-900045-4. URL: http://cds.cern.ch/record/2651299.

[20] The CEPC Study Group. *CEPC Conceptual Design Report: Volume 1 - Accelerator.* 2018. arXiv: 1809.00285 [physics.acc-ph].

[21] D. Iwanenko and I. Pomeranchuk. "On the Maximal Energy Attainable in a Betatron". In: *Phys. Rev.* 65 (11-12 June 1944), pp. 343–343. DOI: `10.1103/PhysRev.65.343`. URL: `https://link.aps.org/doi/10.1103/PhysRev.65.343`.

[22] "The International Linear Collider Technical Design Report - Volume 3.II: Accelerator Baseline Design". In: (June 2013). Ed. by Chris Adolphsen et al. arXiv: `1306.6328 [physics.acc-ph]`.

[23] "XFEL: The European X-Ray Free-Electron Laser. Technical design report". In: (July 2006). Ed. by Massimo Altarelli et al. DOI: `10.3204/DESY_06-097`.

[24] Frank Simon. *Scanning Strategies at the Top Threshold at ILC*. 2020. arXiv: `1902.07246 [hep-ex]`.

[25] Felix Sefkow et al. "Experimental tests of particle flow calorimetry". In: *Reviews of Modern Physics* 88.1 (Feb. 2016). ISSN: 1539-0756. DOI: `10.1103/revmodphys.88.015003`. URL: `http://dx.doi.org/10.1103/RevModPhys.88.015003`.

[26] Y. Fukuda et al. "Evidence for Oscillation of Atmospheric Neutrinos". In: *Phys. Rev. Lett.* 81 (8 Aug. 1998), pp. 1562–1567. DOI: `10.1103/PhysRevLett.81.1562`. URL: `https://link.aps.org/doi/10.1103/PhysRevLett.81.1562`.

[27] B. Abi et al. "Volume I. Introduction to DUNE". In: *Journal of Instrumentation* 15.08 (Aug. 2020), T08008–T08008. DOI: `10.1088/1748-0221/15/08/t08008`. URL: `https://doi.org/10.1088/1748-0221/15/08/t08008`.

[28] B. Abi et al. *Deep Underground Neutrino Experiment (DUNE), Far Detector Technical Design Report, Volume II: DUNE Physics*. 2020. arXiv: `2002.03005 [hep-ex]`.

[29] B. Pontecorvo. "Neutrino Experiments and the Problem of Conservation of Leptonic Charge". In: *Sov. Phys. JETP* 26 (1968), pp. 984–988.

[30] Q. R. Ahmad et al. "Measurement of the Rate of $\nu_e + d \to p + p + e^-$ Interactions Produced by ^8B Solar Neutrinos at the Sudbury Neutrino Observatory". In: *Phys. Rev. Lett.* 87 (7 July 2001), p. 071301. DOI: `10.1103/PhysRevLett.87.071301`. URL: `https://link.aps.org/doi/10.1103/PhysRevLett.87.071301`.

[31] Ziro Maki, Masami Nakagawa, and Shoichi Sakata. "Remarks on the Unified Model of Elementary Particles". In: *Progress of Theoretical Physics* 28.5 (Nov. 1962), pp. 870–880. ISSN: 0033-068X. DOI: `10.1143/PTP.28.870`. eprint: `https://academic.oup.com/ptp/article-pdf/28/5/870/5258750/28-5-870.pdf`. URL: `https://doi.org/10.1143/PTP.28.870`.

[32] C Giunti and Chung W. Kim. *Fundamentals of Neutrino Physics and Astrophysics*. Oxford University Press, 2007. ISBN: 978-0-19-850871-7.

[33] R. Acciarri et al. *Long-Baseline Neutrino Facility (LBNF) and Deep Underground Neutrino Experiment (DUNE) Conceptual Design Report Volume 2: The Physics Program for DUNE at LBNF*. 2016. arXiv: `1512.06148 [physics.ins-det]`.

[34] L. Wolfenstein. "Neutrino oscillations in matter". In: *Phys. Rev. D* 17 (9 May 1978), pp. 2369–2374. DOI: `10.1103/PhysRevD.17.2369`. URL: `https://link.aps.org/doi/10.1103/PhysRevD.17.2369`.

[35] R.B. Patterson. "Prospects for Measurement of the Neutrino Mass Hierarchy". In: *Annual Review of Nuclear and Particle Science* 65.1 (2015), pp. 177–192. DOI: `10.1146/annurev-nucl-102014-021916`. URL: `https://doi.org/10.1146/annurev-nucl-102014-021916`.

[36] Pablo F. de Salas et al. "Neutrino Mass Ordering from Oscillations and Beyond: 2018 Status and Future Prospects". In: *Frontiers in Astronomy and Space Sciences* 5 (2018). ISSN: 2296-987X. DOI: `10.3389/fspas.2018.00036`. URL: `https://www.frontiersin.org/article/10.3389/fspas.2018.00036`.

[37] Mattias Blennow and Alexei Yu. Smirnov. "Neutrino Propagation in Matter". In: *Advances in High Energy Physics* 2013 (2013), pp. 1–33. DOI: `10.1155/2013/972485`. URL: `https://doi.org/10.1155%2F2013%2F972485`.

[38] V. Papadimitriou et al. *Design Of The LBNF Beamline*. 2017. arXiv: `1704.04471 [physics.acc-ph]`.

[39] A. Abed Abud et al. *Deep Underground Neutrino Experiment (DUNE) Near Detector Conceptual Design Report*. 2021. arXiv: `2103.13910 [physics.ins-det]`.

[40] Lorenz Emberger. "Simulation Studies of a Highly Granular Electromagnetic Calorimeter for the DUNE Near Detector." MA thesis. Max-Planck-Institute for Physics, 2018.

[41] Paolo Franzini and Matthew Moulson. "The Physics of DAΦNE and KLOE". In: *Annual Review of Nuclear and Particle Science* 56.1 (Nov. 2006), pp. 207–251. DOI: `10.1146/annurev.nucl.56.080805.140459`. URL: `https://doi.org/10.1146%2Fannurev.nucl.56.080805.140459`.

[42] Cristovao Vilela. *DUNE PRISM*. Dec. 2018. DOI: `10.5281/zenodo.2642370`. URL: `https://doi.org/10.5281/zenodo.2642370`.

[43] DUNE. "Private communication". In: ().

[44] H. Bethe, J. Ashkin, and H. Staub. *Experimental Nuclear Physics*. Ed. by E. Segre. Vol. 1. Wiley and Sons, 1953.

[45] R. L. Workman et al. "Review of Particle Physics". In: *PTEP* 2022 (2022), p. 083C01. DOI: `10.1093/ptep/ptac097`.

[46] Claus Grupen and Boris Shwartz. *Particle Detectors*. Cambridge Monographs on Particle Physics, Nuclear Physics and Cosmology, 2008.

[47] R. Wigmans. *Calorimetry: Energy measurement in particle physics*. Jan. 2018, pp. 1–854. DOI: `10.1093/oso/9780198786351.001.0001`.

[48] Arthur H. Compton. "A Quantum Theory of the Scattering of X-rays by Light Elements". In: *Phys. Rev.* 21 (5 May 1923), pp. 483–502. DOI: `10.1103/PhysRev.21.483`. URL: `https://link.aps.org/doi/10.1103/PhysRev.21.483`.

[49] T.W. Armstrong. *The Intranuclear-Cascade-Evaporation Model*. Ed. by W.R. Nelson and T.M. Jenkins. Vol. 3. Ettore Majorana International Science Series (Physical Sciences). Springer, Boston, MA, 1980.

[50] Tejinder S Virdee. *Calorimetry*. Tech. rep. Geneva: CERN, 1999. URL: `http://cds.cern.ch/record/529421`.

[51] Lev Davidovich Landau. "On the energy loss of fast particles by ionization". In: *J. Phys.* 8 (1944), pp. 201–205. URL: `https://cds.cern.ch/record/216256`.

[52] Frank Simon. "Silicon photomultipliers in particle and nuclear physics". In: *Nuclear Instruments and Methods in Physics Research Section A: Accelerators, Spectrometers, Detectors and Associated Equipment* 926 (May 2019), pp. 85–100. DOI: `10.1016/j.nima.2018.11.042`. URL: `https://doi.org/10.1016%2Fj.nima.2018.11.042`.

[53] The CALICE collaboration et al. "Design and electronics commissioning of the physics prototype of a Si-W electromagnetic calorimeter for the International Linear Collider". In: *Journal of Instrumentation* 3.08 (Aug. 2008), P08001–P08001. DOI: `10.1088/1748-0221/3/08/p08001`. URL: `https://doi.org/10.1088%2F1748-0221%2F3%2F08%2Fp08001`.

[54] G. Baulieu et al. *Construction and commissioning of a technological prototype of a high-granularity semi-digital hadronic calorimeter*. 2015. DOI: `10.48550/ARXIV.1506.05316`. URL: `https://arxiv.org/abs/1506.05316`.

[55] CALICE Collaboration et al. "Construction and Response of a Highly Granular Scintillator-based Electromagnetic Calorimeter". In: (2017). DOI: `10.48550/ARXIV.1707.07126`. URL: `https://arxiv.org/abs/1707.07126`.

[56] M.A. Thomson. "Particle flow calorimetry and the PandoraPFA algorithm". In: *Nuclear Instruments and Methods in Physics Research Section A: Accelerators, Spectrometers, Detectors and Associated Equipment* 611.1 (Nov. 2009), pp. 25–40. DOI: `10.1016/j.nima.2009.09.009`. URL: `https://doi.org/10.1016%2Fj.nima.2009.09.009`.

[57] M. Bouchel et al. "SPIROC (SiPM Integrated Read-Out Chip): Dedicated very front-end electronics for an ILC prototype hadronic calorimeter with SiPM read-out". In: *JINST* 6 (2011), p. C01098. DOI: `10.1088/1748-0221/6/01/C01098`.

[58] Yong Liu et al. *A Design of Scintillator Tiles Read Out by Surface-Mounted SiPMs for a Future Hadron Calorimeter*. 2015. arXiv: `1512.05900 [physics.ins-det]`.

[59] F. Simon and C. Soldner. "Uniformity studies of scintillator tiles directly coupled to SiPMs for imaging calorimetry". In: *Nuclear Instruments and Methods in Physics Research Section A: Accelerators, Spectrometers, Detectors and Associated Equipment* 620.2-3 (Aug. 2010), pp. 196–201. ISSN: 0168-9002. DOI: `10.1016/j.nima.2010.03.142`. URL: `http://dx.doi.org/10.1016/j.nima.2010.03.142`.

[60] Mathias Reinecke. "Power pulsing of the CALICE tile hadron calorimeter". In: *2016 IEEE Nuclear Science Symposium, Medical Imaging Conference and Room-Temperature Semiconductor Detector Workshop (NSS/MIC/RTSD)*. 2016, pp. 1–6. DOI: `10.1109/NSSMIC.2016.8069748`.

[61] Omega. *SPIROC2 User Guide (Draft)*. Feb. 2009.

[62] Daniel Heuchel. "Particle Flow Studies with Highly Granular Calorimeter Data". PhD thesis. Kirchhoff Institute for Physics, June 2022. DOI: `10.11588/heidok.00031794`.

[63] J. Kvasnicka. "Data acquisition system for the CALICE AHCAL calorimeter". In: *Journal of Instrumentation* 12.03 (Mar. 2017), pp. C03043–C03043. DOI: `10.1088/1748-0221/12/03/c03043`. URL: `https://doi.org/10.1088%2F1748-0221%2F12%2F03%2Fc03043`.

[64] Christian Graf. "Towards Precision Time and Energy Measurements in Highly Granular Hadronic Calorimeters". Dissertation. München: Technische Universität München, 2020.

[65] Markus Frank et al. *AIDASoft/DD4hep*. webpage: http://dd4hep.cern.ch/. Oct. 2018. DOI: `10.5281/zenodo.592244`. URL: `https://doi.org/10.5281/zenodo.592244`.

[66] URL: `https://ilcsoft.desy.de/portal/software_packages/marlin/`.

[67] S. Agostinelli et al. "Geant4—a simulation toolkit". In: *Nuclear Instruments and Methods in Physics Research Section A: Accelerators, Spectrometers, Detectors and Associated Equipment* 506.3 (2003), pp. 250–303. ISSN: 0168-9002. DOI: `https://doi.org/10.1016/S0168-9002(03)01368-8`. URL: `https://www.sciencedirect.com/science/article/pii/S0168900203013688`.

[68] Aatos Heikkinen, Nikita Stepanov, and J. P. Wellisch. *Bertini intra-nuclear cascade implementation in Geant4*. 2003. DOI: `10.48550/ARXIV.NUCL-TH/0306008`. URL: `https://arxiv.org/abs/nucl-th/0306008`.

[69] G. Folger and J. P. Wellisch. *String Parton Models in Geant4*. 2003. DOI: `10.48550/ARXIV.NUCL-TH/0306007`. URL: `https://arxiv.org/abs/nucl-th/0306007`.

[70] Huong Lan Tran et al. "Software compensation in particle flow reconstruction". In: *The European Physical Journal C* 77.10 (Oct. 2017). DOI: `10.1140/epjc/s10052-017-5298-3`. URL: `https://doi.org/10.1140%2Fepjc%2Fs10052-017-5298-3`.

[71] R. Diener et al. "The DESY II test beam facility". In: *Nuclear Instruments and Methods in Physics Research Section A: Accelerators, Spectrometers, Detectors and Associated Equipment* 922 (2019), pp. 265–286. ISSN: 0168-9002. DOI: `https://doi.org/10.1016/j.nima.2018.11.133`. URL: `https://www.sciencedirect.com/science/article/pii/S0168900218317868`.

136

[72] Hendrik Uwe Windel. "CLAWS - An injection background monitoring system for the second and third phase of the SuperKEKB commissioning". Dissertation. München: Technische Universität München, 2021.

[73] Kazunori Akai, Kazuro Furukawa, and Haruyo Koiso. "SuperKEKB collider". In: *Nuclear Instruments and Methods in Physics Research Section A: Accelerators, Spectrometers, Detectors and Associated Equipment* 907 (Nov. 2018), pp. 188–199. DOI: 10.1016/j.nima.2018.08.017. URL: https://doi.org/10.1016%2Fj.nima.2018.08.017.

[74] Malinda de Silva and F. Simon. "Effects of misalignment on response uniformity of SiPM-on-tile technology for highly granular calorimeters". In: *Journal of Instrumentation* 15 (June 2020), P06030–P06030. DOI: 10.1088/1748-0221/15/06/P06030.

[75] F. Hummer. "Intrinsic Time Resolution of Plastic Scintillator Tiles with SiPM Readout for Highly Granular Calorimeters". MA thesis. Max-Planck-Institute for Physics, 2022.

[76] J. A. Formaggio and G. P. Zeller. "From eV to EeV: Neutrino cross sections across energy scales". In: *Reviews of Modern Physics* 84.3 (Sept. 2012), pp. 1307–1341. ISSN: 1539-0756. DOI: 10.1103/revmodphys.84.1307. URL: http://dx.doi.org/10.1103/RevModPhys.84.1307.

[77] Lorenz Emberger and Frank Simon. "A highly granular calorimeter concept for long baseline near detectors". In: *Journal of Physics: Conference Series* 1162 (Jan. 2019), p. 012033. DOI: 10.1088/1742-6596/1162/1/012033. URL: https://doi.org/10.1088%2F1742-6596%2F1162%2F1%2F012033.

[78] Andrew Mastbaum. "The DUNE Near Detector". In: *PoS* EPS-HEP2021 (2022), p. 798. DOI: 10.22323/1.398.0798.

[79] C. Green et al. "The Art Framework". In: *J. Phys. Conf. Ser.* 396 (2012). Ed. by Michael Ernst et al., p. 022020. DOI: 10.1088/1742-6596/396/2/022020.

[80] C. Andreopoulos et al. "The GENIE Neutrino Monte Carlo Generator". In: *Nucl. Instrum. Meth. A* 614 (2010), pp. 87–104. DOI: 10.1016/j.nima.2009.12.009. arXiv: 0905.2517 [hep-ph].

[81] J. Allison et al. "Geant4 developments and applications". In: *IEEE Transactions on Nuclear Science* 53.1 (2006), pp. 270–278. DOI: 10.1109/TNS.2006.869826.

[82] J. Allison et al. "Recent developments in Geant4". In: *Nuclear Instruments and Methods in Physics Research Section A: Accelerators, Spectrometers, Detectors and Associated Equipment* 835 (2016), pp. 186–225. ISSN: 0168-9002. DOI: https://doi.org/10.1016/j.nima.2016.06.125. URL: https://www.sciencedirect.com/science/article/pii/S0168900216306957.

[83] Rene Brun et al. *root-project/root: v6.18/02*. Version v6-18-02. Aug. 2019. DOI: 10.5281/zenodo.3895860. URL: https://doi.org/10.5281/zenodo.3895860.

[84] G. Enderlein. "Wilks, S. S.: Mathematical Statistics. J. Wiley and Sons, New York–London 1962; 644 S., 98 s". In: *Biometrische Zeitschrift* 6 (1964), pp. 214–215.

[85] Thomas M. Mitchell. *Machine Learning.* 1st ed. USA: McGraw-Hill, Inc., 1997. ISBN: 0070428077.

[86] URL: https://lightgbm.readthedocs.io.

[87] T. Golan, J.T. Sobczyk, and J. Żmuda. "NuWro: the Wrocław Monte Carlo Generator of Neutrino Interactions". In: *Nuclear Physics B - Proceedings Supplements* 229-232 (2012). Neutrino 2010, p. 499. ISSN: 0920-5632. DOI: https://doi.org/10.1016/j.nuclphysbps.2012.09.136. URL: https://www.sciencedirect.com/science/article/pii/S0920563212003532.

[88] Y. Hayato. "Neut". In: *Nuclear Physics B - Proceedings Supplements* 112.1 (2002), pp. 171–176. ISSN: 0920-5632. DOI: https://doi.org/10.1016/S0920-5632(02)01759-0. URL: https://www.sciencedirect.com/science/article/pii/S0920563202017590.

[89] S. Dytman et al. "Comparison of validation methods of simulations for final state interactions in hadron production experiments". In: *Physical Review D* 104.5 (Sept. 2021). ISSN: 2470-0029. DOI: 10.1103/physrevd.104.053006. URL: http://dx.doi.org/10.1103/PhysRevD.104.053006.

[90] DUNE Collaboration et al. *Snowmass Neutrino Frontier: DUNE Physics Summary.* 2022. DOI: 10.48550/ARXIV.2203.06100. URL: https://arxiv.org/abs/2203.06100.

[91] Eldwan Brianne. "Time development of hadronic showers in a Highly Granular Analog Hadron Calorimeter". Dissertation, Universität Hamburg, 2018. Dissertation. Hamburg: Universität Hamburg, 2018, p. 259. DOI: 10.3204/PUBDB-2018-02769. URL: https://bib-pubdb1.desy.de/record/408316.

[92] Frank Simon. *The Time Structure of Hadronic Showers in Imaging Calorimeters with Scintillator and RPC Readout.* 2013. DOI: 10.48550/ARXIV.1308.6395. URL: https://arxiv.org/abs/1308.6395.

[93] Zhenxiong Yuan et al. "KLauS: A Low-power SiPM Readout ASIC for Highly Granular Calorimeters". In: *2019 IEEE Nuclear Science Symposium and Medical Imaging Conference (NSS/MIC).* 2019, pp. 1–4. DOI: 10.1109/NSS/MIC42101.2019.9059888.

[94] Erik Buhmann. "Deep learning based energy reconstruction for the CALICE AHCAL". MA thesis. Universität Hamburg, 2019.

[95] Martin Erdmann, Jonas Glombitza, and Thorben Quast. "Precise Simulation of Electromagnetic Calorimeter Showers Using a Wasserstein Generative Adversarial Network". In: *Computing and Software for Big Science* 3.1 (Jan. 2019). DOI: 10.1007/s41781-018-0019-7. URL: https://doi.org/10.1007%2Fs41781-018-0019-7.

[96] J Butler et al. *CMS Phase II Upgrade Scope Document*. Tech. rep. Geneva: CERN, Sept. 2015. URL: https://cds.cern.ch/record/2055167.

[97] Rikiya Yamashita et al. "Convolutional neural networks: an overview and application in radiology". In: *Insights into Imaging* 9.4 (2018), pp. 611–629. DOI: 10.1007/s13244-018-0639-9. URL: https://doi.org/10.1007/s13244-018-0639-9.

[98] Yanming Guo et al. "Deep learning for visual understanding: A review". In: *Neurocomputing* 187 (2016). Recent Developments on Deep Big Vision, pp. 27–48. ISSN: 0925-2312. DOI: https://doi.org/10.1016/j.neucom.2015.09.116. URL: https://www.sciencedirect.com/science/article/pii/S0925231215017634.